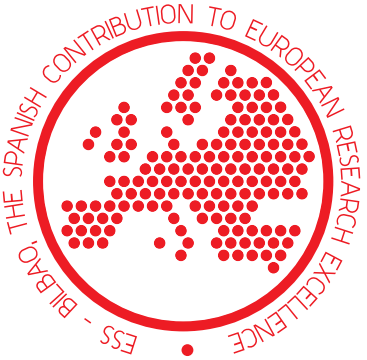

ESS bilbao

European Spallation Source: ESS Target Design process

July 29, 2015

Authors	Review	Aproved
A. Ghiglino (ESSB) L. Mena (ESSB) A. Aguilar (ESSB) T. Mora (ESSB) I. Herraz (ESSB) R. Vivanco (ESSB) M. Magan (ESSB) J. de Vicente (ESSB) F.J. Bermejo (CESIC) F. Sordo (ESSB)	F. Sordo (ESSB)	

Contents

Chapter 1

Spallation Material Study

1.1 Introduction

Spallation sources are devices designed to produce neutrons from spallation nuclear reactions. In order to produce this kind of reactions it is necessary to accelerate a proton using electromagnetic fields up to they get a huge amount of kinetic energy. In that moment, protons are led to impact on a nucleus of a heavy atom (generally mercury, lead or tungsten) producing what it is known as spallation reaction.

The place where the reaction is produced it is known as Spallation Target and it is considered the neutron source. This Targets are complex devices, from an engineering point of view, where a huge amount of heat is deposited on the spallation material. In some cases, it is note that the heat density can be higher than fuel bars in a nuclear power reactor which an equivalent engineering challenge. ESS target is one of these cases.

The European Spallation Source is an ambitious European project with a budget higher to 1800 M€. The aim is to build the most important and the highest spallation source in the world. It will use a proton beam with final power deposited on the target of 5 MW 5 MW (five times higher than SNS and JPARC) which will impact on a tungsten Target cooled by helium gas.

The Target will be designed with a set of tungsten blocks placed inside of a wheel of 2.5 meter of diameter. Protons have an impact on the wheel in a radial direction. Inside the wheel, helium flows at high velocity, cooling the tungsten blocks dissipating the heat produced by the nuclear reactions. The wheel rotates at a speed of 0.2-0.5 Hz, so the proton beam impacts on a different region of the wheel, distributing the heat over the whole perimeter and volume.

The aim of this report is to evaluate ESS baseline design during nominal conditions with the current beam parameters (2.0 GeV, 2.5 mA of average current and a “Raster profile”) and evaluate different alternatives to reduce the working conditions in the spallation material.

1.2 Thermal Source

One of the first parameter to analyze is the power density profile on the spallation material due to the proton beam. In order to evaluate this thermal source, some simulations have been performed using MCNPX code [5].

As it has been mentioned, one of the objectives of this report is to evaluate alternative geometries in the spallation materials. Thus, thermal load has been evaluated as a function of the position vector, so thermal load is decoupled from a particular geometry. One of the hypothesis considered is that the energy deposition per proton is lineal and thus power profile is proportional to the spatial profile of the proton beam. Power density expression can be written as follows:

$$P(X,Y,Z) = Q_x(X) \cdot Q_y(Y) \cdot Q_z(Z) \tag{1.1}$$

Figure 1.1 shows spatial distribution of the proton beam. Currently the beam profile considered is a Rastering System [8] which allows to get flatter profiles.

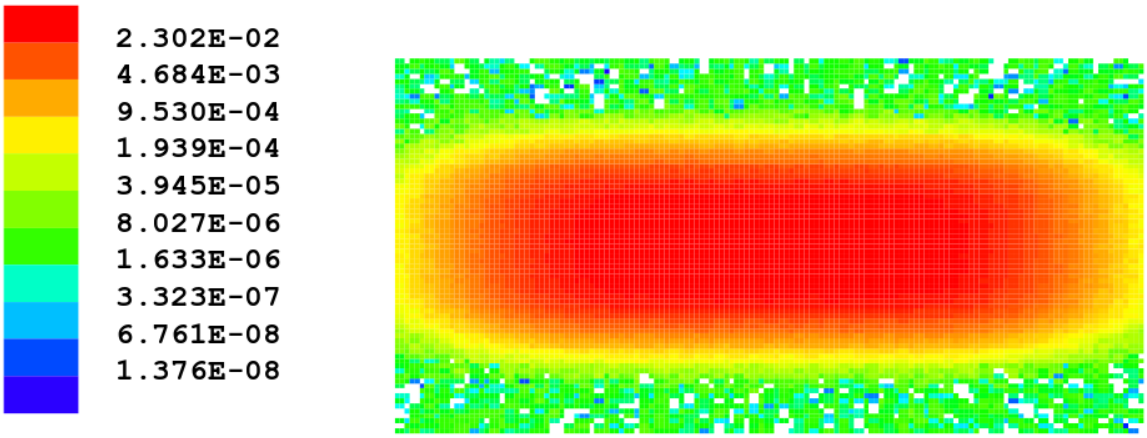

Figure 1.1: Spatial distribution of the raster proton beam.

To approximate the beam profile to an analytic expression we have considered several quadratic polynomials multiplied by symmetric exponential functions for both Q_x and Q_y. The integral of both functions must be one, so that global power will come from the function Q_z:

$$Q_x(X) = (a \cdot x^2 + b \cdot x + c) \cdot e^{-d \cdot x^2} \tag{1.2}$$

$$\int_{-8}^{8} Q_x(X) = 1 \tag{1.3}$$

$$Q_y(Y) = (a \cdot y^2 + b \cdot y + c) \cdot e^{-d \cdot y^2} \tag{1.4}$$

$$\int_{-3}^{3} Q_y(Y) = 1 \tag{1.5}$$

$$P_{total} = \int_{0}^{60} \int_{-3}^{3} \int_{-8}^{8} Q_y(y) \cdot Q_x(X) \cdot Q_z(Z) = \int_{0}^{60} Q_z(Z) \tag{1.6}$$

Figures 1.2 and 1.3 show the result of the interpolation. Proposed functions follow almost exactly the profile of the proton beam distribution. In both cases, the expressions have been normalized to guarantee that the integral is one on beam surface.

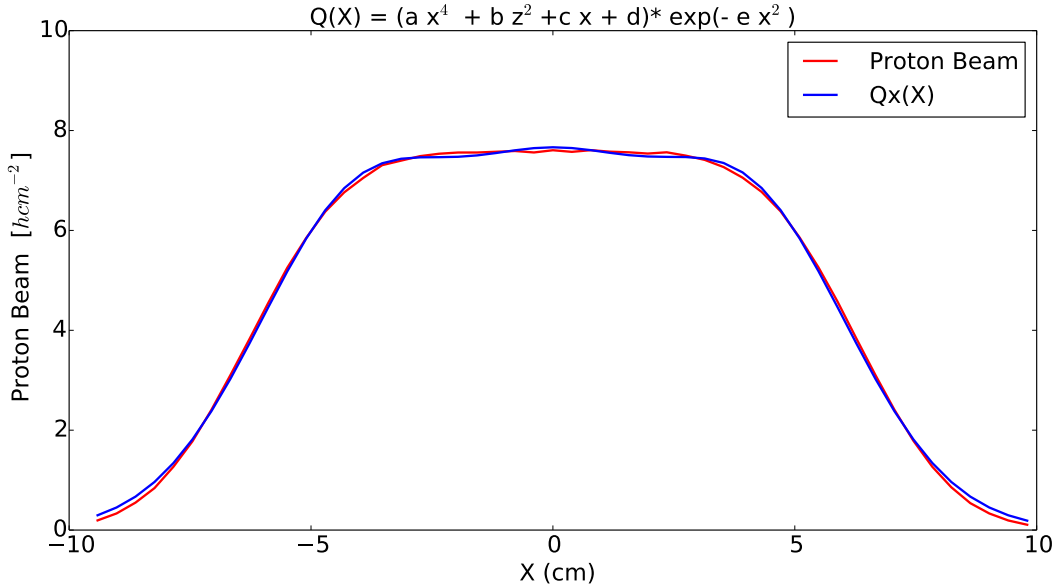

Figure 1.2: Approximation expression in X direction.

Figure 1.4 shows the lineal power deposition of the proton beam in the spallation material. This power distribution has been evaluated using a MCNPX mesh with one cell in X [-11:11] and Y [-4:4] directions and around 200 divisions in the beam direction. In this case, Z profile can not be approximated using a polynomial expression, so it has been used the following function:

$$Q_z(Z) = (a \cdot z^2 + b \cdot z + c) \cdot e^{d \cdot z} + e \cdot e^{-f \cdot z} \tag{1.7}$$

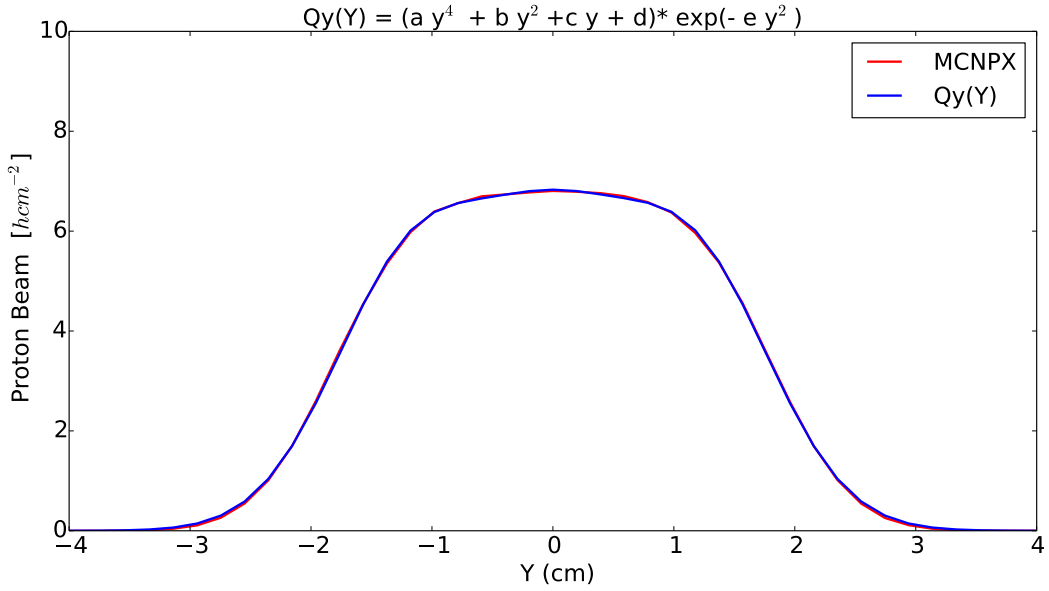

Figure 1.3: Approximation expression in Y direction.

It can be noticed in figure 1.4 that the expression is adjusted almost exactly to the MCNPX simulation.

Table 1.1 shows the values of the coefficients of the different interpolation functions. As a check execise, the integral along target volume considering CEM as intranuclear cascade model is around 2.56 MW with a peak value of 4.6 $kWcm^3$. The peak value from the direct MCNPX evaluation is 4.62 $kWcm^3$, so the interpolation works as expected. However, it is important to point out that this approximation has been done with the intention of analyze the spallation material volume which a high energy deposition, so this function is no applicable to other areas of the model.

	Q_X	Q_Y	Q_Z CEM	Q_Z Bertini
a	3.84E-2	3.30E+0	-1.68E-4	1.46E-4
b	5.04E-1	5.22E+0	2.90E+1	2.70E+1
c	1.98E-3	5.98E-3	1.97E+2	1.73E+2
d	7.66E+0	6.83E+0	1.47E+1	1.38E-1
e	7.99E-2	8.81E-1	-	-

Table 1.1: Coefficient values of the different expressions.

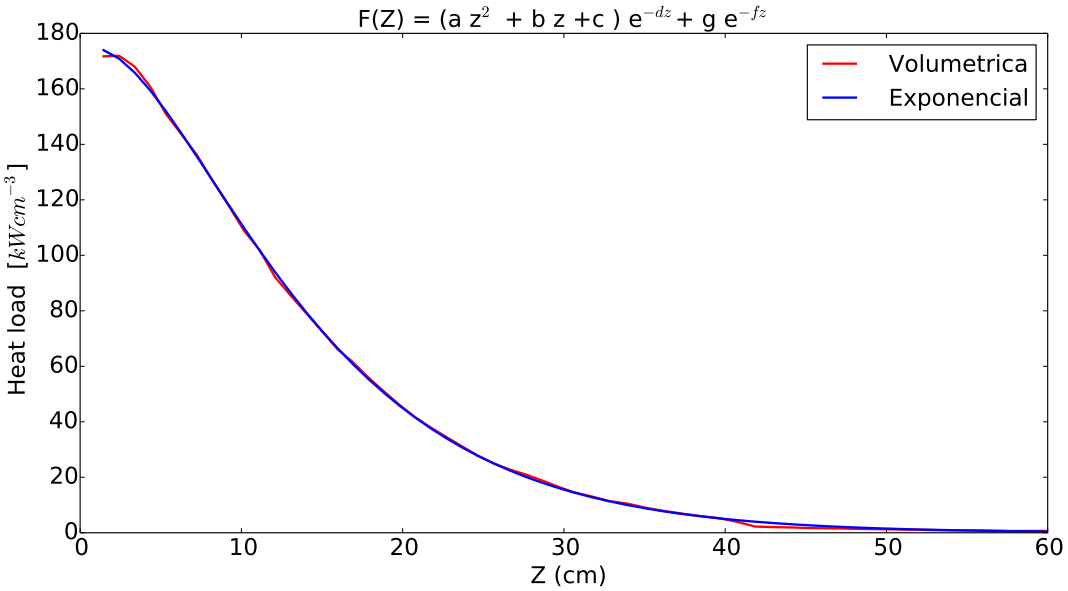

Figure 1.4: Approximation expression in Z direction.

1.3 ESS Baseline Design Analysis

1.3.1 Geometry Description

The rotatory target is divided by 33 sectors assembled in a wheel of 2.5 m of diameter which rotates synchronized with the pulse proton beam, so each sector receives 1 of 33 pulses. Based on this rotation effect the ∼2600 kW heat load is divided in between the sectors, that can be considered for the thermal analysis as an isolated element with a heat power of ∼ 75 kW.

The concept of each sector proposed by ESS shows similarities with other tungsten target designs cooled by water, like ISIS and Lujan Center (Los Alamos) [1] [2]. This configuration consists of some tungsten slabs parallel between them and with a thickness rising in the beam direction (1-10 cm). Helium flows through the cooling channels which are the space between the slabs (∼ 3 mm). This concept is shown in figure 1.5.

With the aim of homogenizing the distribution of temperature in the system, there are some additional elements between lateral zones, in such a way that helium path has a ”S“ shape.

Helium mass flow rate inside the target is 3 $kg \cdot s^{-1}$ (∼ 91 $g \cdot s^{-1}$ on each sector) with an inlet temperature of 40ºC and an average pressure of 10 bar.

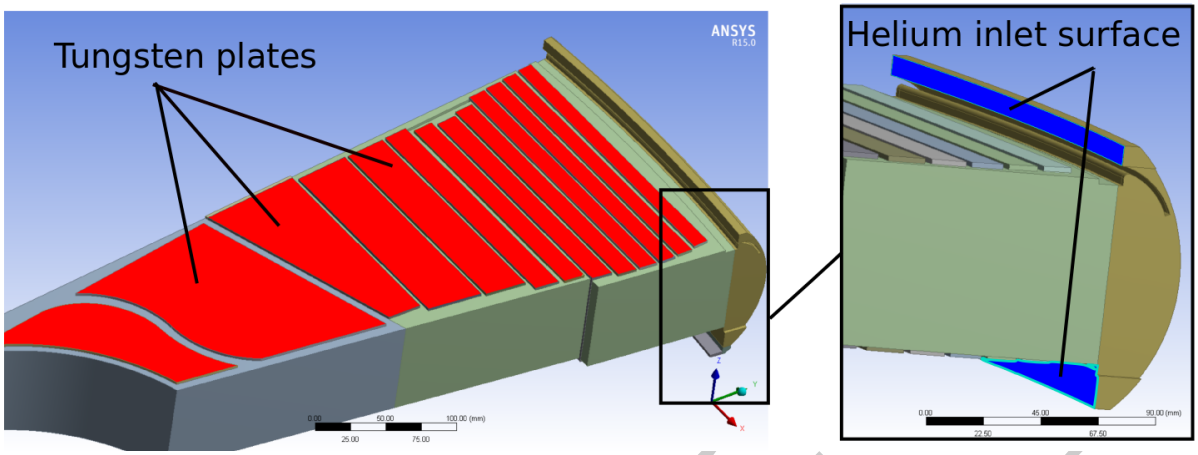

Figure 1.5: ESS baseline geometry.

1.3.2 Thermal Analysis

The thermal analysis has been performed using the CFD code FLUENT [11] with compressible fluid and viscosity $k-\omega$ models and temperature variable properties. Regarding helium, it has considered an ideal gas with some properties variable with temperature as viscosity, thermal conductivity and specific heat. Finally, for tungsten it has been used a thermal conductivity variable with temperature. Based on the discrepancies between available data considered on previous analysis two different approaches for the thermal conductivity has been consider: TDR-2013 and ESS-2014.

Figure 1.6 shows helium velocity profile. Maximum values are above 160 $m \cdot s^{-1}$ and are located in both lateral collectors (highlighted with black rectangles). According to the available information about some erosion experiments, currently under study, at Lund University [12], it is recommended to reduce maximum velocity values down to 100 $m \cdot s^{-1}$.

Regarding temperature distribution, it is shown in figure 1.7. By contrast to the targets cooled by materials with higher specific heat [4] in which the increase is moderated, helium is heated from 40^{o}C to 240^{o}C. This heating increases tungsten temperature while helium goes through the channels. On the other hand, growing thicknesses in tungsten slabs homogenizes heat dissipation on each slab. Both effects produce that heat distribution is decoupled from the proton beam profile. Maximum temperature value is reached in the 9^{th} slab, around 380^{o}C which is lower to the operational limit (it is recommended to work below 500^{o}C to avoid tungsten oxidation). It is noticed that this temperature distribution is not symetrical to the horizontal midplane because of the narrowing in top inlet channel and this produces an increase of the mass flow rate in the bottom part of the system.

Such as it has mentioned, there are some discrepancies for thermal conductivity in the avail-

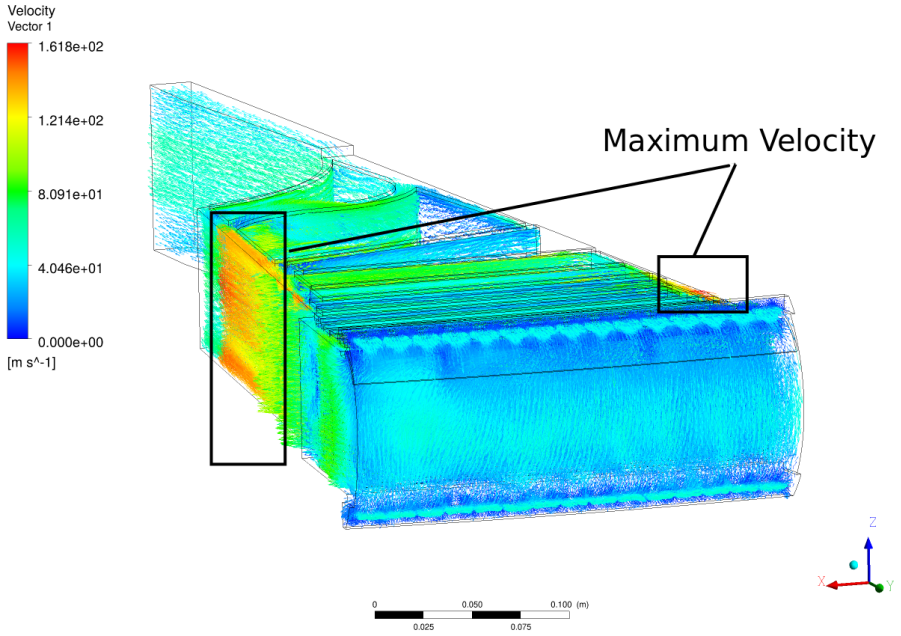

Figure 1.6: ESS baseline velocity profile.

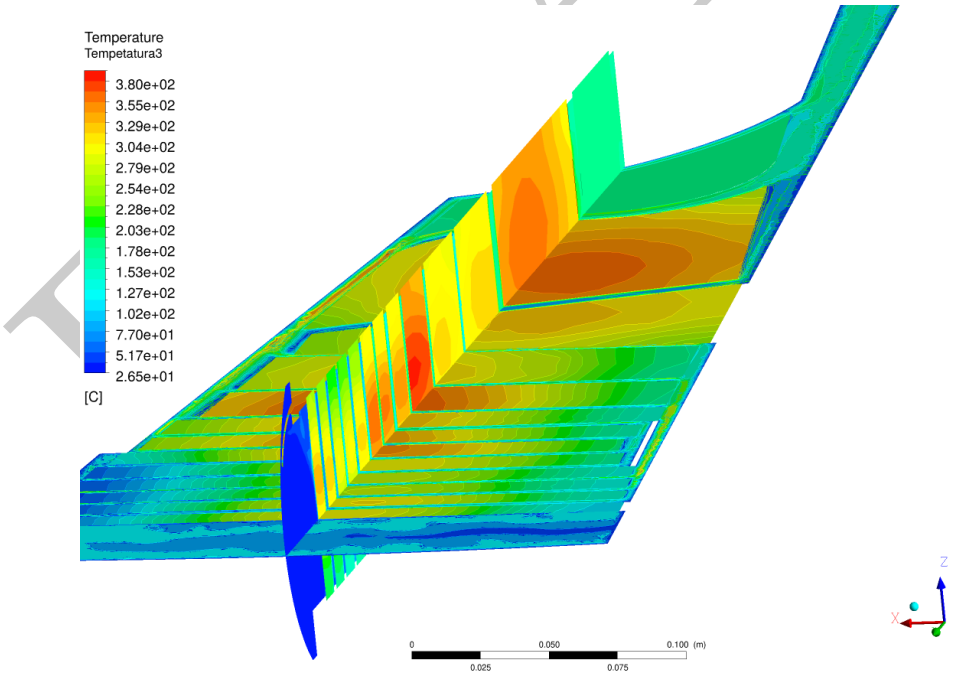

Figure 1.7: ESS baseline temperature profile.

able data. Figure 1.8 shows the evolution of the thermal conductivity used in the TDR [6] and in the documentation provided by ESS Target team[7]. It is noticed a difference in

the thermal conductivity close to 15% at the operation temperature 350^{o}C. To reduce the uncertainties related to this discrepancy, it has been compared maximum temperature and stress values for both cases. Using the properties from the TDR, maximum temperature increases up to 420^{o}C.

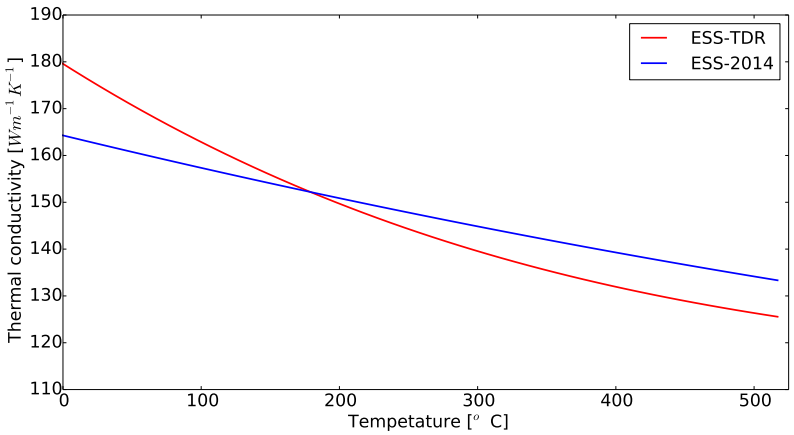

Figure 1.8: Tungsten thermal conductivity evolution with the temperature.

1.3.3 Mechanical Analysis

To complete the analysis of the baseline design, it has been evaluated mechanical stress profiles in the firsts tungsten slabs. Stress values are linked to the constrains of the slabs so as a first approach a free expansion conditions has been considered (no constrains).

It is important to notice that, like with the thermal conductivity, there are some discrepancies about thermal expansion coefficient of the tungsten in the ESS data sets. Figure 1.9 shows temperature evolution of the thermal expansion for two different sources of properties, the one used in the TDR and the one provided by ESS team in 2014. It can be seen that at operational conditions (350^{o}C) thermal expansion is lower for ESS-2014 properties.

Figure 1.10 shows Von Mises Stress profiles using Bertini intranuclear cascade model and ESS mechanical properties. On the other hand, for CEM intranuclear cascade model, maximum stress value reaches around 170 MPa.

Considering design requirements in the tungsten provided by ESS [9], maximum stress value must be below 100 MPa, thus this proposal does not achieve these requirements even though the fix system has not been taken into account.

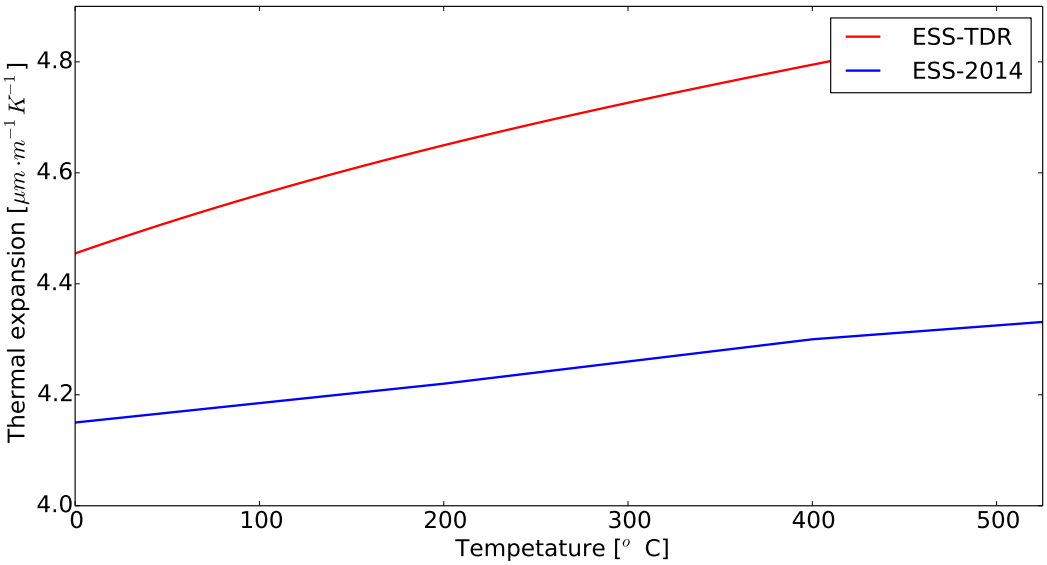

Figure 1.9: Tungsten thermal expansion evolution with the temperature.

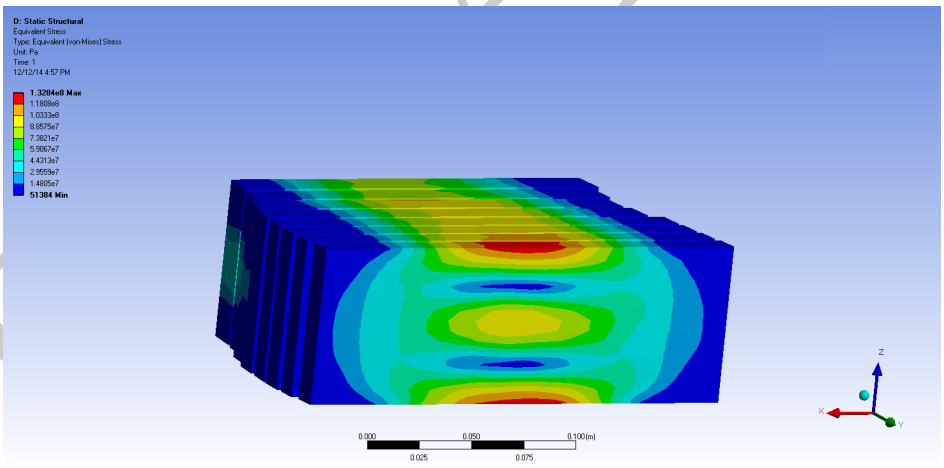

Figure 1.10: Stress profile in the first tungsten slabs.

1.4 ESS-Bilbao alternative proposal

1.4.1 Introduction

As it has been noticed from the thermo-mechanical analysis of the baseline configuration, tungsten slabs are under a mechanical stress of around 130-180 MPa, depending on the material properties and on the intranuclear cascade models considered, exceeding up to an 80% of the requirements established by ESS, that for the steady state case is around 100 MPa.

Thus, in order to reduce maximum stress values it has been proposed to use rectangular blocks with dimensions of tens millimeter instead of the slabs. This decrease on the dimensions will minimize the thermal gradient and expansion and thus mechanical stress is reduced.

The bricks will be placed in a quincunx configuration to avoid that protons go through the target without interact with the spallation material damaging structural material. Besides, with this configuration the helium is forced to go around the bricks sides increasing the cooling.

The first step performed has been a 2D parametric analysis to optimize blocks dimensions and the helium gap between them. It has been used the thermal load and material properties used in the TDR [6]. The helium has been simulated as a compressible fluid using an ideal gas for density and temperature variable for thermal conductivity and viscosity [10]. As is in the base line analysis the analysis has been performed with FLUENT considering SST $k-\omega$ viscosity model.

Table 1.2 shows the summary of the analysis. The variables represented are:

- L_x Length of the block in X direction (X axis is perpendicular to the beam).
- L_y Length in Y direction (Y axis is parallel to the beam).
- Gap_x Gap in X direction.
- Gap_y Gap in Y direction.
- ρ Spallation material density represented as a volume percentage that the tungsten blocks occupied in the volume of the whole sector.
- T_{max} Maximum temperature reached in the target.
- Vel_{max} Maximum helium velocity.
- ΔP Pressure drop.

The optimum configuration is represented in red. It is for rectangular blocks of 10 mm length in X direction and 30 mm length in Y direction with a helium gap between blocks of 2 mm in both directions and a density of 80%. Maximum temperature and velocity are 353^{o}C and 100 m/s respectively with a pressure drop of 0.25 bar. Comparing these values to the baseline configuration, it can be observed that in this 2D analysis velocity and pressure drop are highly reduced: velocity is reduced from 170 m/s to 100 m/s and pressure drop from 0.4 bar to 0.25 bar.

L_x (mm)	L_y (mm)	Gap_x (mm)	Gap_y (mm)	ρ (%)	T_{max} (^{o}C)	Vel_{max} (m/s)	ΔP (bar)
15	15	1	1	88	390	200	2.5
15	15	2	2	78	343	132	0.72
10	30	1	1	88	390	137	0.9
10	**30**	**2**	**2**	**78**	**353**	**100**	**0.25**
30	10	1	1	88	325	346	8.2

Table 1.2: 2D analysis summary.

Figure 1.11 shows some examples of the geometry studied. On the top right side it is represented the optimal solution.

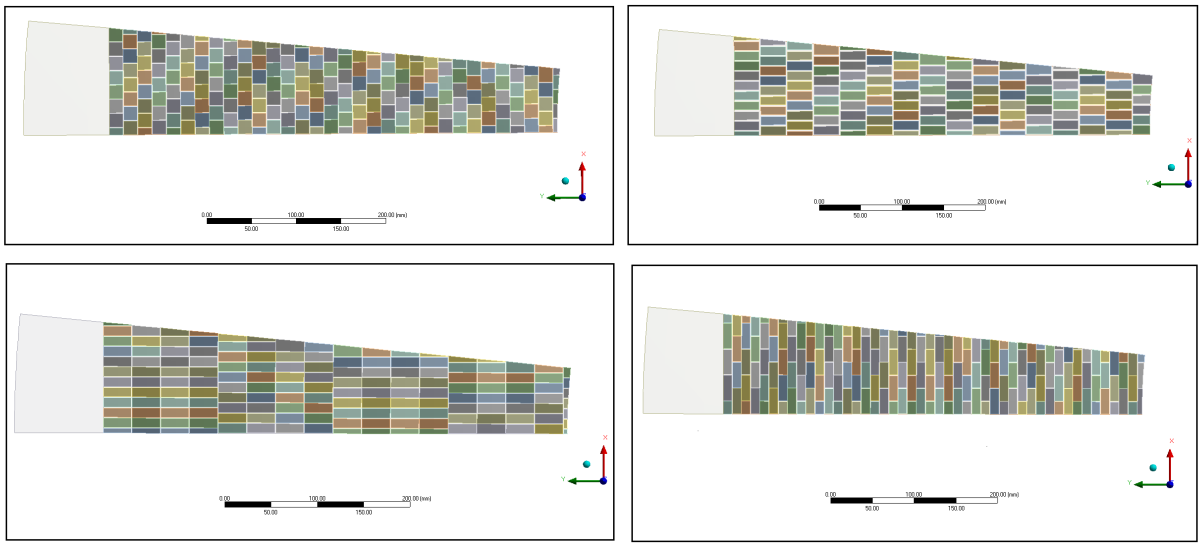

Figure 1.11: 2D examples.

1.4.2 3D Thermo-Mechanical Analysis

Once it has been obtained the most optimal configuration of the blocks, the next step is to analyze 3D effects produced by the thermal load described on previous sections(Section 1.2). As it has been seen before, there are some discrepancies for both different intranuclear cascade models, being more conservative CEM model (Cascade-Exciton Model) and Bertini the most optimistic. In this section it will be seen a comparison between both models and after that an analysis comparing the difference between the material properties.

Figure 1.12 shows the 3D geometry corresponding to a sector with a symmetry boundary condition in the middle plane YZ. Helium goes into the target in both top and bottom inlets, cooled the Beam Entrance Window and leave the sector from the center. The mass flow rate on each sector is around 0.091 kg/s (3 kg/s divided in 33 sectors). Helium inlet conditions

are 40ºC and an average pressure of 10 bar.

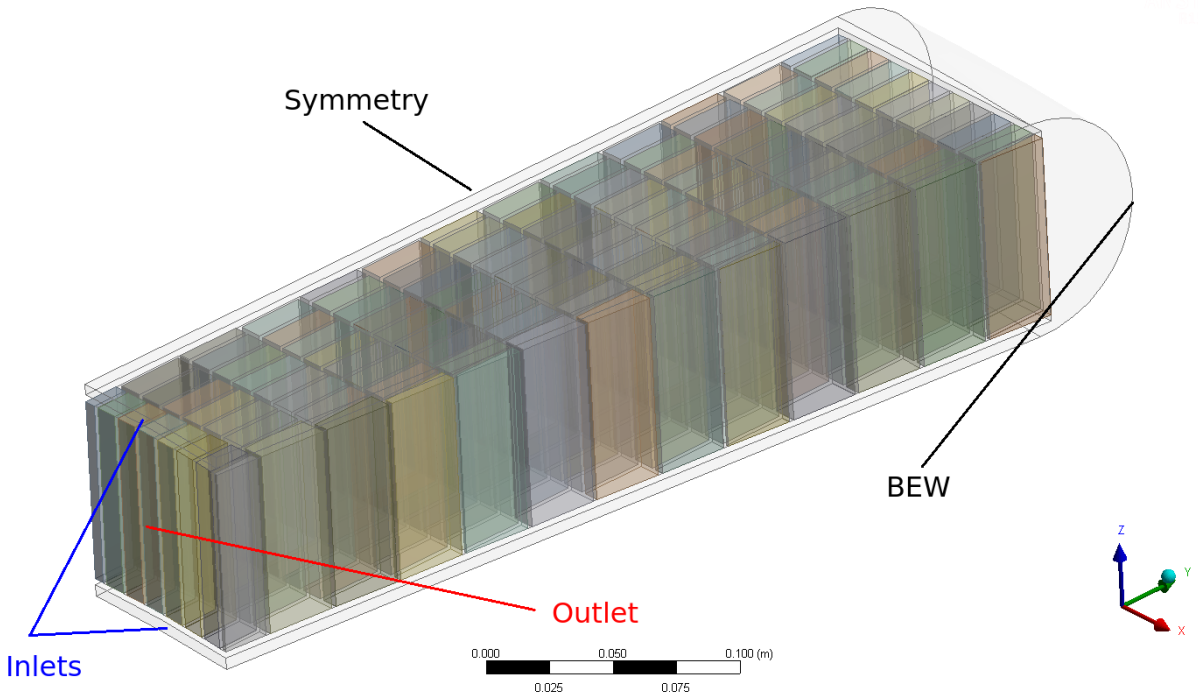

Figure 1.12: 3D geometry.

In the velocity profile can be observed that while the pressure is reducing, the velocity increases up to reach 70 m/s with a total pressure drop of 0.2 bar (see figure 1.13).

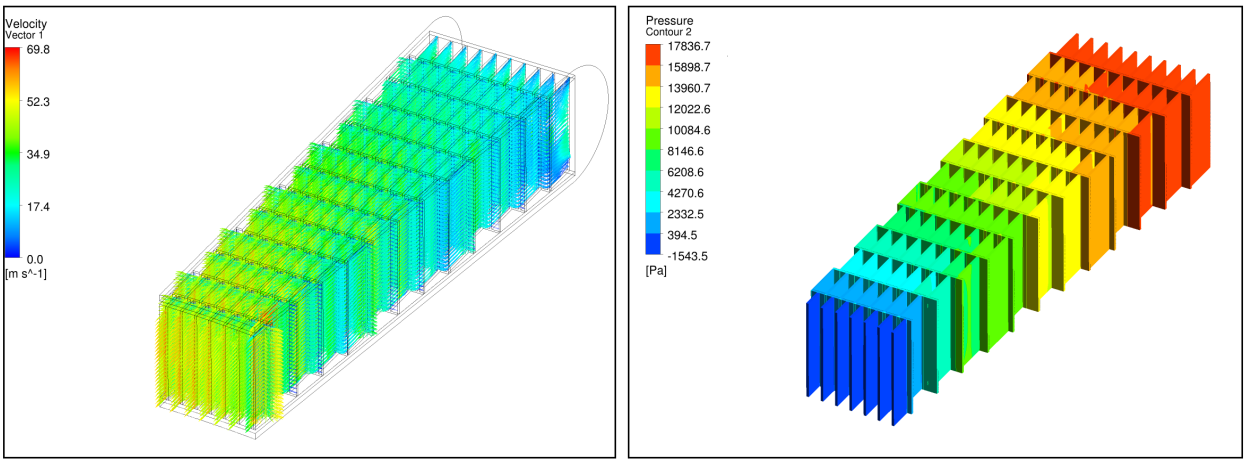

Figure 1.13: Velocity profile and pressure drop.

Such as it has seen in the baseline analysis, temperature distribution changes depending on the intranuclear cascade considered. This will affect to the maximum stress value reached in the blocks. To assess this effect, it has been performed a comparison between the thermo-mechanical results taking into account both models.

Figures 1.14 and 1.15 show temperature and stress profiles considering Bertini model and using TDR material properties. Maximum temperature is around 358^{o}C and it is reached in the second row of blocks just in the center, where the power density is maximum. In spite of that power density reached its maximum value in the firsts centimeter of spallation material and decreases exponentially, maximum temperature is steady in all the blocks placed in the center of the sector. This effect is produced, not due to the heat deposition of the protons heating the tungsten, but due to the heating of the helium which produces a heating of the tungsten blocks. Maximum von Mises stress is around 81 MPa in the block of the second row in the center of the sector, where thermal gradient is higher.

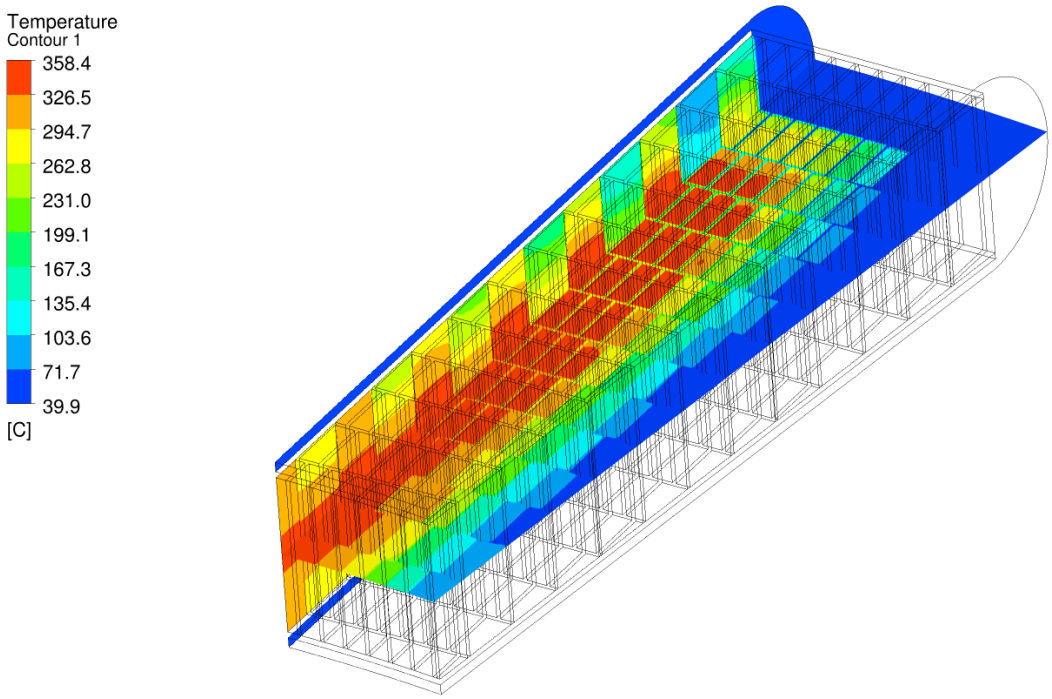

Figure 1.14: Temperature profile for Bertini model.

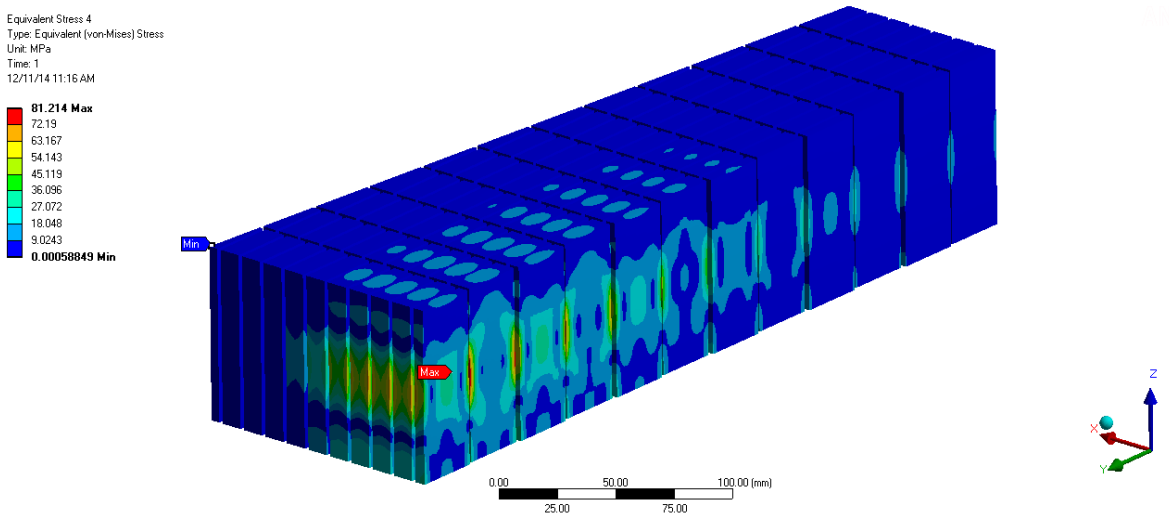

Figure 1.15: Stress profile for Bertini model.

For CEM model case, figures 1.16 and 1.17 represents temperature and stress maps. It is observed that maximum temperature is higher than for Bertini model, reaching around 374^{o}C. Maximum stress is close to 90 MPa. Thus, as it has mentioned before, CEM model provides more conservative values. However, for both models tungsten requirements are fulfilled.

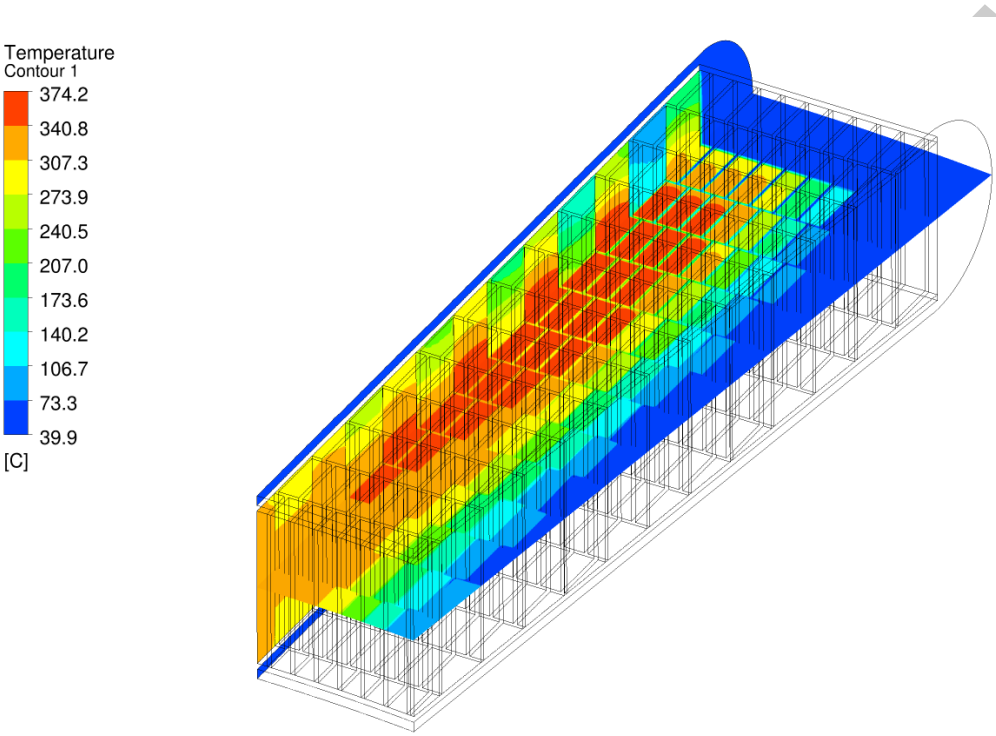

Figure 1.16: Temperature profile for CEM model.

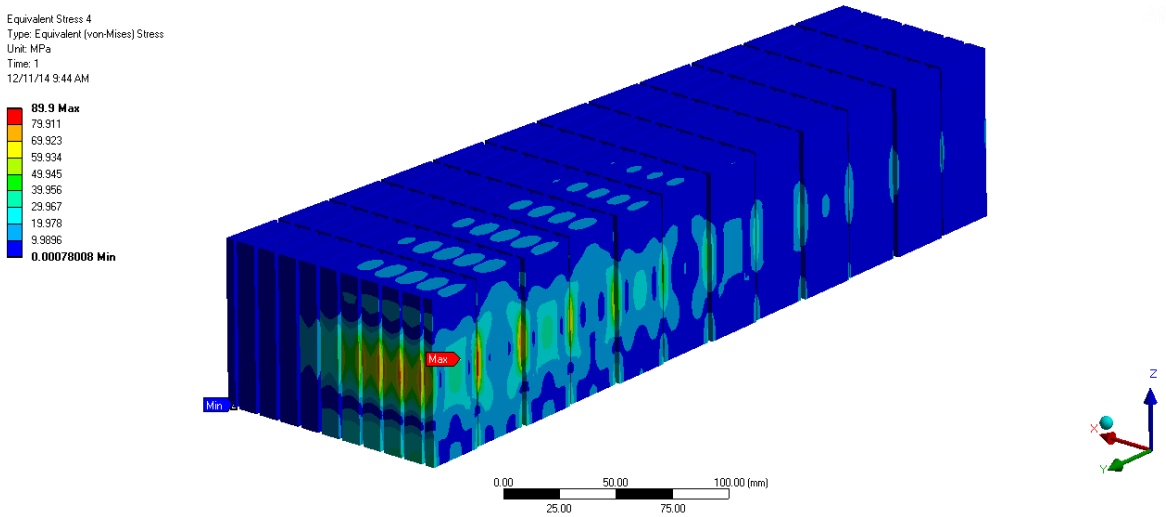

Figure 1.17: Stress profile for CEM model.

Optimization

Once it has been seen the 3D effect produced by the thermal source in the tungsten blocks, next step consists of optimizing thermal-hydraulic design. Looking carefully at figure 1.13 it can be concluded that a not negligible part of the helium flows through the extremes of the sectors, where the tungsten is colder. Thus, to optimize the cooling behavior we proposed to increase the mass flow rate in the center of the sector reducing the gap in X direction (Gap_x) between blocks in the extreme of the sector, keeping constant Gap_y. This is shown in figure 1.18. Mass flow rate in the center of the sector is increased without a significant change in the velocity profile but increasing pressure drop, which rises up to 0.25 bar (see 1.19).

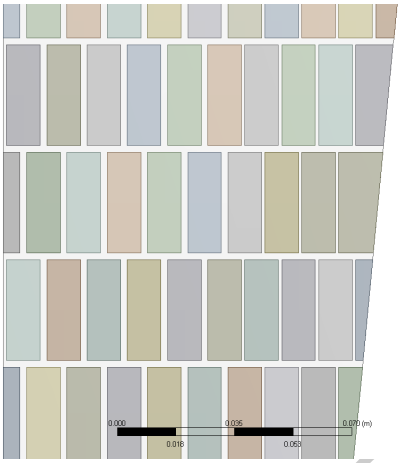

Figure 1.18: Geometry optimized.

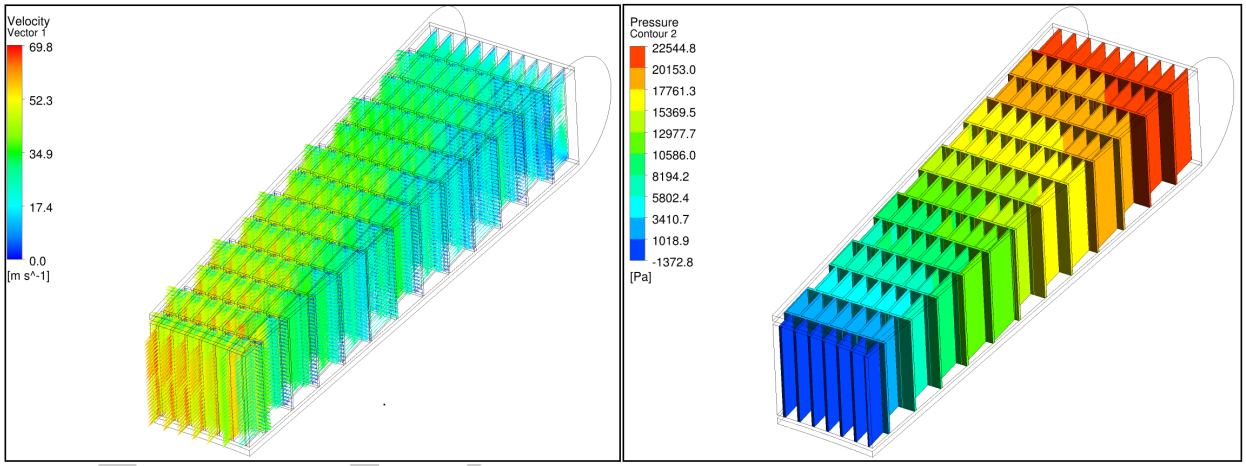

Figure 1.19: Velocity profile and pressure drop after the optimization.

According to the temperature, it is seen that the effect of increasing the mass flow rate in the center of the sector reduces maximum temperature. For Bertini model, maximum temperature is around 325^{o}C which is around 35^{o}C lower than the case without optimization. Thermal stress is reduced reaching a value of 78 MPa, but not significantly because of thermal gradient which is almost the same.

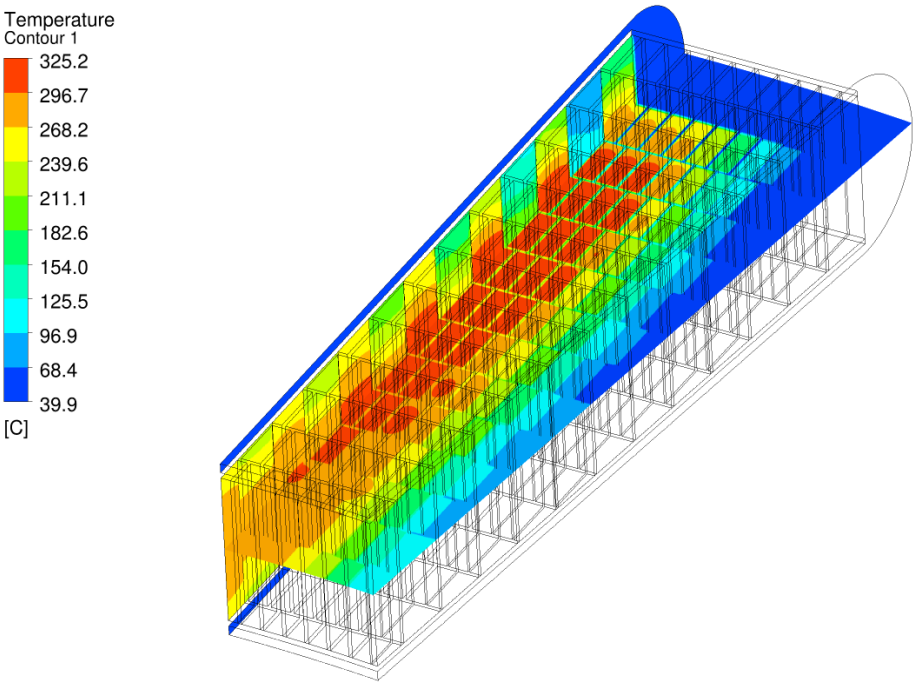

Figure 1.20: Temperature profile for Bertini model and optimized geometry.

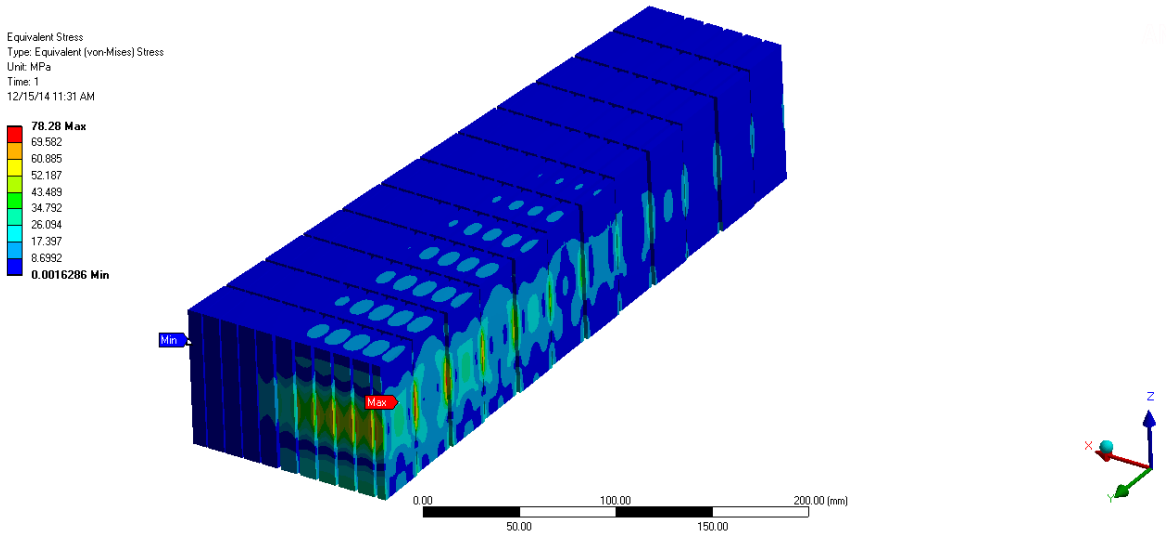

Figure 1.21: Stress profile for Bertini model and optimized geometry.

For CEM model, maximum temperature reached is around 341^{o}C, again around 35^{o}C lower than the case without optimization and a maximum stress of 86.5 MPa, very close to the 90 MPa reached without any optimization. In summary, this optimization reduces maximum temperature by 35^{o}C, but for stress behavior there is no a significant reduction because thermal gradient has a negligible variation.

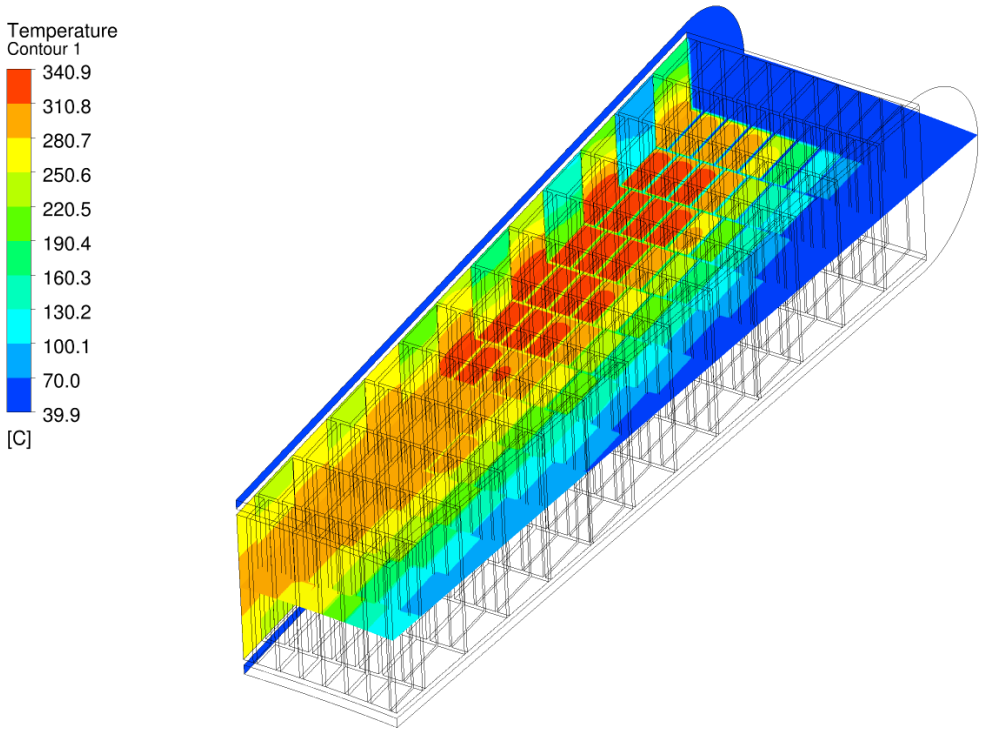

Figure 1.22: Temperature profile for Bertini model and optimized geometry.

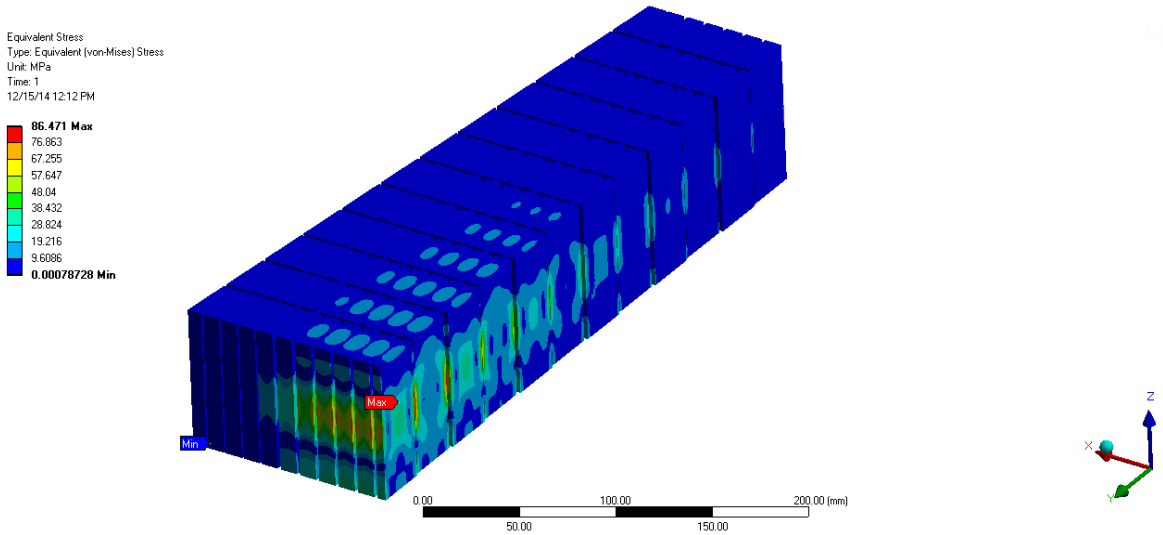

Figure 1.23: Stress profile for Bertini model and optimized geometry.

Comparison between different material properties

In this study it will be assessed the results using a set of material properties provided by ESS (named ESS-2014) and considering both intranuclear cascade models. For Bertini case, maximum temperature is reduced down to 314^{o}C, around 10^{o}C lower than the case obtained with TDR properties due to thermal conductivity is slightly higher in ESS-2014 properties. However, the main effect is produced in thermal stress which is reduced down to 58 MPa, 20 MPa lower because of the difference in thermal expansion, considerably lower for ESS-2014 properties. For CEM case, maximum temperature is reduced down to 332^{o}C and a maximum stress of 63 MPa.

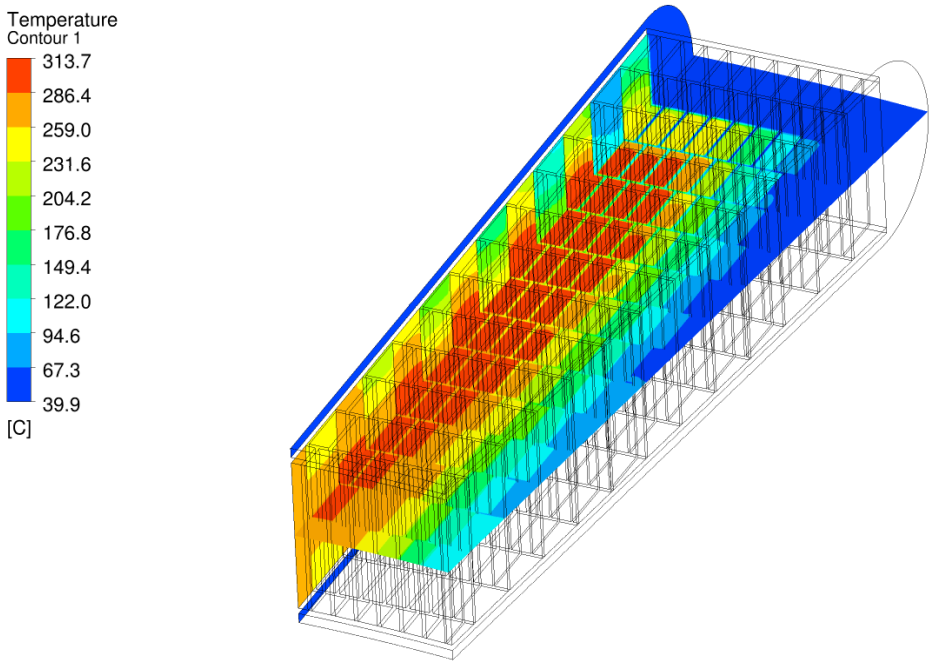

Figure 1.24: Temperature profile for Bertini model and optimized geometry.

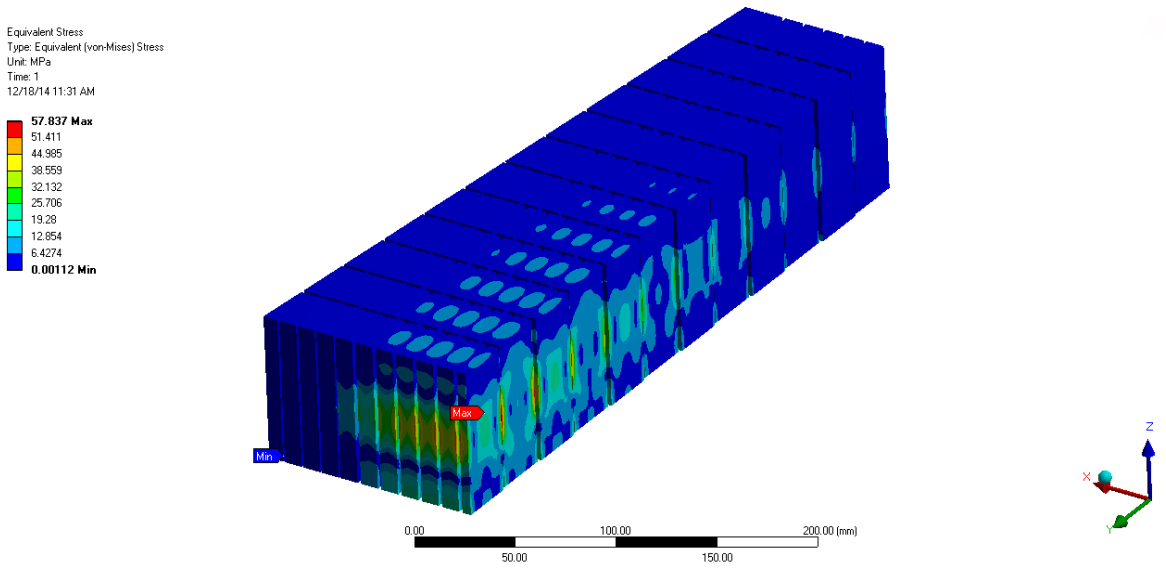

Figure 1.25: Stress profile for Bertini model and optimized geometry.

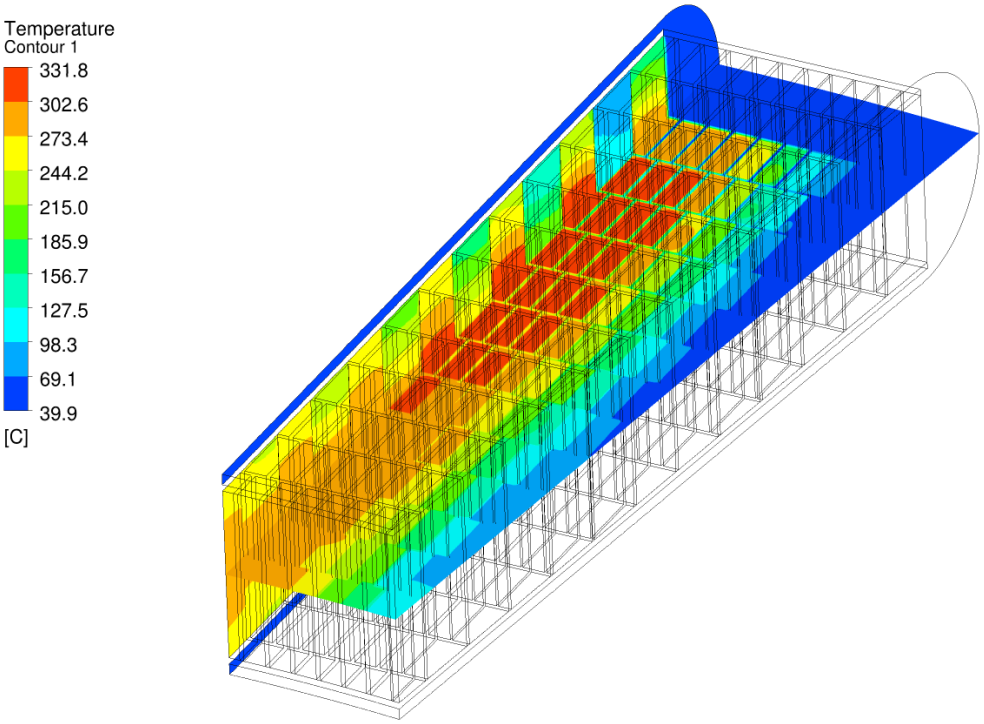

Figure 1.26: Temperature profile for Bertini model and optimized geometry.

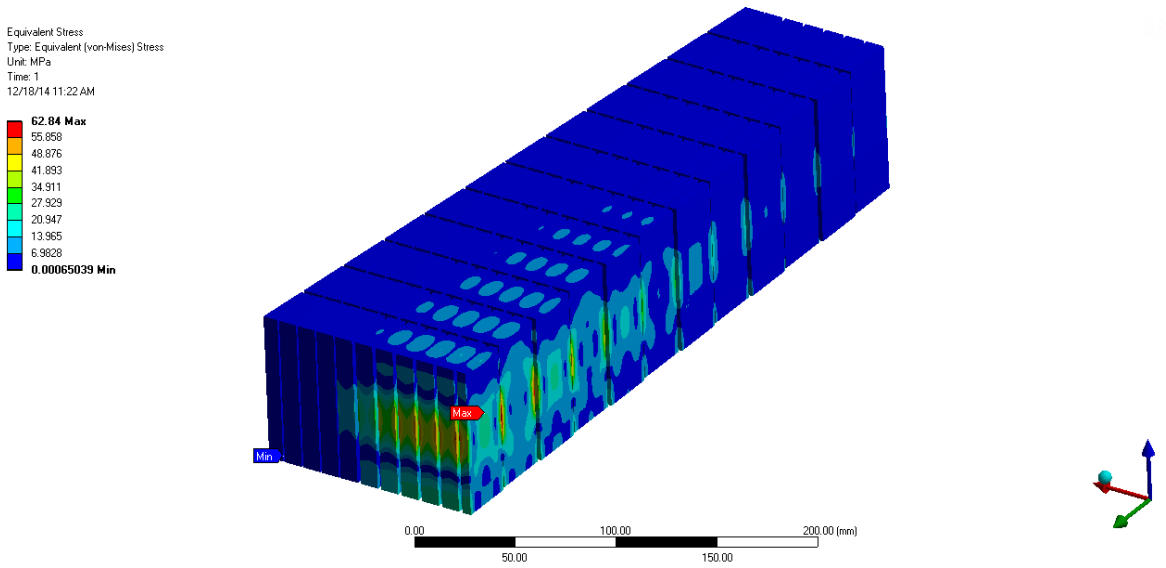

Figure 1.27: Stress profile for Bertini model and optimized geometry.

Regardless of the intranuclear cascade model and material properties considered, in all cases stress and temperature values are below ESS requirements for tungsten, established in [9] where temperature limit is 500^{o}C and steady state stress is 100 MPa. Table 1.3 shows a summary of the values obtained in this 3D steady state analysis combined the results considering different material properties and different intranuclear cascade for the optimized geometry. The range of maximum values where the tungsten fluctuates is: for temperature, **314**^{o}C and **341**^{o}C and for stress, **86.5** MPa and **58** MPa for Bertini with ESS-2014 properties and CEM with TDR properties respectively. This means that temperature varies ± 30^{o}C and stress ± 30 MPa, approximately.

	$T_{max,\mathbf{CEM}}$ (^{o}C)	$\sigma_{max,\mathbf{CEM}}$ (MPa)	$T_{max,\mathbf{Bertini}}$ (^{o}C)	$\sigma_{max,\mathbf{Bertini}}$ (MPa)
ESS-TDR Properties	**341**	**86.5**	325	78
ESS-2014 Properties	332	63	**314**	**58**

Table 1.3: Summary of the analysis performed with the optimized geometry

1.4.3 3D Transient Analysis

As it is known, ESS neutron target consists of a wheel divided by 33 sectors where a pulsed proton beam transfers its energy with a frequency of 14 Hz and a pulse length of 2.86 ms. Each pulse impacts on a different sector, so that each one has enough time to cool down. Thus, next step consists of considering transient effect in the target for both thermal and mechanical behavior.

Figure 1.28 shows time evolution of the maximum temperature in the tungsten for the most optimistic model (Bertini model and ESS-2014 material properties) and the most conservative one (CEM model and TDR properties). For Bertini and ESS-2014 properties, maximum temperature reached is around **365^{o}C** whereas for CEM and TDR properties is **395^{o}C**. It is important to highlight that these curves are the time evolution of the maximum temperature in the system and the position of this moves downstream after the proton pulse as it shown on Figure 1.29.

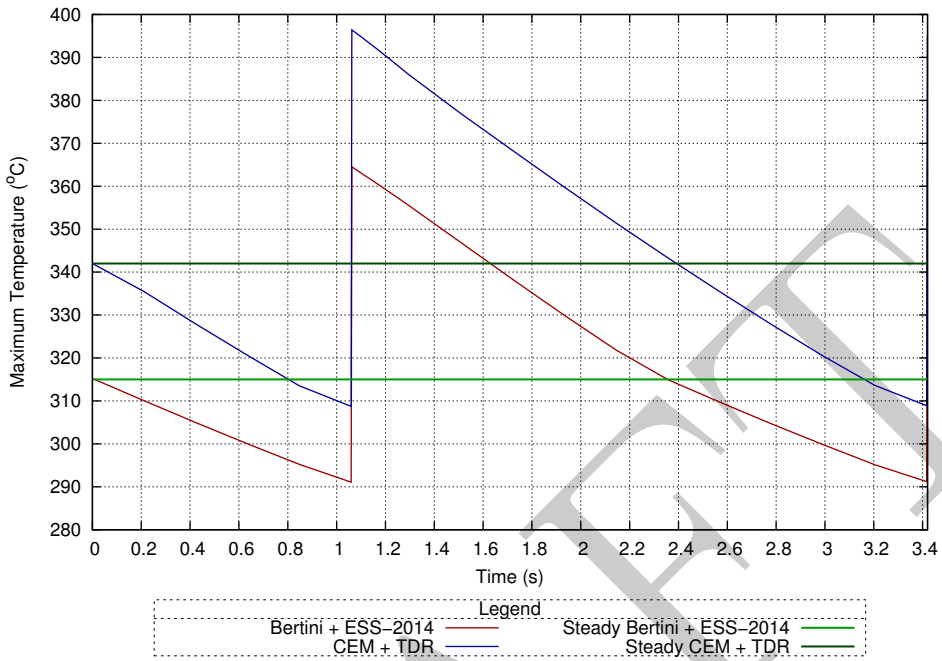

Figure 1.28: Time evolution of the maximum temperature in the system for Bertini with ESS-2014 properties and CEM with TDR properties.

Figures 1.29 and 1.30 show temperature and stress profiles before a new pulse (when the sector is cooled down) and just after a pulse (when temperature is maximum) for the most optimistic model respectively. Temperature and stress increases in the worst block (second row at the center of the sector) are $\Delta T \sim 105 - 110^o$C and $\Delta\sigma = 40$ MPa.

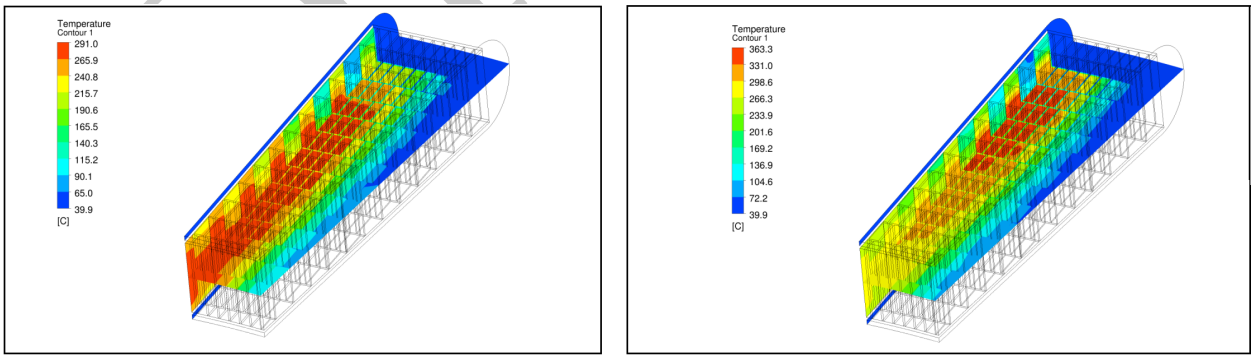

Temperature Before a Pulse

Temperature After a Pulse

Figure 1.29: Temperature peak for Bertini with ESS-2014 properties.

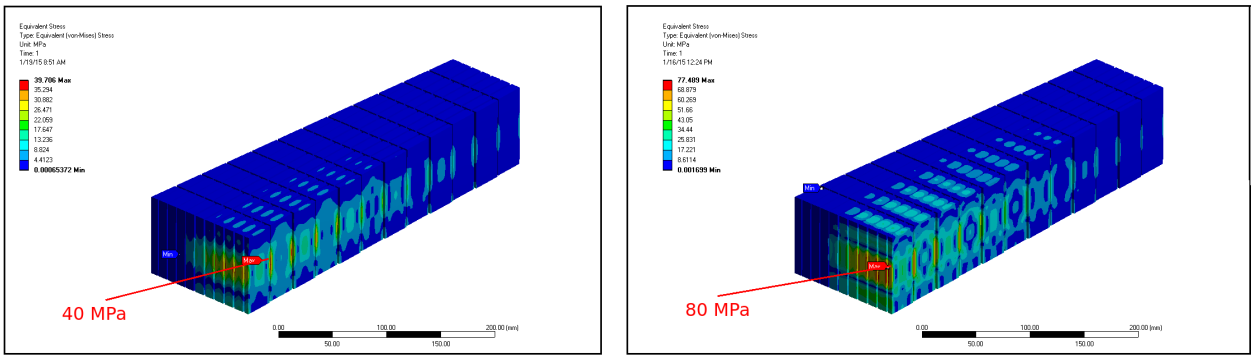

Stres Before a Pulse

Stress After a Pulse

Figure 1.30: Stress peak for Bertini with ESS-2014 properties.

For the most conservative conditions temperature and stress peaks in the worst block are $\Delta T \sim 110 - 120^o$C and $\Delta\sigma = 50$ MPa, as expected slightly higher. It can be remarked, the displacement downstream of the hot spot is due to the helium flow, which transfers energy from the first lines of brick to the last ones.

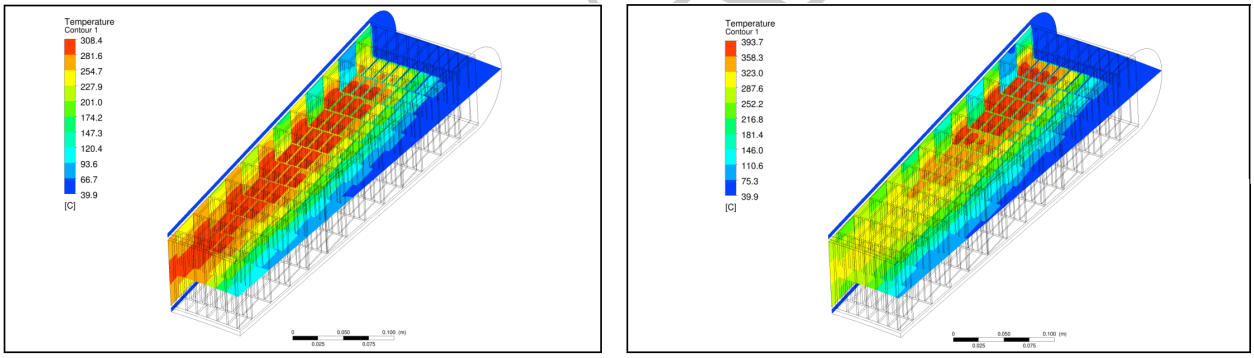

Temperature Before a Pulse

Temperature After a Pulse

Figure 1.31: Temperature peak for CEM with TDR properties.

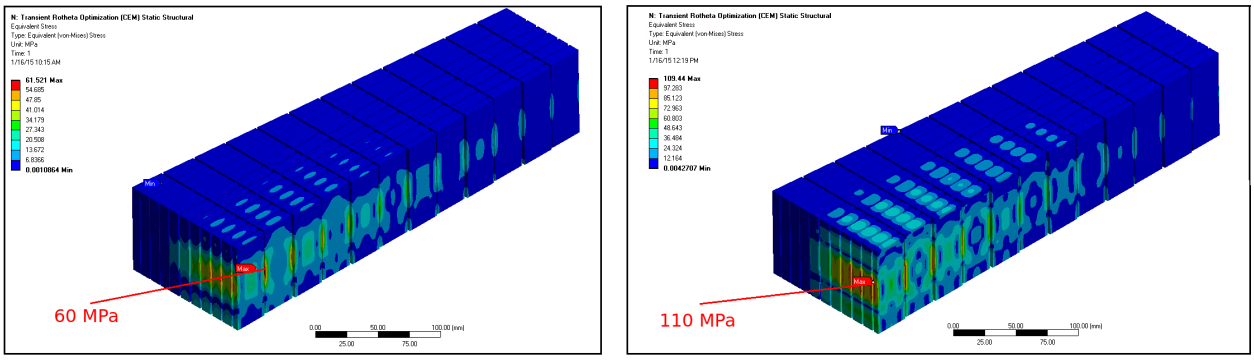

Stres Before a Pulse

Stress After a Pulse

Figure 1.32: Stress peak for CEM with TDR properties.

1.4.4 Evaluation of loss of thermal conductivity in the Tungsten

Due to some uncertainties in the behavior of the tungsten after high irradiation conditions, in this section a thermo-mechanical analysis has been performed considering a lose of 20% of thermal conductividad in tungsten. Table 1.4 shows the summary of the analysis. It can be seen that temperature is increased 15^{o}C for the most optimistic and the most conservative models, reaching **355^{o}C** for CEM model and TDR properties and **330^{o}C** for Bertini model and ESS-2014 properties. In the stress case, for Bertini model maximum stress value is around **70 MPa** still below of the ESS requirements. However, for CEM model and TDR properties maximum stress is **105 MPa** which is in the limit of the tungsten requirements. So it is important to notice that considering the most conservative scenario, target conditions are in the limit of the requirements. This means that for other models like i.e. Bertini with TDR properties, tungsten conditions will be below ESS requirements.

	$T_{max,\mathbf{CEM}}$ (^{o}C)	$\sigma_{max,\mathbf{CEM}}$ (MPa)	$T_{max,\mathbf{Bertini}}$ (^{o}C)	$\sigma_{max,\mathbf{Bertini}}$ (MPa)
ESS-TDR Properties	**355**	**105**	-	-
ESS-2014 Properties	-	-	**330**	**70**

Table 1.4: Summary of the analysis performed considering a lose of 20% of thermal conductivity in tungsten.

1.4.5 Thermal evaluation for different number of sectors

From a manufacturing point of view, if 33 sectors are considered it is a challenge task to manufacture pieces with periodic angles. So, the purpose of this section is to assess thermal-hydraulic behavior of the tungsten with different number of sectors. This study will be complemented with the mechanical analysis of the target vessel, performed in the next chapters. The decision of using an odd number of sectors is because in previous designs there were lateral helium channels surrounding spallation material, this means that in case of

beam desynchronization protons could pass through the target without interact with spallation material unless there was a sector on the other side to stop them. Nevertheless, current design does not have lateral helium channels and an odd number of sectors are not needed.

Figure 1.33 shows temperature profiles with different number of sectors: 28, 32, 33 and 36. As it was expected, the greater the number of sectors, the lower the maximum temperature. For 36 sectors a maximum temperature of 297^o is reached in the tungsten, increasing the safety margin of the device.

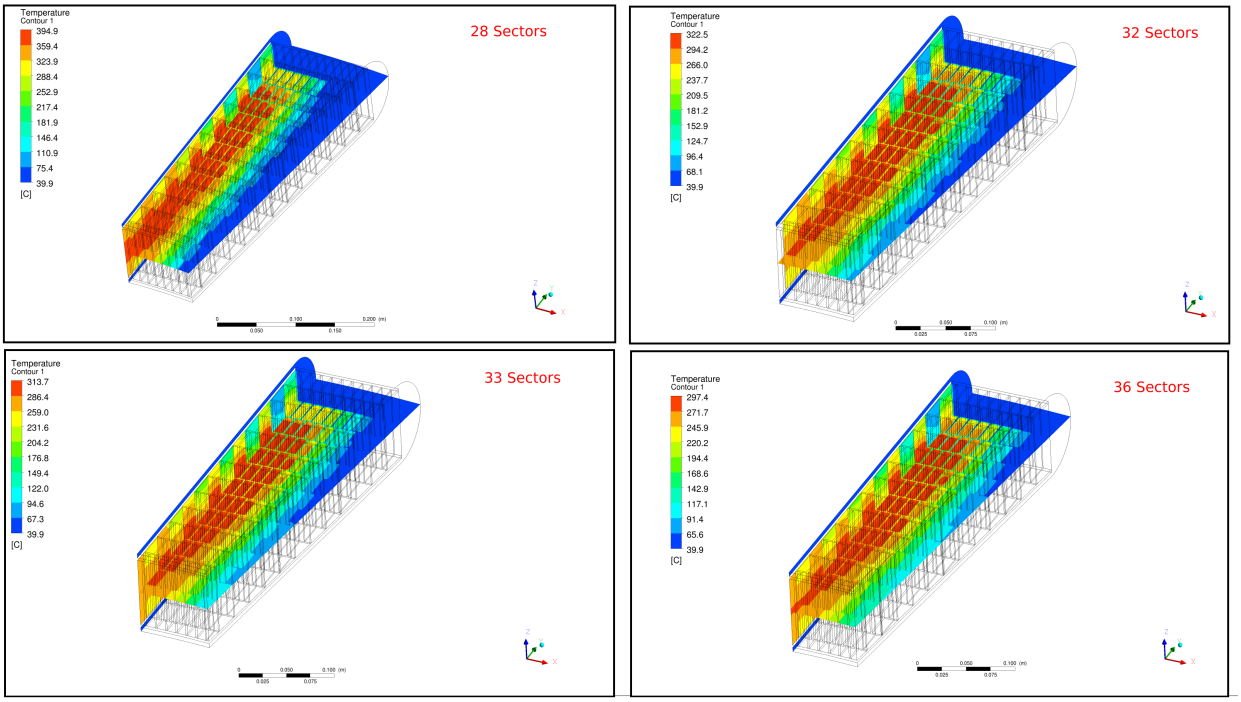

Figure 1.33: Temperature profiles with different number of sectors.

1.5 Conclusions

Table 1.5 shows a comparison between baseline configuration with the ESS-Bilbao proposal. With the blocks placed in a quincunx configuration, temperature can be reduced more than 70^{o}C and the stress almost the half. Even considering the most conservative design conditions (CEM intranuclear cascade model and TDR properties), ESS-Bilbao proposal fulfills with some margin ESS tungsten requirements.

	T_{max} (^{o}C)	σ_{max} (MPa)
ESS Baseline with TDR properties& CEM	**422**	**170**
ESS Baseline with ESS-2014 Properties & Bertini	**380**	**130**
ESS-Bilbao proposal with TDR properties & CEM	**341**	**86.5**
ESS-Bilbao proposal with ESS-2014 Properties & Bertini	**314**	**58**

Table 1.5: Comparison between baseline design and ESS-Bilbao proposal.

Focusing on the ESS-Bilbao proposal:

- From the steady-state case, it can be observed that maximum temperature will be in the range of **315-340^{o}C** and maximum stress between **60-90 MPa** (for Bertini model + ESS-2014 properties and CEM model + TDR properties respectively).
- For transient case, it can be seen that $\mathbf{\Delta T = 105 - 120^oC}$ and $\mathbf{\Delta\sigma = 40 - 50\ MPa}$, for Bertini model + ESS-2014 properties and CEM model + TDR properties respectively.
- After an irradiation period, thermal conductivity can be reduced up to 20%. In that case, maximum temperature will be between **330-355^{o}C** and maximum stress around **70-105 MPa** (for Bertini model + ESS-2014 properties and CEM model + TDR properties respectively).
- Considering 36 sectors, maximum temperature can be reduced up to **300^{o}C**, increasing the safety margin.

Chapter 2

Target Vessel

2.1 Shroud component

The initial baseline target design called for 33 target sectors, each made up of slabs of tungsten held in place between two structural holder beams. The 33 beams delimit the target sectors and are connected to a massive central hub that makes the transition to the shaft. The 33 sectors of spallation material and structural beams are contained between top and bottom ring-shaped lids welded to the periphery of the central hub, with a rim composed of the beam entrance windows (BEW) and their frames. The target wheel rotates around a vertical axis. The shrouds and rim form the gas-tight target vessel, which, together with the structural beams to which it is welded, forms the target's pressure container. In this section, it has developed a thickness optimization of the target vessel, specifically with the shroud component, and it has performed a stress sensitivity analysis considering different number of sectors (32, 33 and 36 target sectors) and seeing which one is more suitable from a mechanical point of view.

In order to determine the optimal thickness for structural beams and target vessel, a Shell model in FEM was used to perform the optimizations (Figure 2.1). In this section, a sensitivity analysis has been developed for different target sectors (see sections 2.1.4, 2.1.5, 2.1.6 and 2.1.7). In each analysis, it has mixed different geometry configurations to reach the best case, including modifications between the different cases (see section 2.1.1).

To carry out this study it has been developed a thorough study in the BEW area, which has changed the geometry, radius and incorporated stiffeners on the top and bottom of the plate, continuing to establish contact just to the BEW. Figure 2.2 shows different developments, including a gap at the back of the component as a safety measure, so that, all sectors are in contact if any cooling blockage occurs in one of them. For this study, it has been varied the curvature radius in the BEW, improving the He flow and causing a high stress reduction in that zone (down to close 20 MPa). A stiffener is included, due to high and unfeasible stress values that are produced at certain points (reaching stresses close to 480 MPa), so the achieved stiffener relieves these stresses and creates a solid support, so the component has a good consistency. In any case the design should not exceed the RCC-MRx[3] acceptance

criteria values, see Table 2.1.2.

The material of the pressure container will be SS-316L, annealed austenitic stainless steel with controlled nitrogen content. As the primary loading on the container is the pressure, only this physical boundary condition was taken into account.

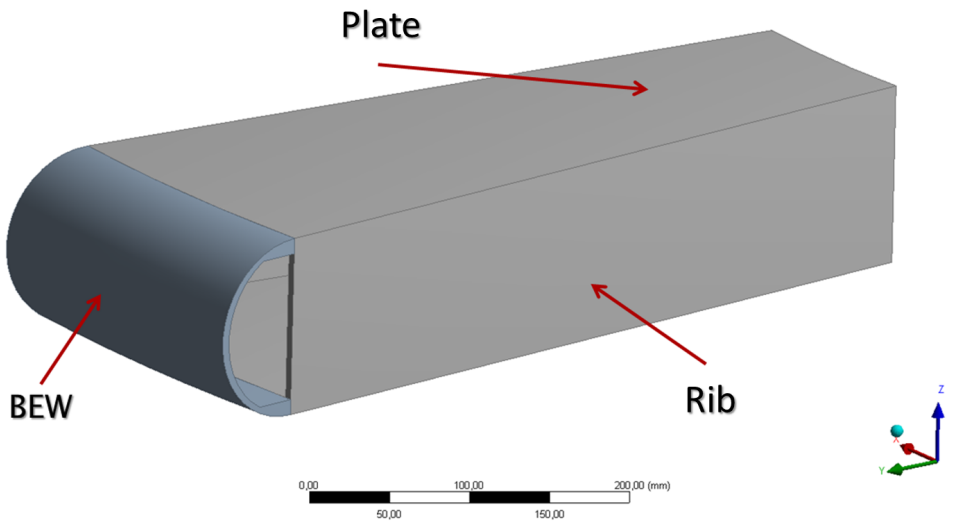

Figure 2.1: Geometry of the shroud with material assignment

In the following subsections geometry, different loads, boundary conditions, material properties and different studies for several sectors are described.

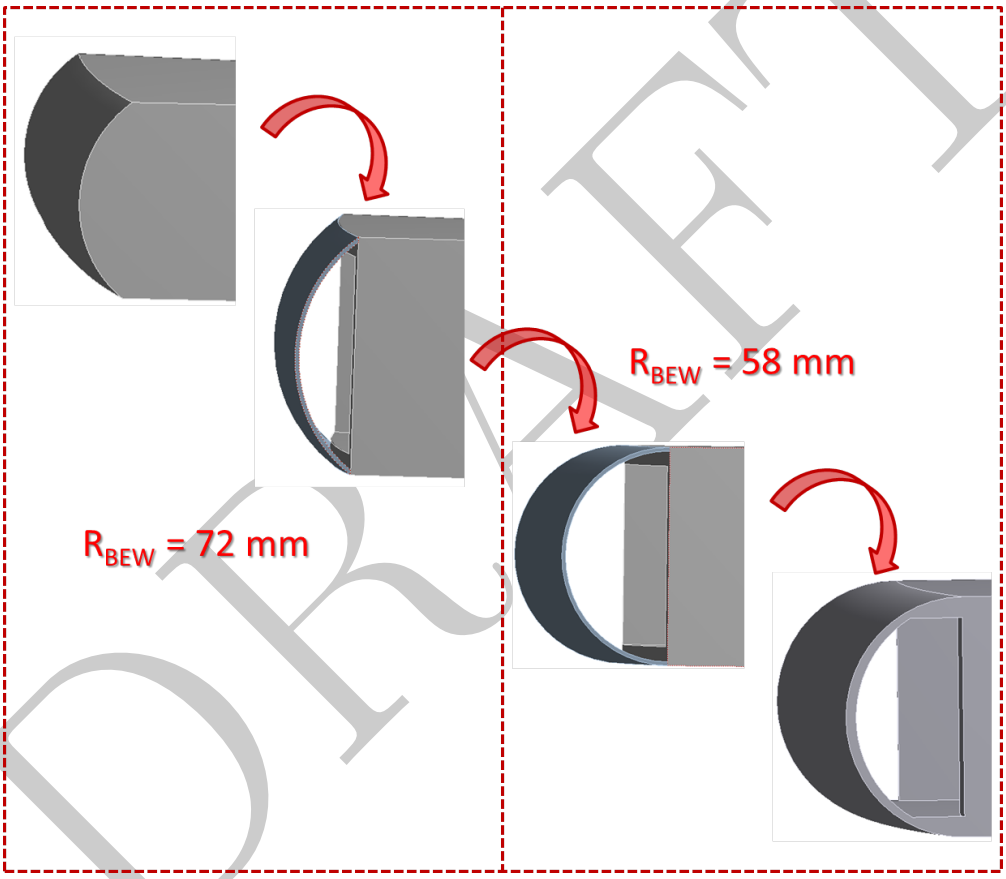

Figure 2.2: Evolution of the BEW geometry. The stiffener and the BEW are manufactured in a single peace and it is welded to the shroud.

2.1.1 Shroud geometry

To assess mechanical behavior of the structure, several geometries have been considered. Differences between them are the thickness in the plate, including a gap in the BEW, varying the radius of the BEW, including a stiffener in the BEW-plate connection and without stiffeners.

Figures 2.3 and 2.4 show the complete sector geometry. Figures 2.5 and 2.6 show target sector with gap geometry and with a radius of r_{BEW}=72 mm. Figures 2.7 and 2.8 show target sector with gap geometry and with a radius of r_{BEW}=58 mm. Figures 2.9 and 2.10 show target sector with gap geometry, with a radius of r_{BEW}=58 mm and considering stiffeners which establishes the contact from the BEW to the plate. These figures show two sectors to make it look how the share the rib.Figure 2.11 shows the target sector without ribs, with a radius r_{BEW}=72 mm.

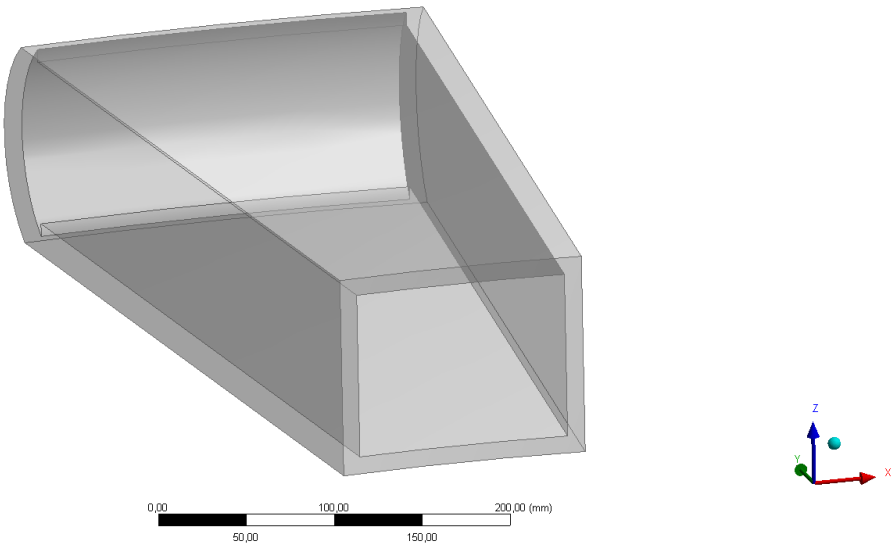

Figure 2.3: Complete design sector (r_{BEW}=72 mm)

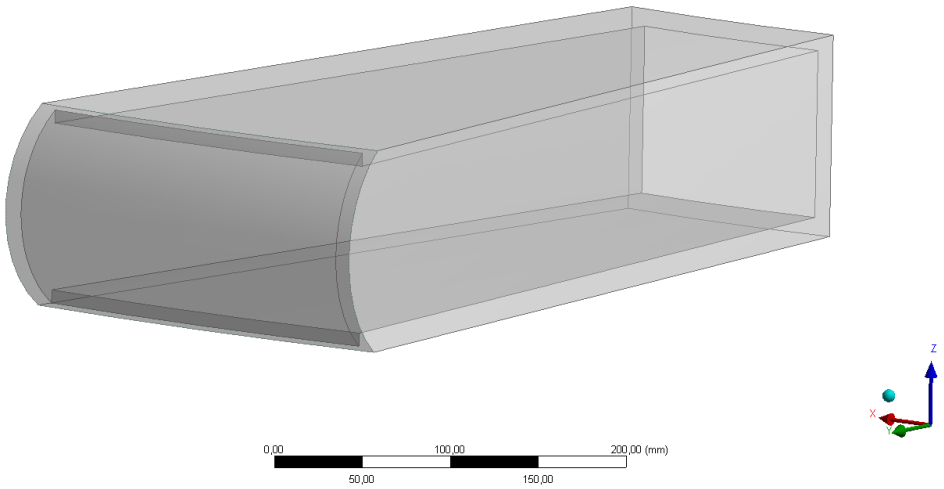

Figure 2.4: View of the BEW complete design sector (r_{BEW}=72 mm)

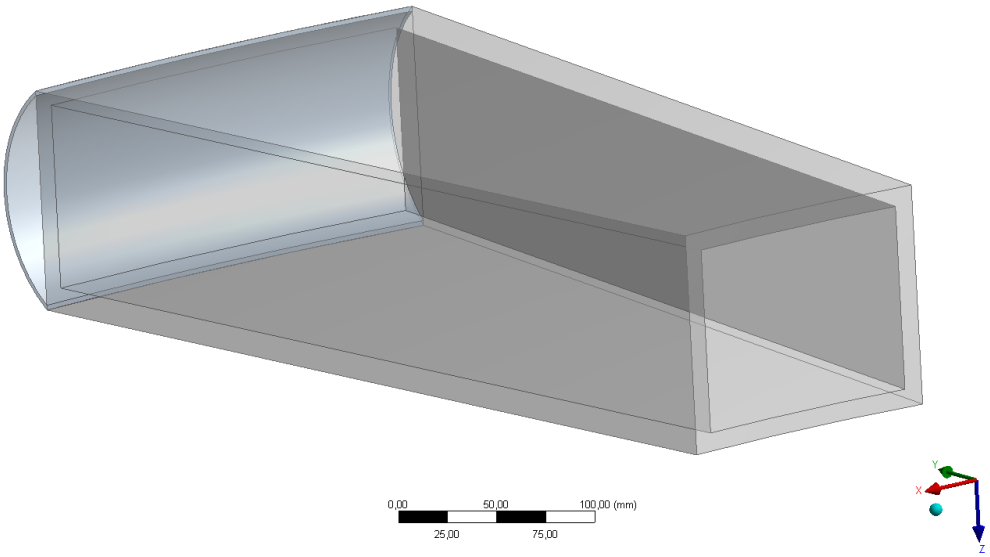

Figure 2.5: Design with gap included (r_{BEW}=72 mm)

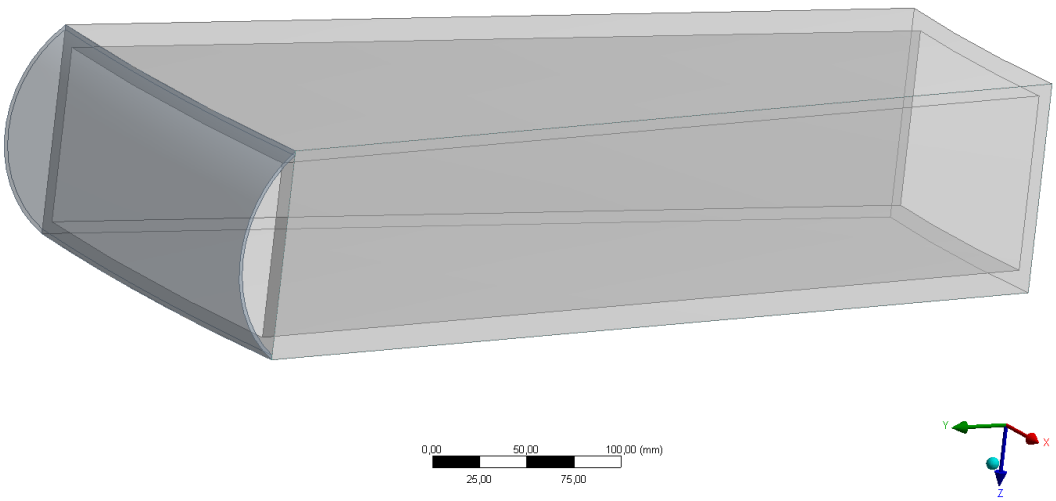

Figure 2.6: View of the BEW design with gap included (r_{BEW}=72 mm)

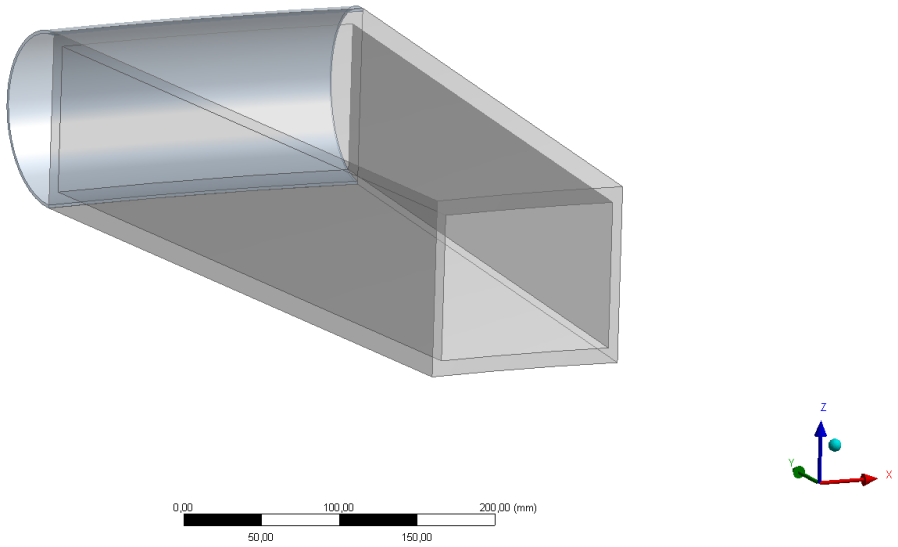

Figure 2.7: Design with gap included (r_{BEW}=58 mm)

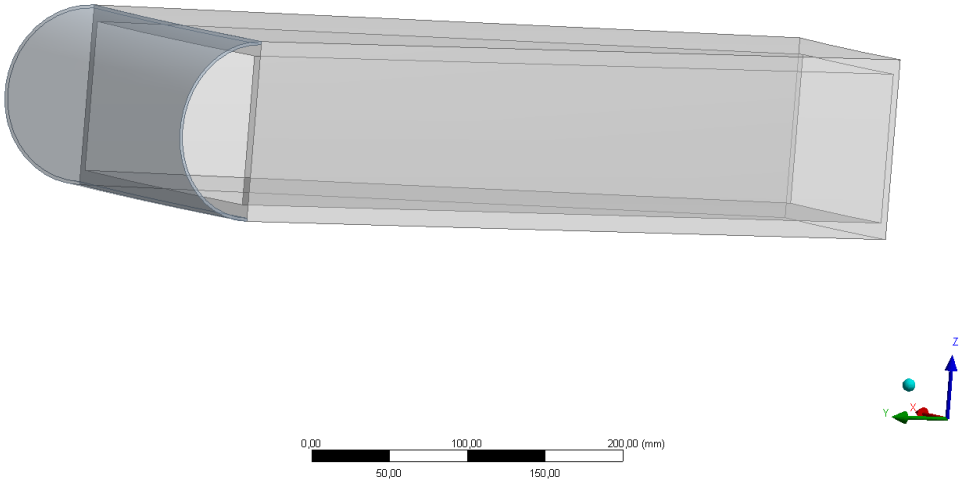

Figure 2.8: View of the BEW design with gap included (r_{BEW}=58 mm)

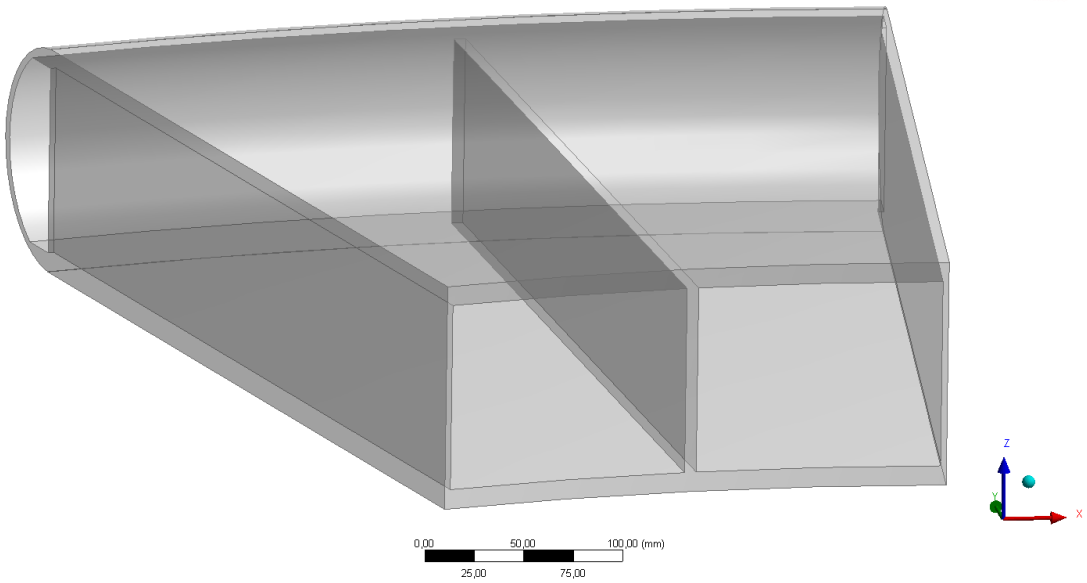

Figure 2.9: Design with gap and stiffener included, rib sharing (r_{BEW}=58 mm)

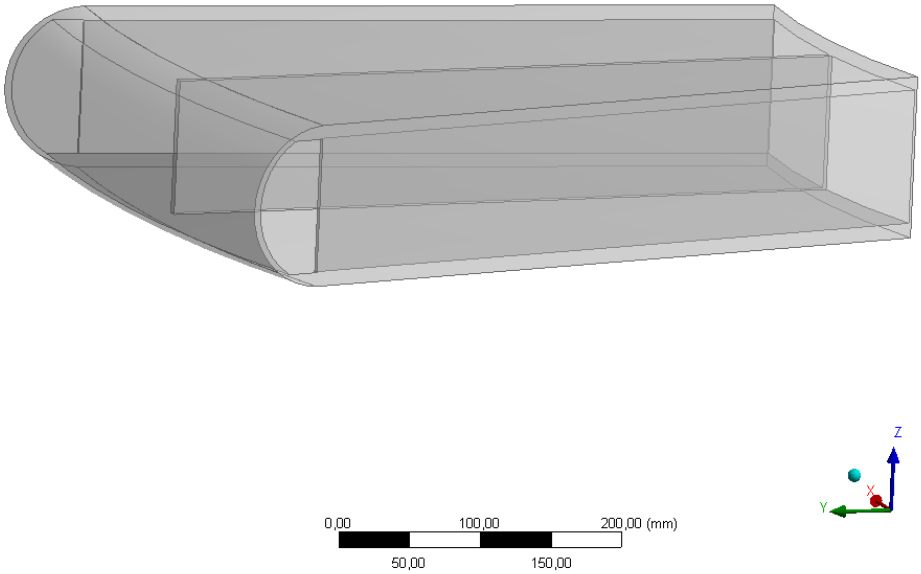

Figure 2.10: View of the BEW design with gap and stiffener included, rib sharing (r_{BEW}=58 mm)

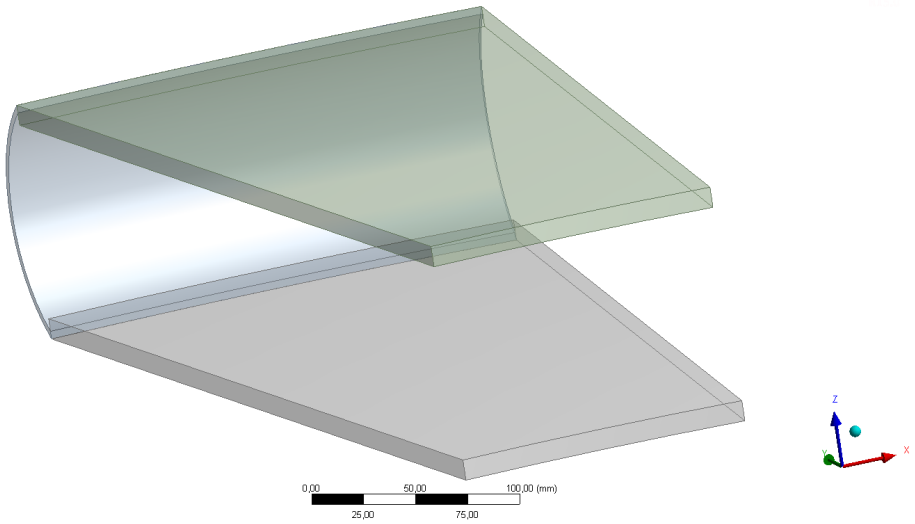

Figure 2.11: Design of the shroud without stiffeners

2.1.2 Primary loads and boundary conditions

This analysis focuses only on primary loads during normal operating conditions. Secondary loads coming from thermal conditions are not considered in this study and they will be assessed in later chapters. Figure 2.12 shows the several primary loads including in the target sector.

The structural loads are the following:

- Rotational velocity: 24-25 RPM
- Earth gravity: 9.81 m/s^2
- Outer pressure: 1 bar
- Inside pressure: 13 bar
- Design pressure ΔP: 12 bar
- Cassette weight: 101.94 kg
- Fixed support

Mechanical criteria for the vessel come from the RCC-MRxMx code. Table 2.1.2 shows these criteria considering in the three first rows only primary loads and in the last two rows a combination between primary and secondary loads:

Criterion	**Value (MPa)**	
	BEW	Shroud
P_m	123	123
P_L	184.4	184.4
P_L+P_b	184.4	184.5
P_m+Q_m	415	415
P_L+P_b+Q+F	851.5	851.5

Table 2.1: Criterion used for mechanical design

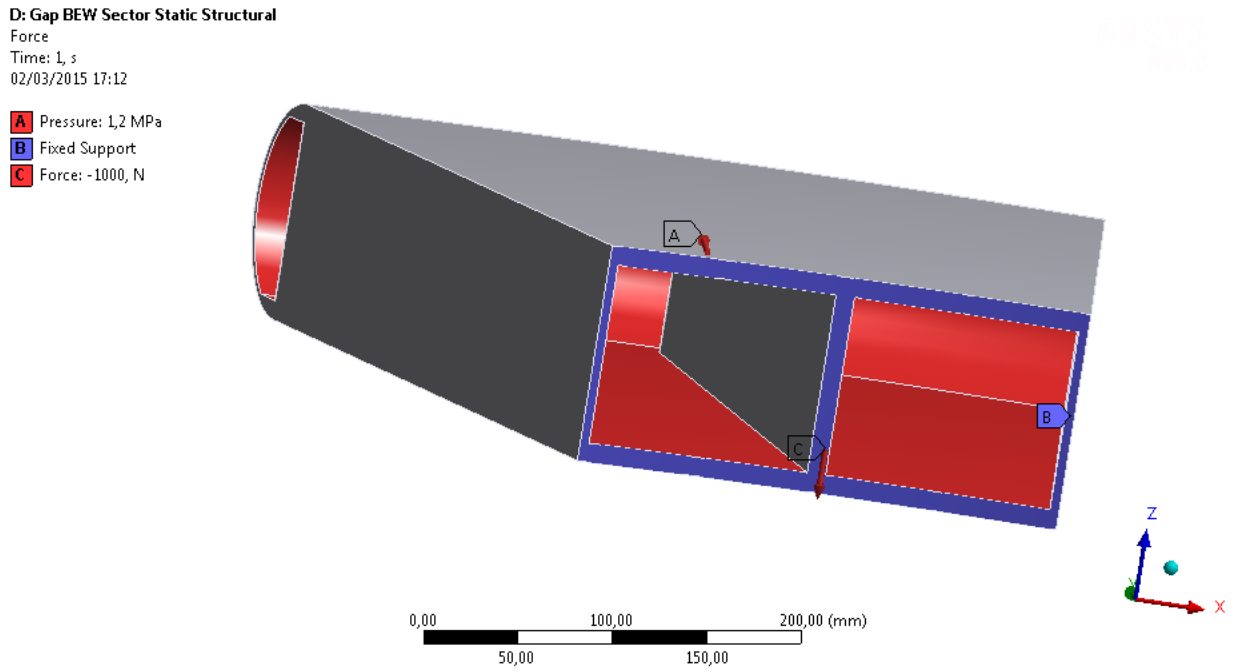

Figure 2.12: Primary loads in the target sector

2.1.3 Material properties

The material used to perform this mechanical study is austenitic SS-316L. As it will be seen later, the BEW reaches a temperature value close to 160°C and the shroud (without BEW) reaches a maximum temperature close to 80°C. So, main properties in operating conditions are the following:

- Thermal expansion, Figure 2.13:
  - Shroud: $1.57 \cdot 10^{-5}$ (C^{-1})
  - BEW: $1.62 \cdot 10^{-5}$ (C^{-1})
- Young modulus, Figure 2.14
  - Shroud: $2.1275 \cdot 10^{11}$ Pa
  - BEW: $2.0675 \cdot 10^{11}$ Pa
- Poisson ratio, Figure 2.15
  - Shroud: 0.272
  - BEW: 0.279
- Bulk modulus, Figure 2.16
  - Shroud: $1.5424 \cdot 10^{11}$ Pa
  - BEW: $1.5524 \cdot 10^{11}$ Pa
- Shear modulus, Figure 2.17
  - Shroud: $8.3349 \cdot 10^{10}$ Pa
  - BEW: $8.05 \cdot 10^{10}$ Pa

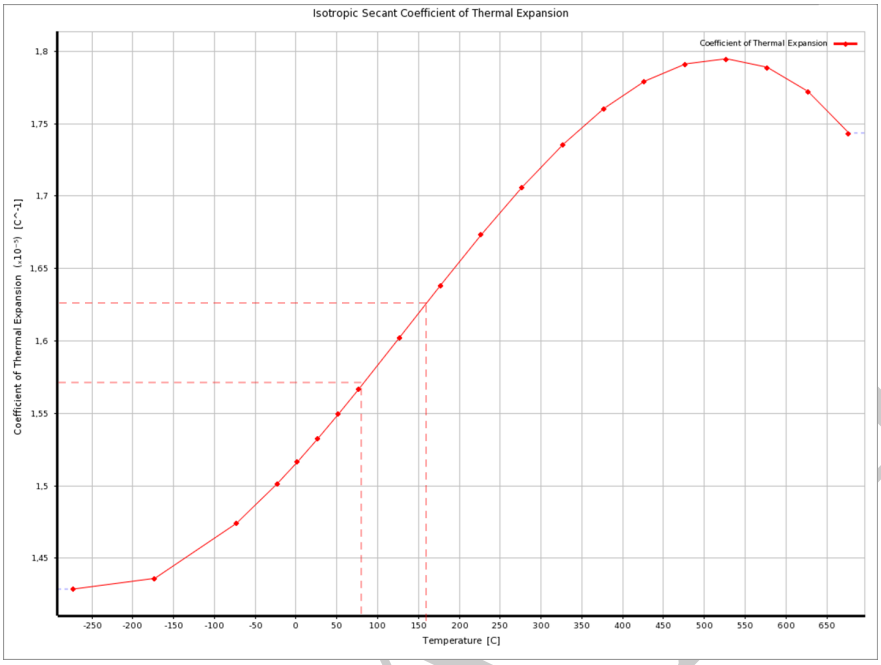

Figure 2.13: Coefficient of thermal expansion

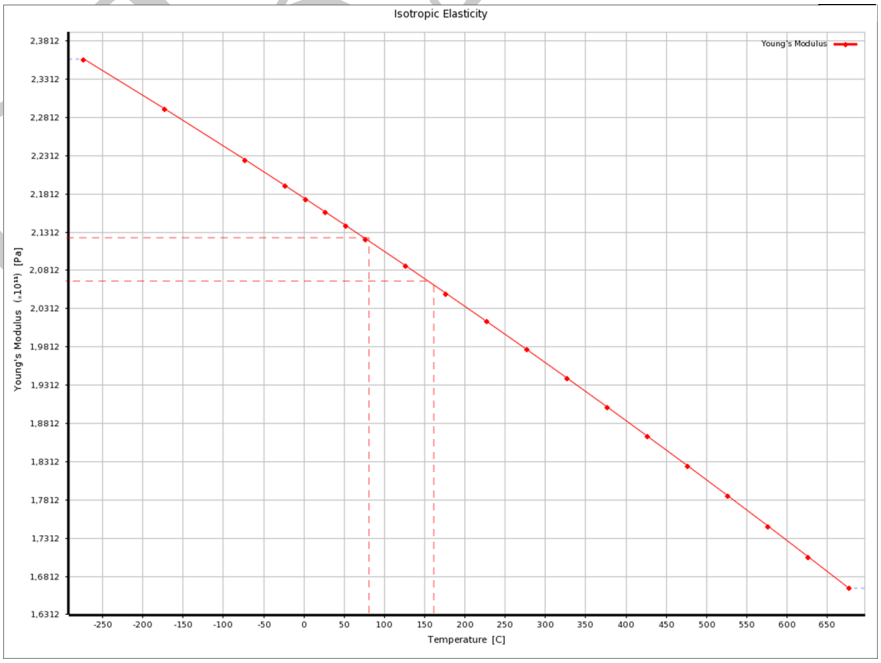

Figure 2.14: Young modulus

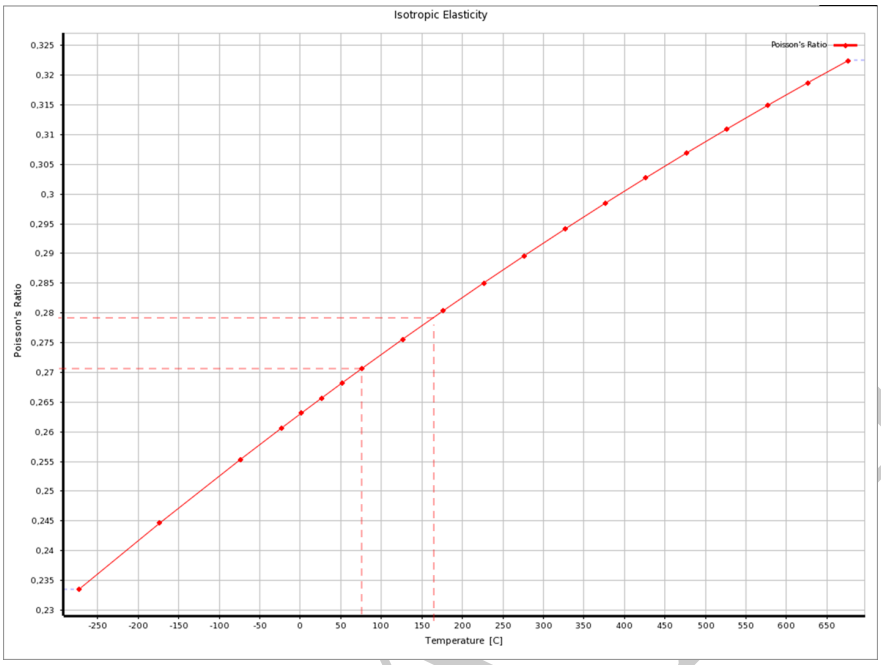

Figure 2.15: Poisson ratio

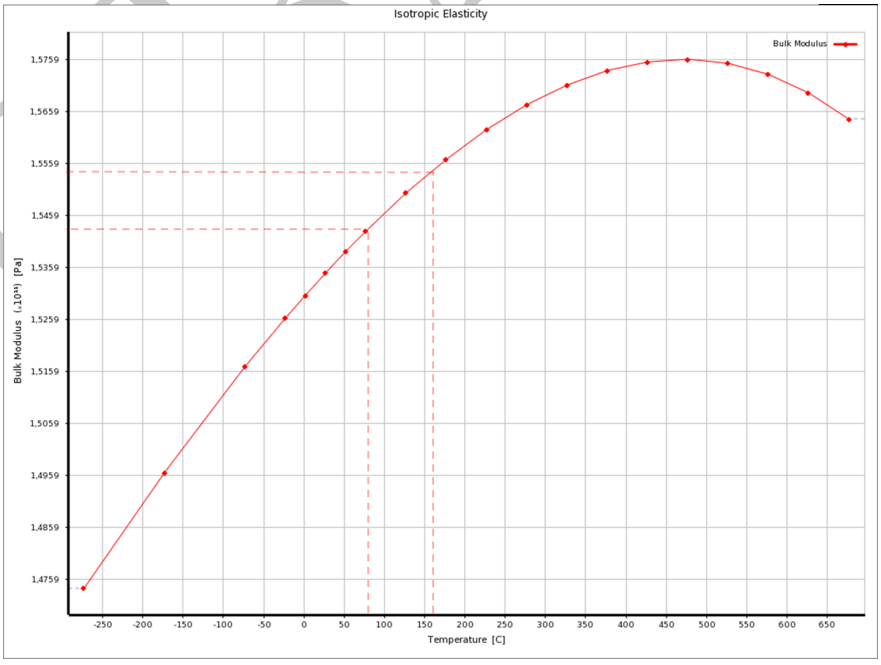

Figure 2.16: Bulk modulus

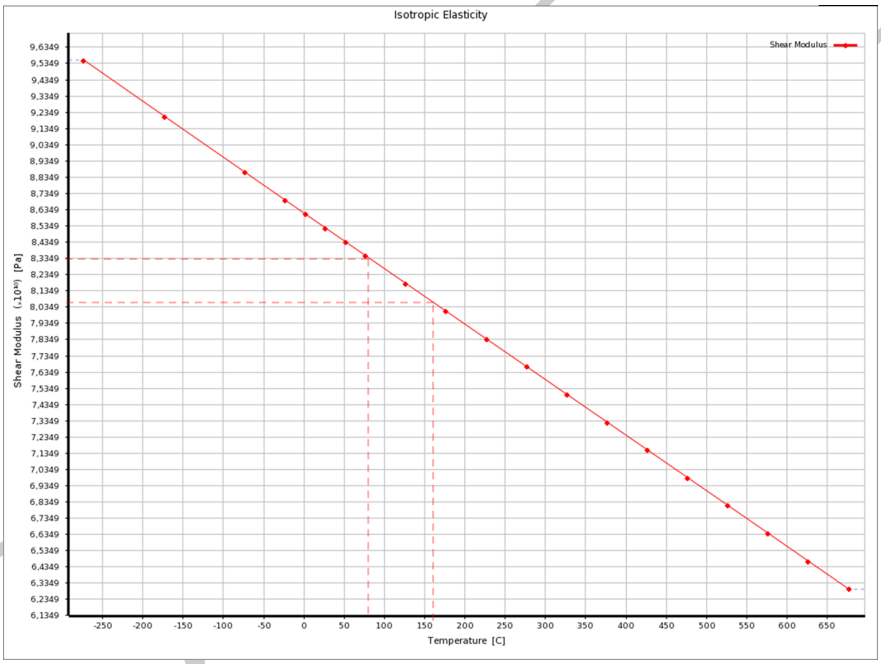

Figure 2.17: Shear modulus

2.1.4 Shroud with 33 target sectors

This section is divided in:

- Complete sector
- Sector with gap in the BEW

Complete sector

The angle of this sector is 10.90909°and the radius value of the BEW is 72 mm, Figures 2.3 and 2.4. The hexa mesh density in this case can be taken from Figure 2.18. The structure consists of a total of 130,119 elements and 578,119 nodes.

To carry out this study, it has been developed a sensitivity analysis changing the thickness in two components of the shroud: the plate and the rib. Global results are shown in Figure 2.19. It has simulated in this section 12 cases, changing the thickness parameters, and in the Figure it shows the Von-Mises stress in each case.

The optimized case for this study is the **case 9** (plate and rib thickness = 10 mm) with an Equivalent Von-Mises Stress value of 165.53 MPa, see Figure 2.20 and a total deformation in the top of the plate is less than 0.54 mm, see Figure 2.21.

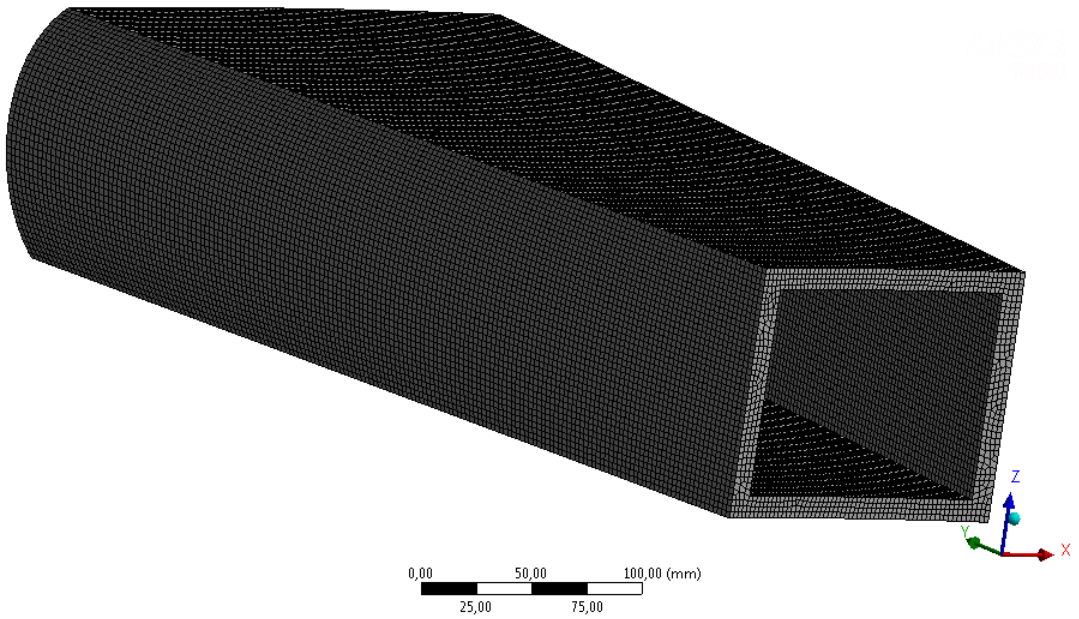

Figure 2.18: Mesh of the shroud with 33 (r_{BEW}=72 mm). Complete sector

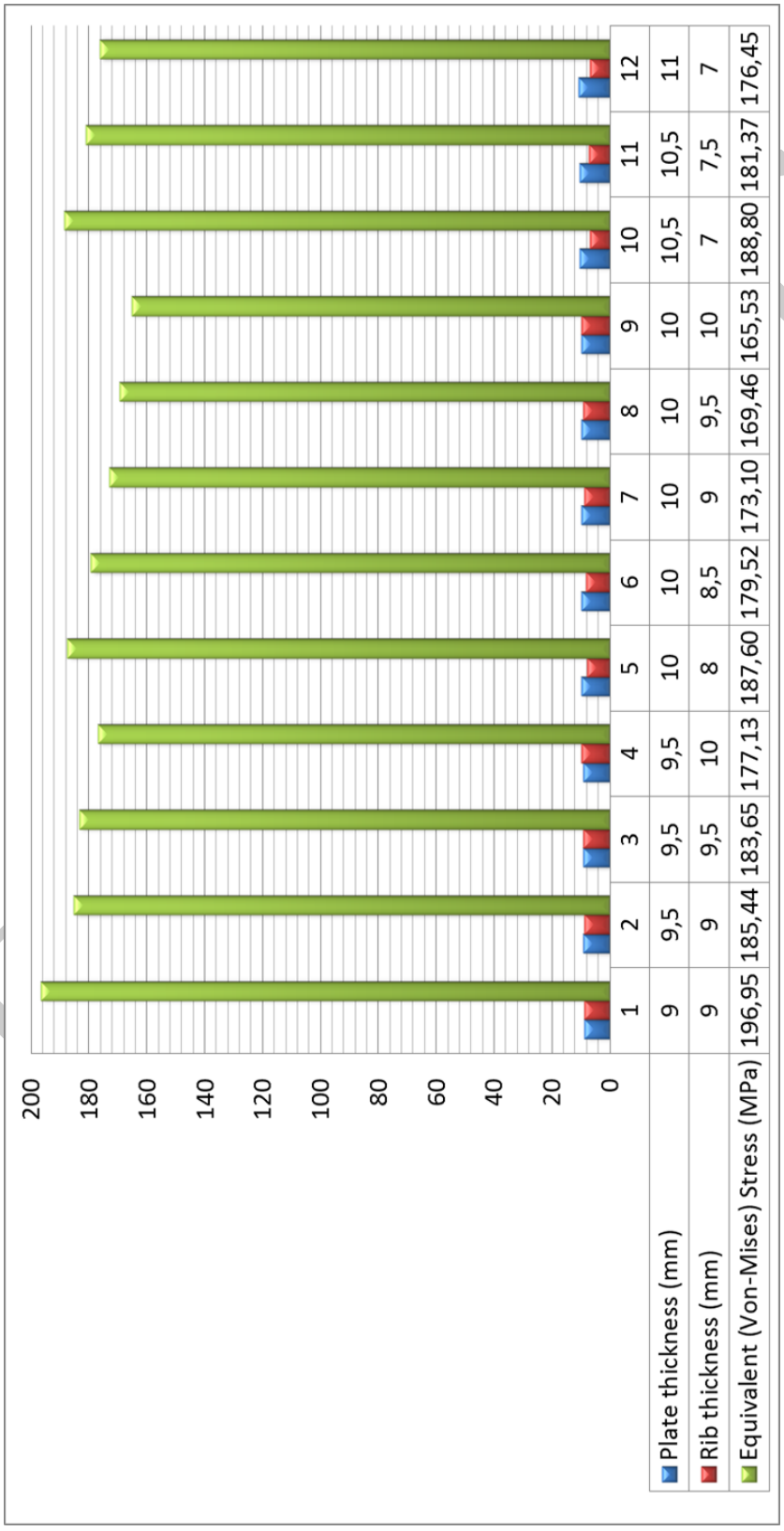

Figure 2.19: Global results with 33 target sectors (r_{BEW}=72 mm)

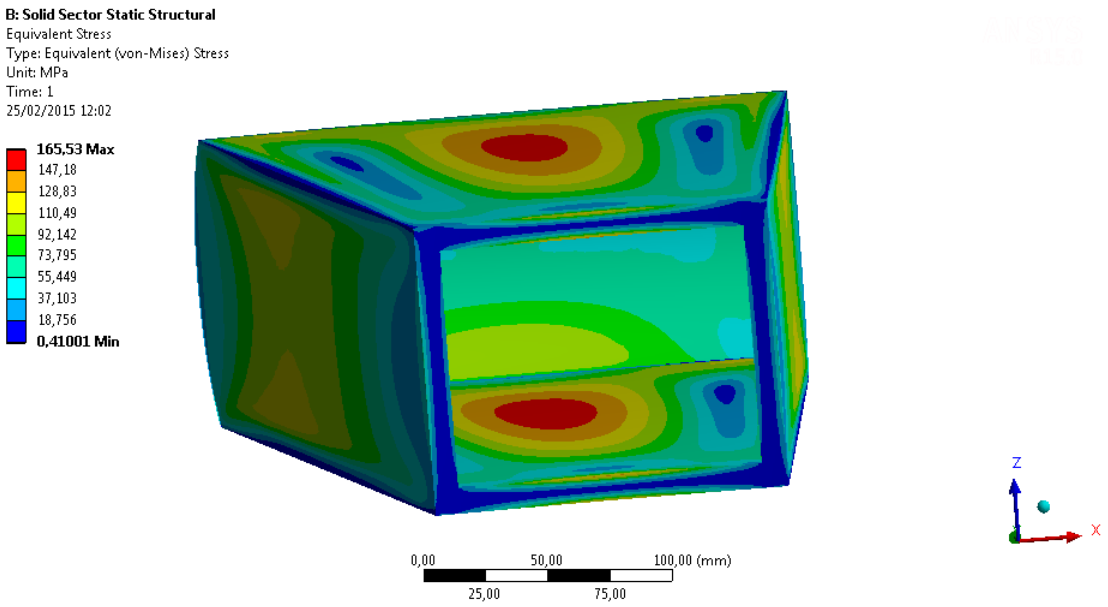

Figure 2.20: Equivalent stress in the shroud with 33 target sectors (r_{BEW}=72 mm)

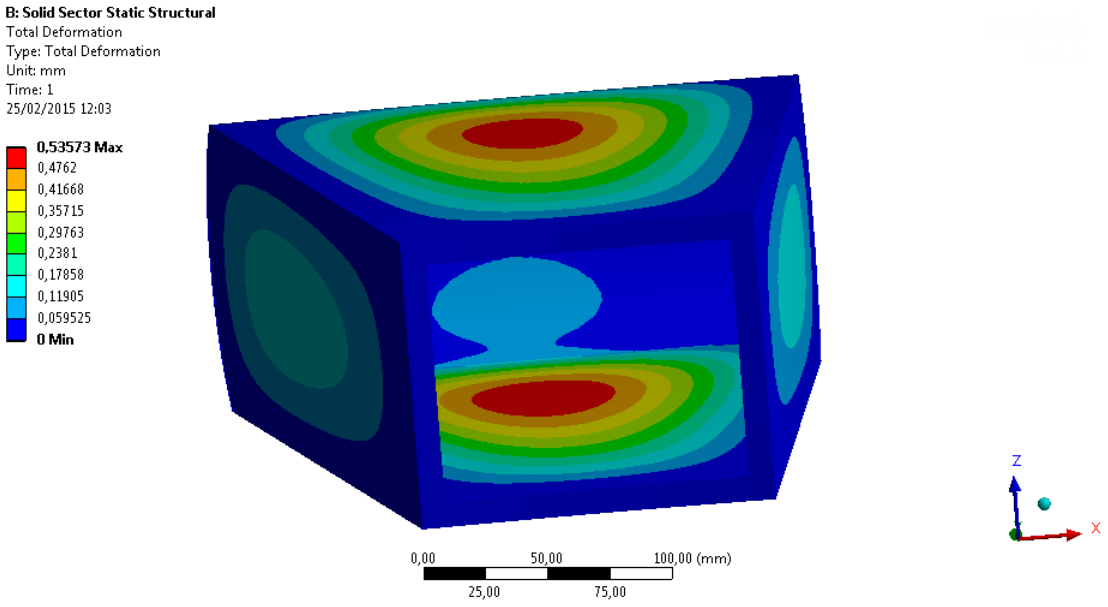

Figure 2.21: Total deformation in the shroud with 33 target sectors (r_{BEW}=72 mm)

Sector with gap in the BEW

This sector is the same as the previous one (same angle and radius), but including the gap in the end of the sector, close to the BEW, see Figures 2.5 and 2.6. Mesh density is shown in Figure 2.22 and consists of a total of 125,378 elements and 600,131 nodes.

It has developed a parametric analysis changing the thickness of the plate and the rib. Global results are shown in Figure 2.23.

The optimized case for this study is the **case 5** (plate and rib thickness = 10 mm) with an Equivalent Von-Mises Stress value of 181.01 MPa in the welding area, see Figure 2.24 and a total deformation in the top of the plate is less than 0.54 mm, see Figure 2.25. It has been performed a path analysis in several parts of the shroud, see Figure 2.26. Path analysis results of the case 5 are shown in Figure 2.27. In all paths, stress valuers are below the criteria established by RCC-MRxMx for primary loads.

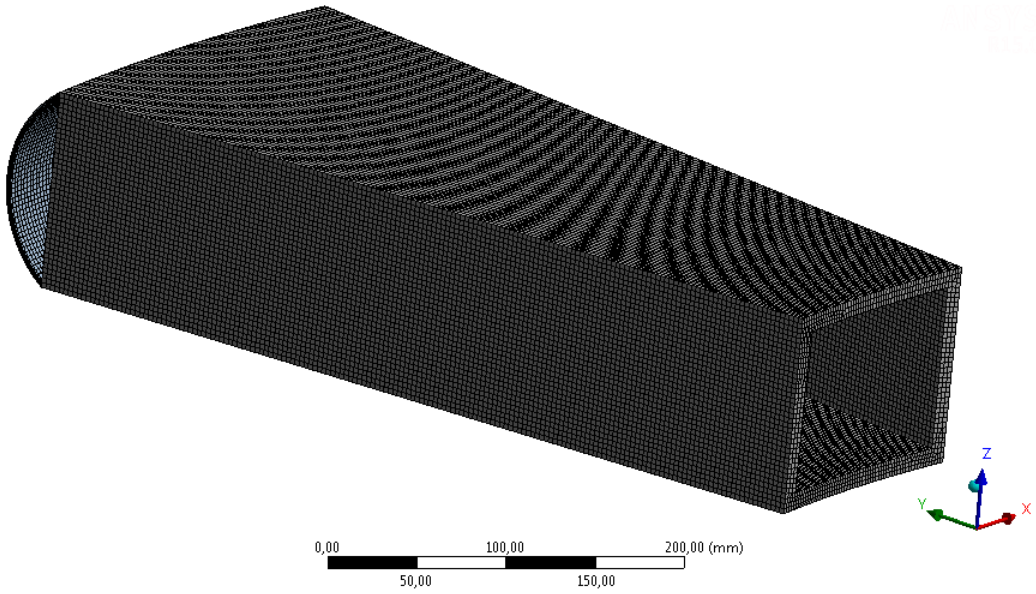

Figure 2.22: Mesh of the shroud with 33 sectors and gap in the BEW (r_{BEW}=72 mm)

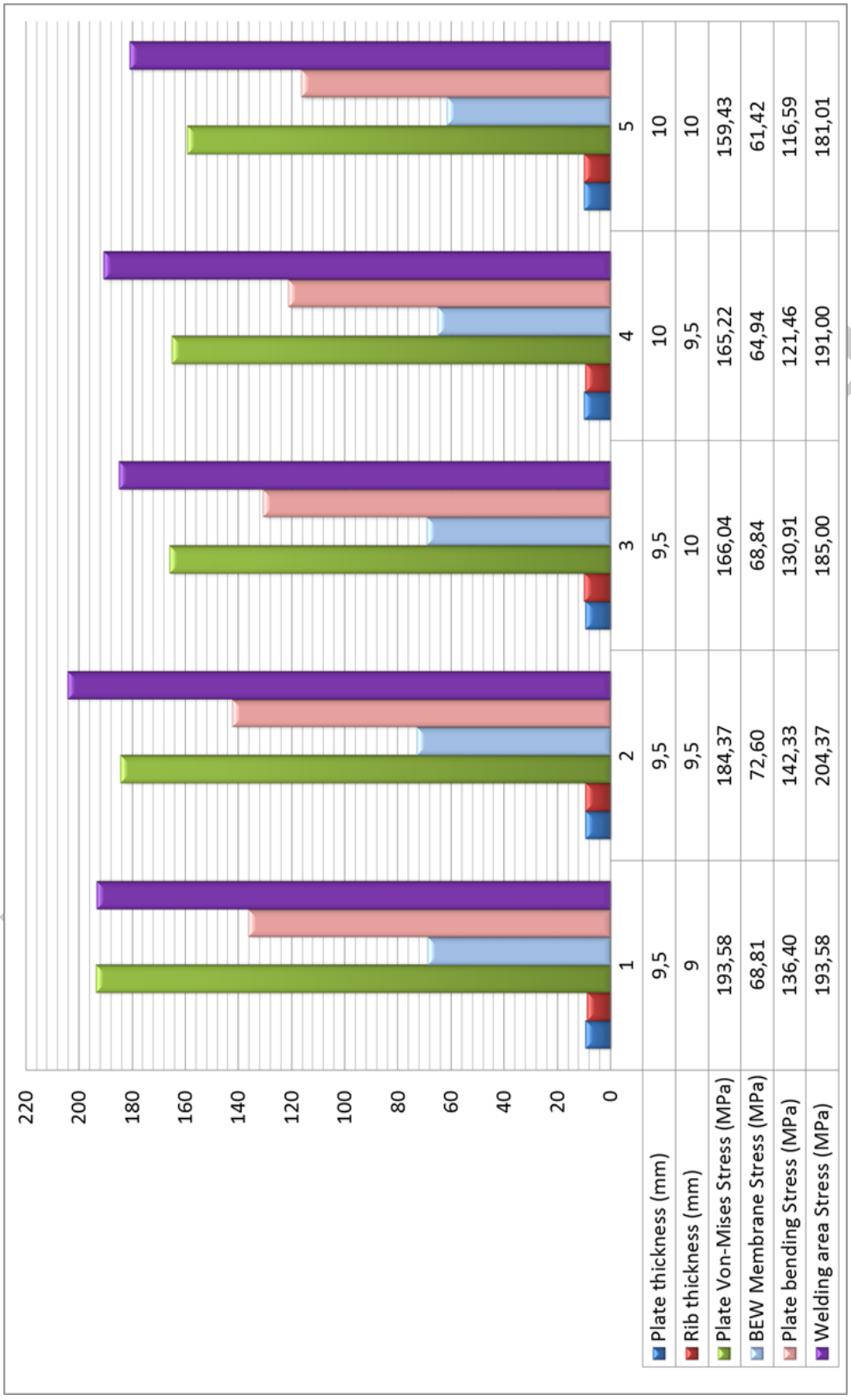

Figure 2.23: Global results with 33 target sectors with Gap in the BEW (r_{BEW}=72 mm)

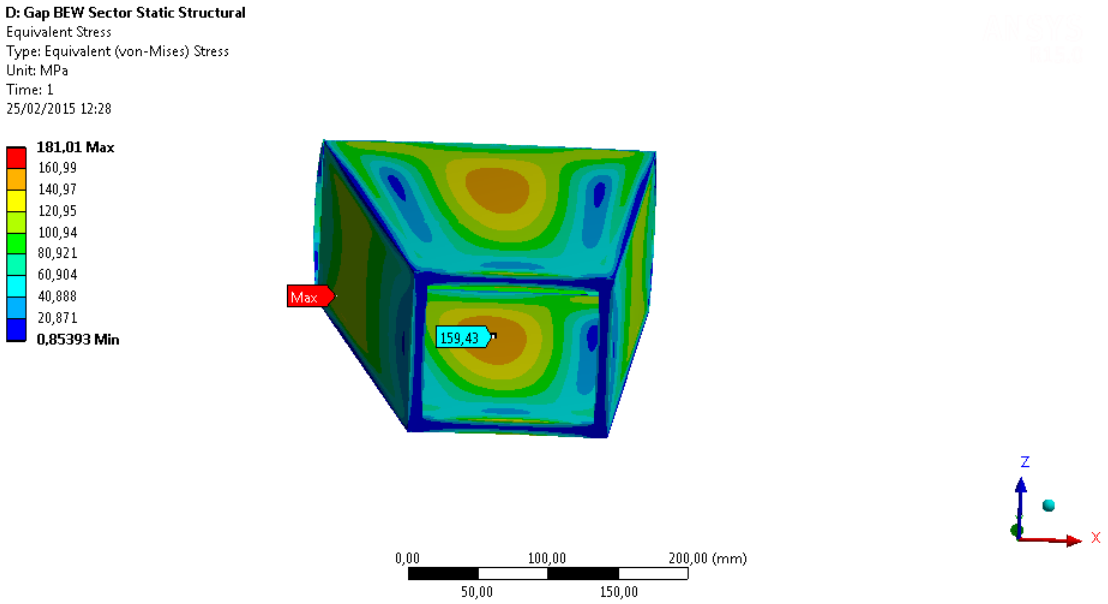

Figure 2.24: Equivalent stress in the shroud with 33 target sectors with gap in the BEW (r_{BEW}=72 mm)

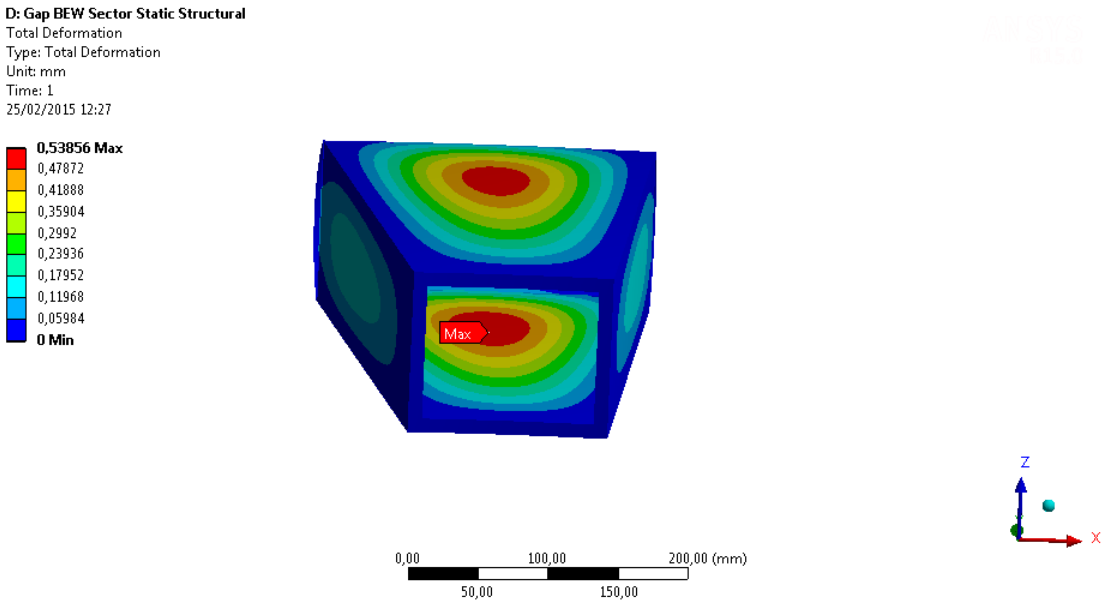

Figure 2.25: Total deformation in the shroud with 33 target sectors with gap in the BEW (r_{BEW}=72 mm)

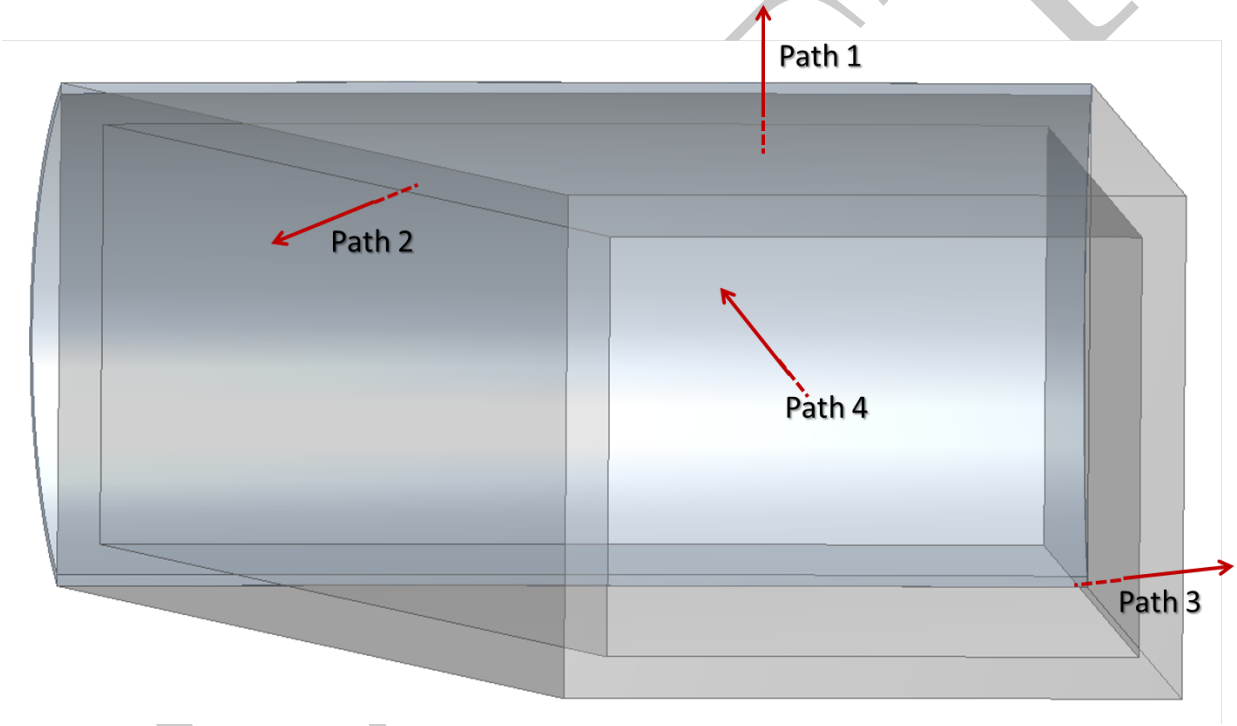

Figure 2.26: Path analysis with 33 target sectors with gap in the BEW (r_{BEW}=72 mm)

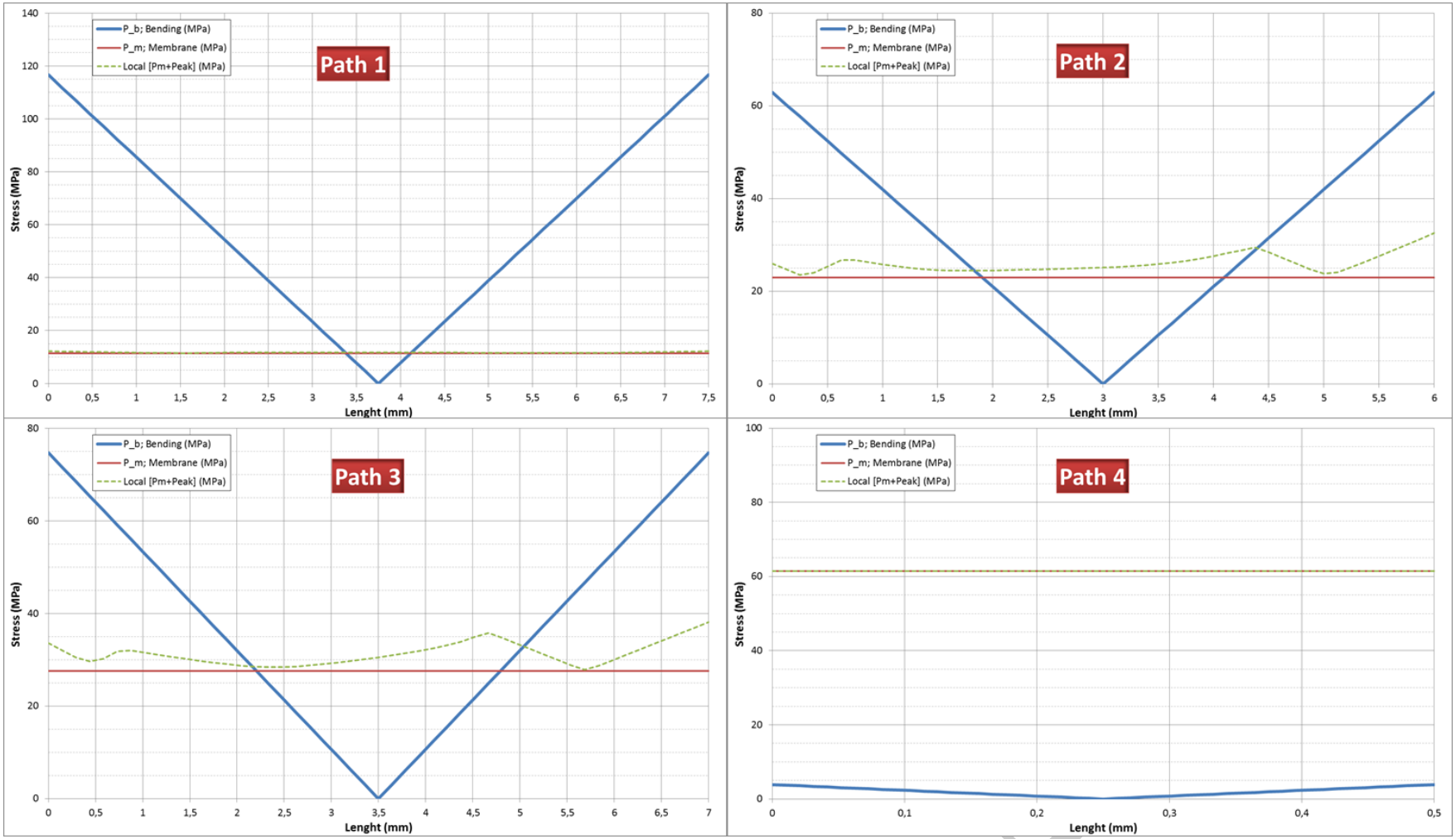

Figure 2.27: Results of the path analysis with 33 target sectors with gap in the BEW (r_{BEW}=72 mm). Case 5

2.1.5 Shroud with 36 target sectors

This section is divided in:

- Complete sector
- Sector with gap in the BEW, r_{BEW}=72 mm
- Sector with gap in the BEW, r_{BEW}=58 mm

Complete sector

This case is the same as section 2.1.4, but changing the angle of the sector, in this case is 10.00°, see Figures 2.3 and 2.4. Mesh density consists of 119,317 elements and 533,231 nodes (see Figure 2.28).

The results of the parametric analysis, varying thicknesses of the plate and the rib, are shown in Figure 2.19. For this study, it has simulated 12 cases, and most of them have acceptable values due to they are below the maximum value (184,5 MPa). The optimized case for this study (configuration and manufacturing) is the **case 8** (plate thickness = 10 and rib thickness = 7.5 mm) with an Equivalent Von-Mises Stress value of 170.74 MPa (see Figure 2.30) and a total deformation in the top of the plate is less than 0.54 mm, see Figure 2.31.

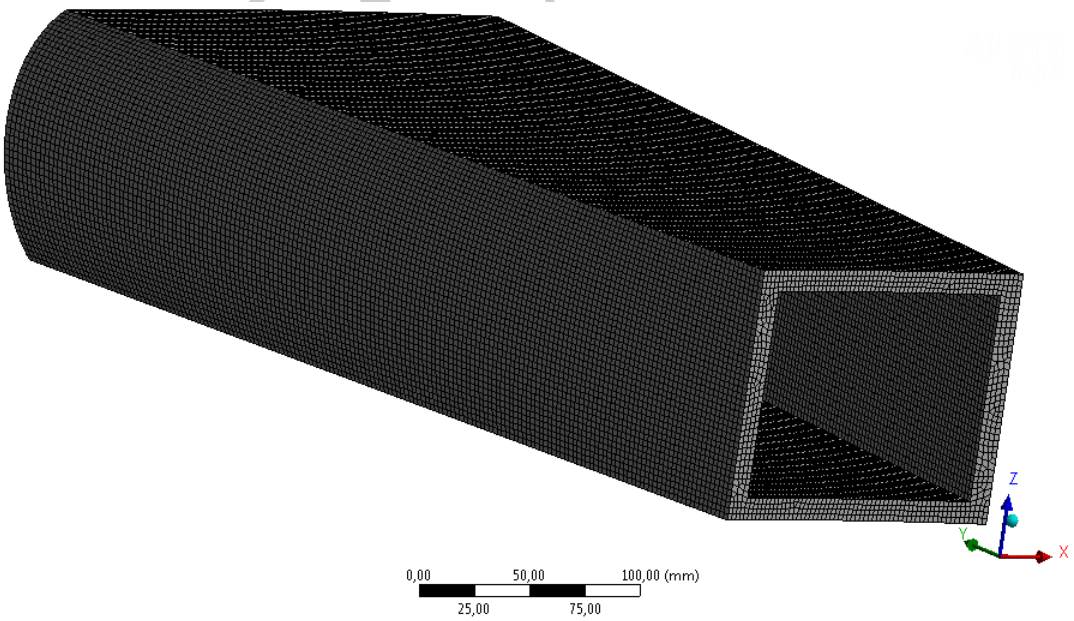

Figure 2.28: Mesh of the shroud with 36 (r_{BEW}=72 mm). Complete sector

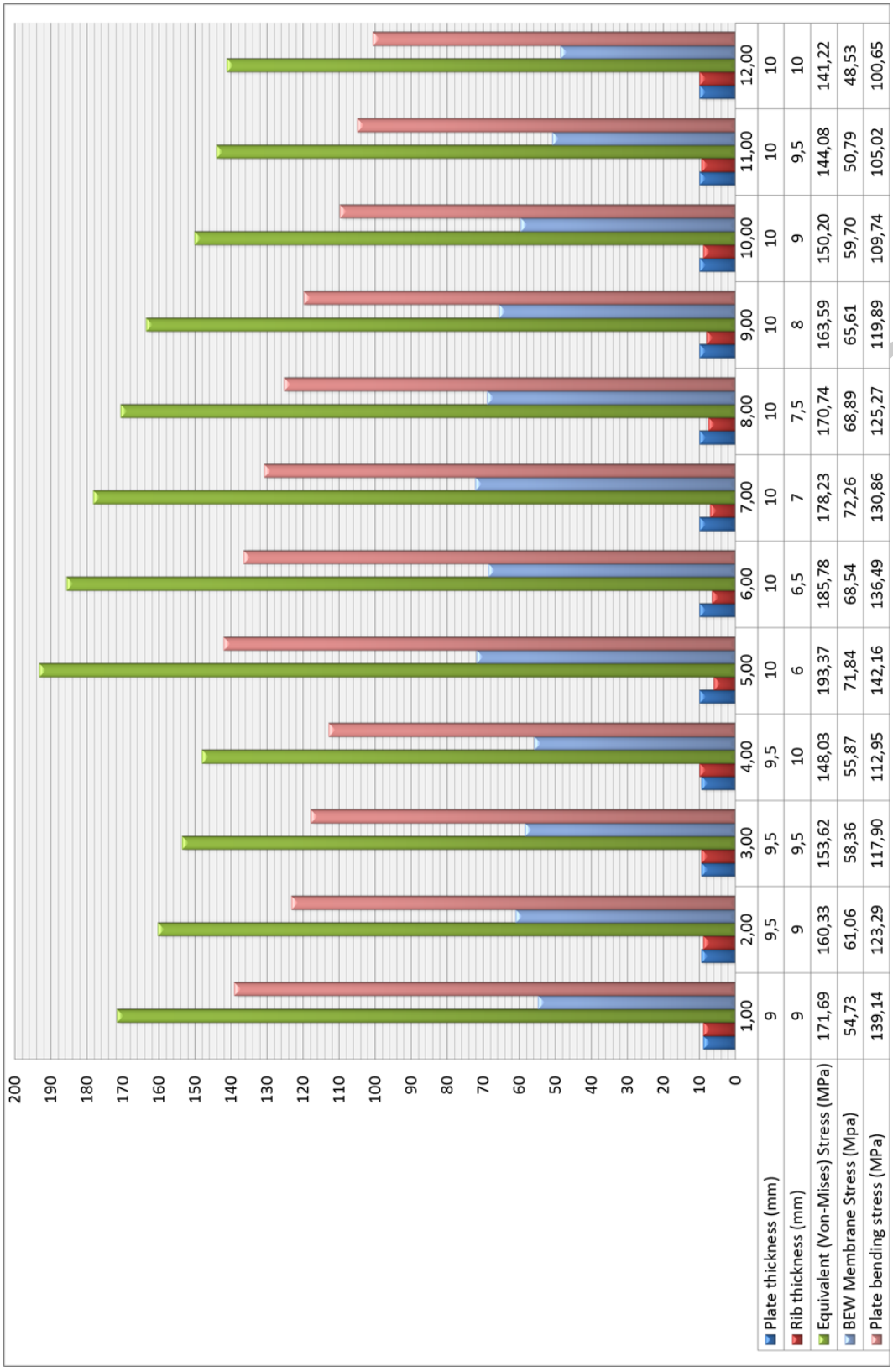

Figure 2.29: Global results with 36 target sectors (r_{BEW}=72 mm)

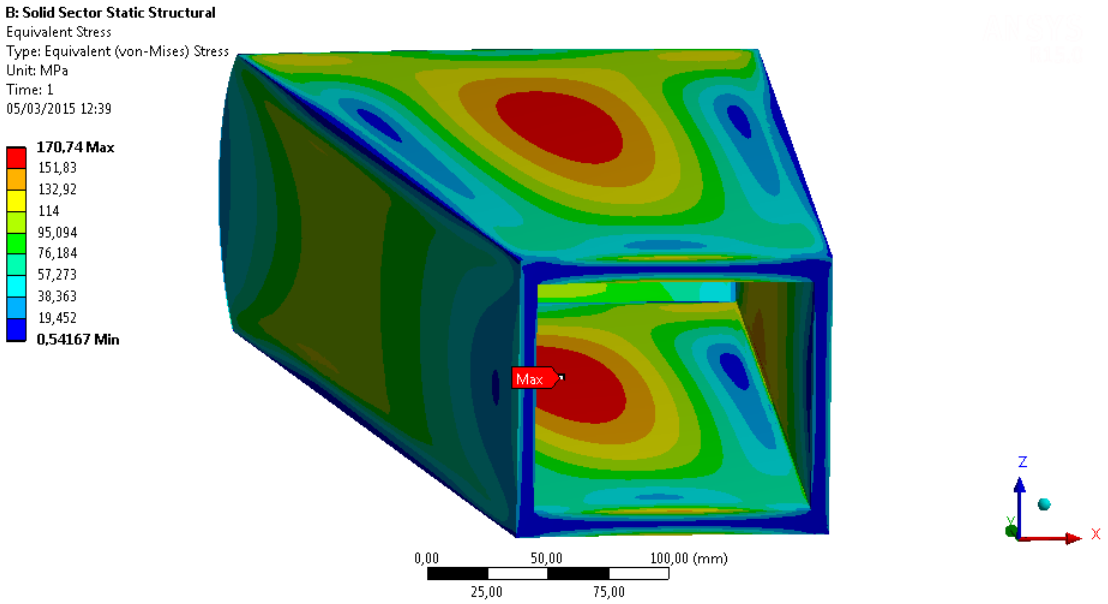

Figure 2.30: Equivalent stress in the shroud with 36 target sectors (r_{BEW}=72 mm)

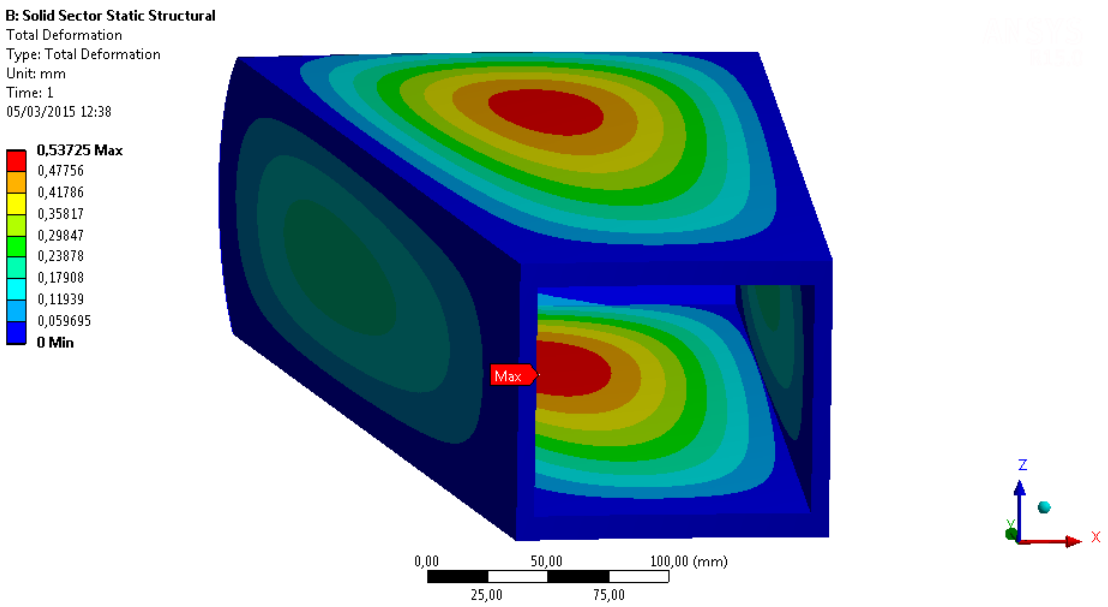

Figure 2.31: Total deformation in the shroud with 36 target sectors (r_{BEW}=72 mm)

Sector with gap in the BEW, r_{BEW}=72 mm

This study is the same as section 2.1.4 but modifying the angle (10.00°), see Figures 2.5 and 2.6. The hexa mesh density in this case can be taken from Figure 2.32 and consists of a total of 110,106 elements and 534,798 nodes, and it has performed the same analysis, modifying the thickness in the plate and rib. Global results are shown in the Figure 2.33. For this study, it has performed 12 cases, several of them have acceptable values.

The optimized case for this study is the **case 10** (plate thickness = 10 and rib thickness = 9 mm) with an Equivalent Von-Mises Stress value close to 176 MPa in the welding area, see Figure 2.34 and a total deformation in the top of the plate is less than 0.46 mm, see Figure 2.35.

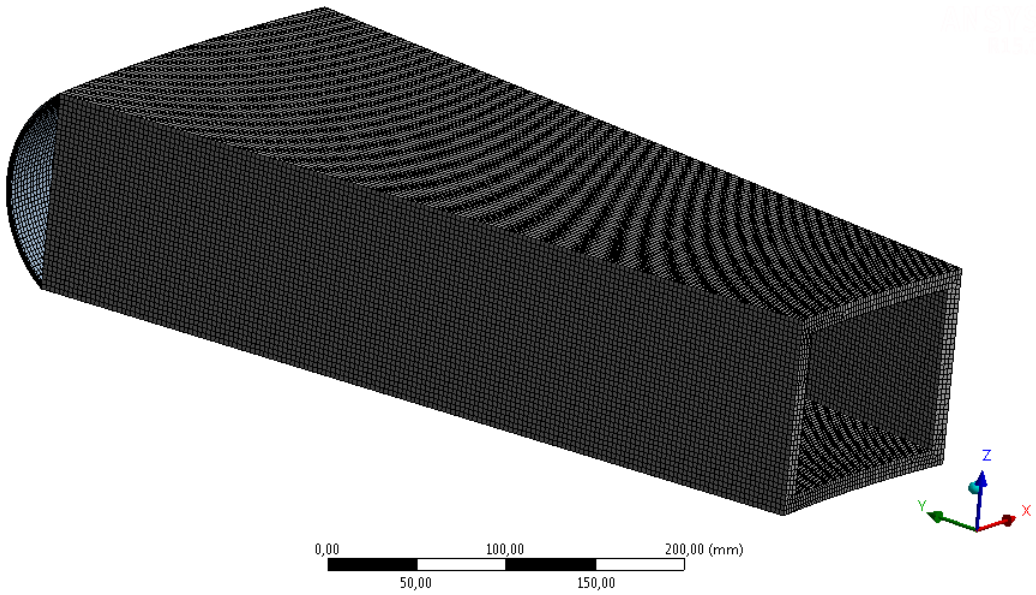

Figure 2.32: Mesh of the shroud with 36 sectors and gap in the BEW (r_{BEW}=72 mm)

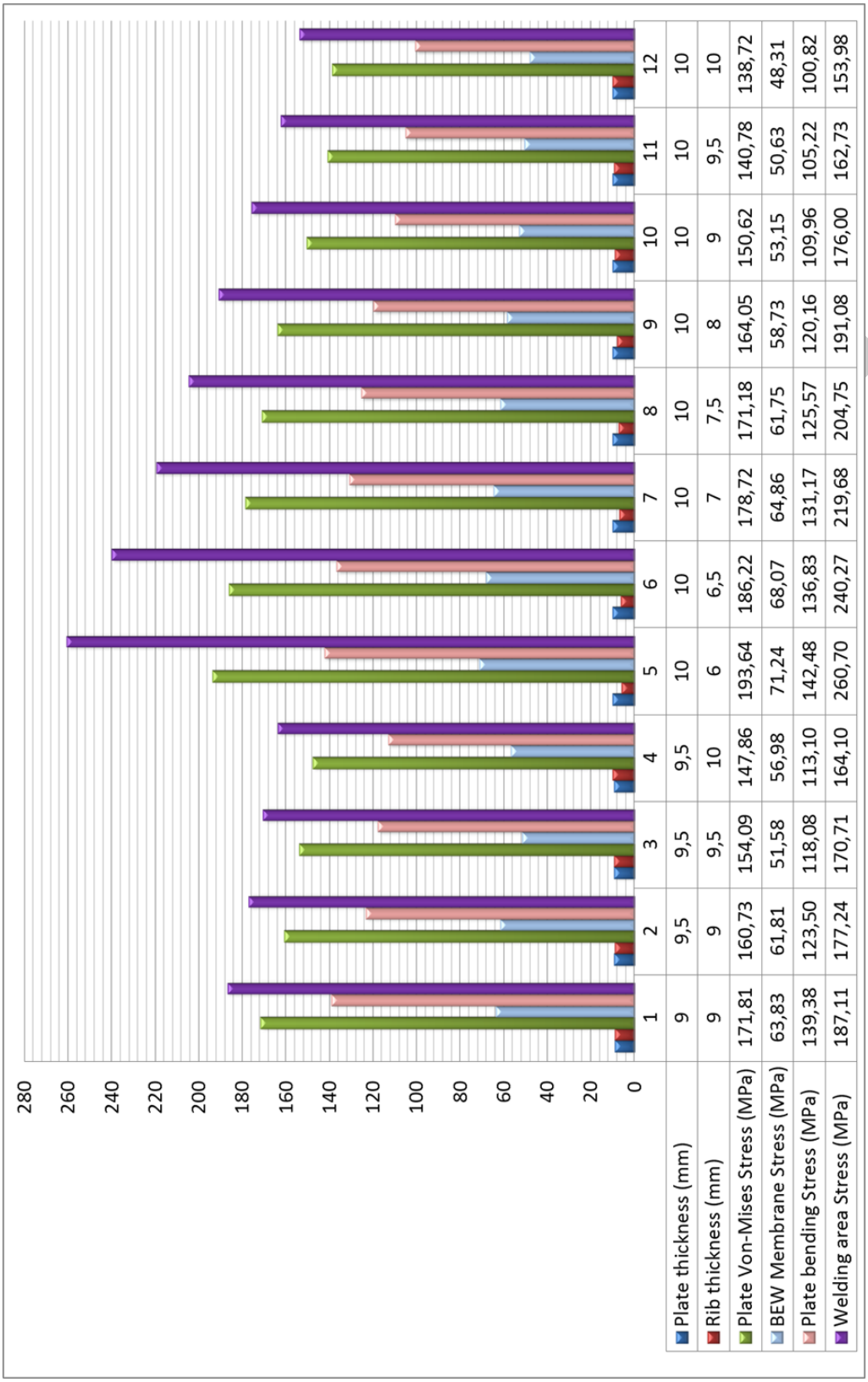

	1	2	3	4	5	6	7	8	9	10	11	12
Plate thickness (mm)	9	9,5	9,5	9,5	10	10	10	10	10	10	10	10
Rib thickness (mm)	9	9	9,5	10	6	6,5	7	7,5	8	9	9,5	10
Plate Von-Mises Stress (MPa)	171,81	160,73	154,09	147,86	193,64	186,22	178,72	171,18	164,05	150,62	140,78	138,72
BEW Membrane Stress (MPa)	63,83	61,81	51,58	56,98	71,24	68,07	64,86	61,75	58,73	53,15	50,63	48,31
Plate bending Stress (MPa)	139,38	123,50	118,08	113,10	142,48	136,83	131,17	125,57	120,16	109,96	105,22	100,82
Welding area Stress (MPa)	187,11	177,24	170,71	164,10	260,70	240,27	219,68	204,75	191,08	176,00	162,73	153,98

Figure 2.33: Global results with 36 target sectors with Gap in the BEW (r_{BEW}=72 mm)

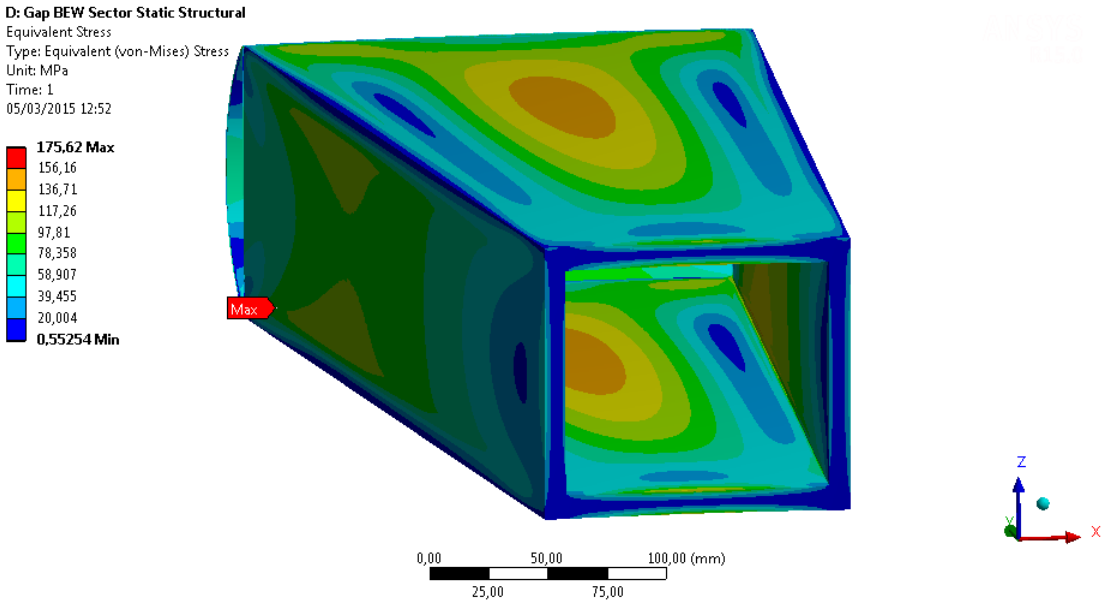

Figure 2.34: Equivalent stress in the shroud with 36 target sectors with gap in the BEW (r_{BEW}=72 mm)

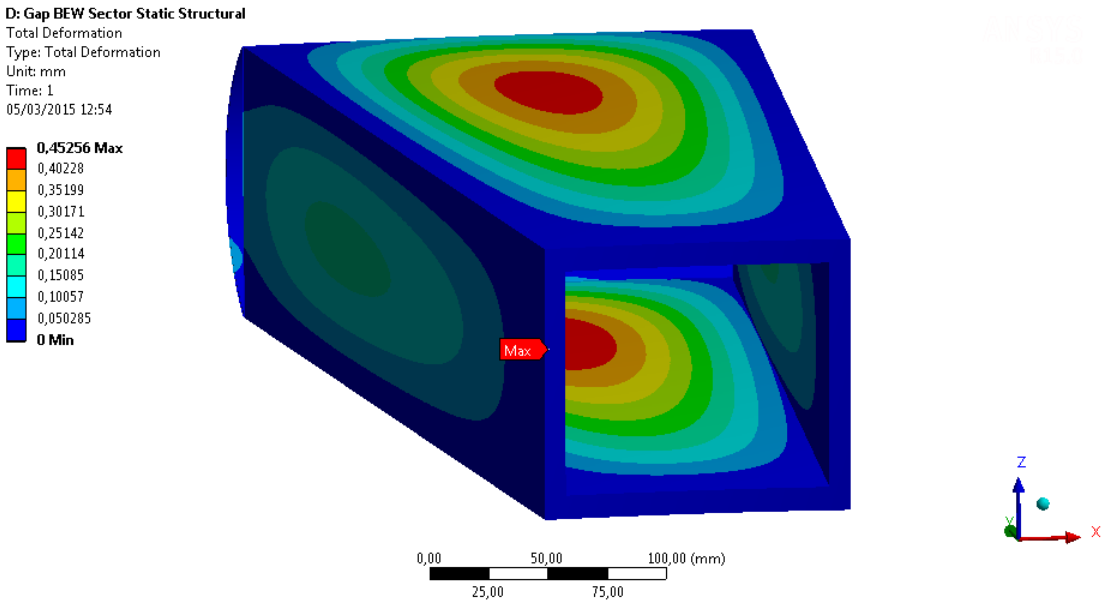

Figure 2.35: Total deformation in the shroud with 36 target sectors with gap in the BEW (r_{BEW}=72 mm)

Sector with gap in the BEW, r_{BEW}=58 mm

In this case the BEW radius has been modified to a value of 58 mm, Figures 2.7 and 2.8. Mesh density is 102,482 elements and 509,044 nodes (see Figure 2.36).

Equivalent Von-Mises Stress is too high (value of 477.1 MPa), in the welding area of the BEW, see Figure 2.37, and it exceeds the RCC-MRxMX criteria, Table 2.1.2. For this reason, it has been incorporated a stiffener which connects the BEW with the top plate (last step in Figure 2.2).

So a new analysis has been performed considering this stiffener between the BEW and the top plate (the geometries can be seen in Figures 2.9 and 2.10). The mesh for this model is 180,077 elements and 881,424 nodes. It is important to mention that for this new study the rib is shared between two consecutive sectors, this means that the sectors are not individuals components. Global results are shown in Figure 2.39, and it has simulated 18 cases.

The optimized case for this study is the **case 9** (plate thickness = 10 and rib thickness [each sector] = 5 mm) with an Equivalent Von-Mises Stress value of 175.41 MPa, see Figures 2.40 and 2.41, and a total deformation in the plate close to 0.25 mm, see Figure 2.42. It has been performed a path analysis in several parts of the shroud to assess carefully stress behavior in the component, see Figure 2.26. Path analysis results of the case 9 are shown in Figure 2.43.

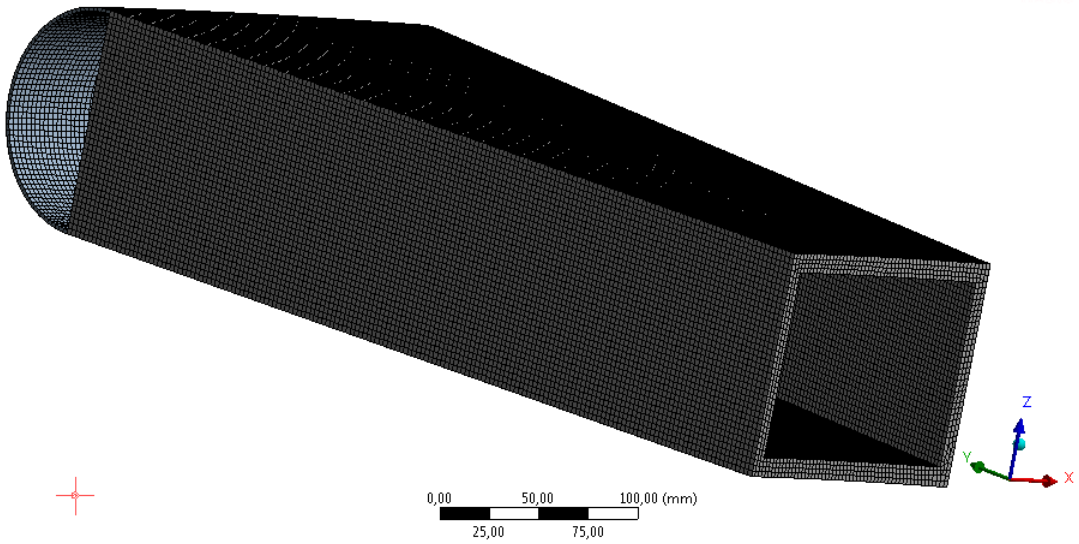

Figure 2.36: Mesh of the shroud with 36 sectors and gap in the BEW (r_{BEW}=58 mm)

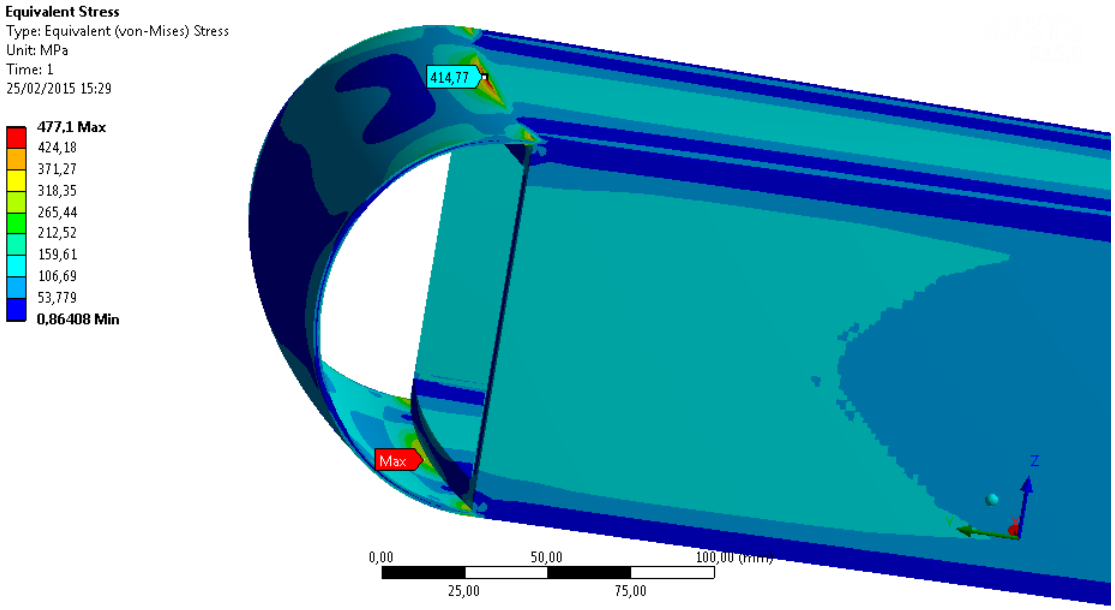

Figure 2.37: Equivalent stress in the shroud with 36 target sectors with gap in the BEW (r_{BEW}=58 mm)

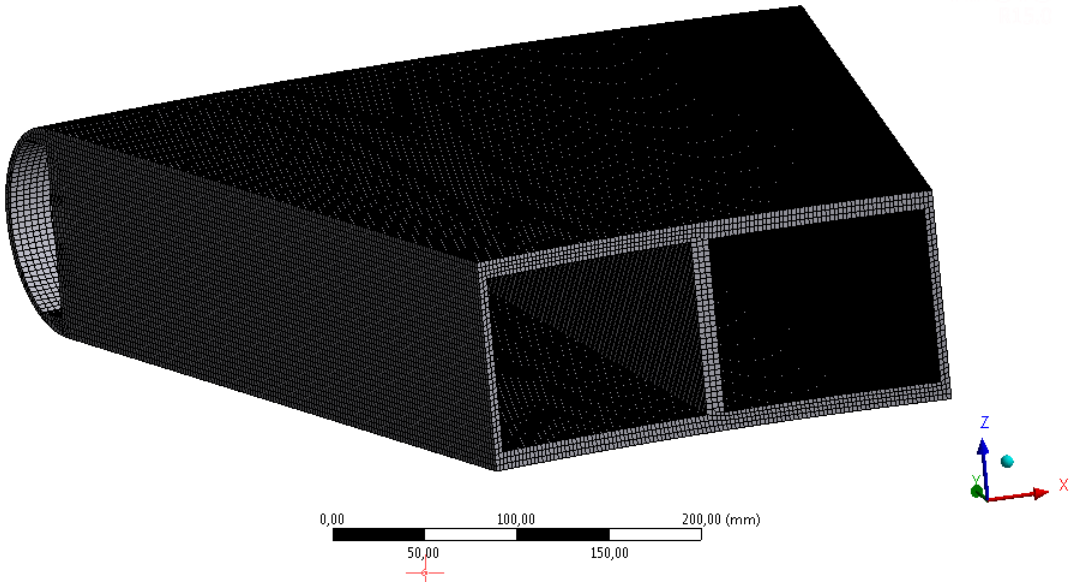

Figure 2.38: Mesh of the shroud with 36 sectors and gap in the BEW (r_{BEW}=58 mm) with stiffeners and rib sharing

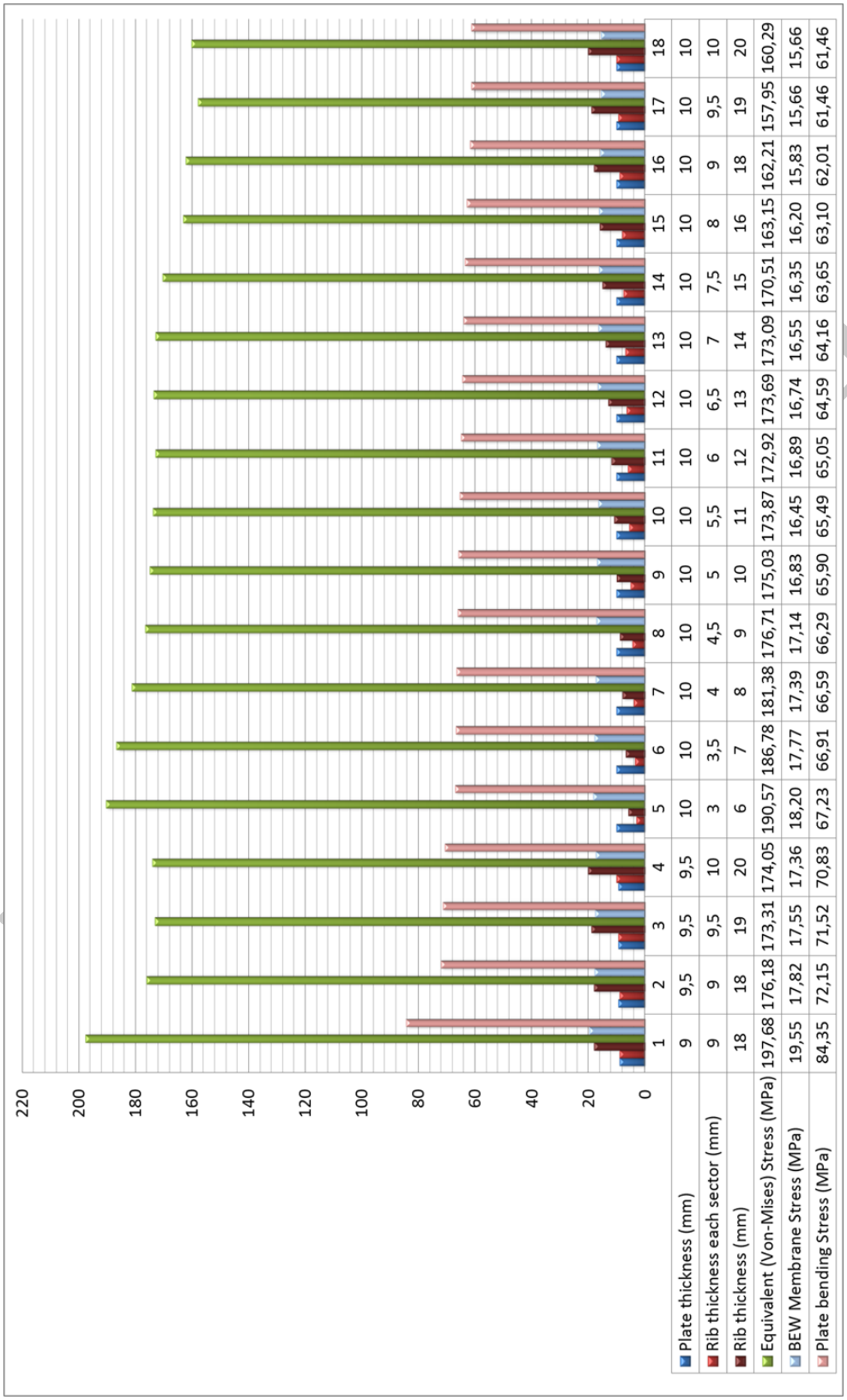

	1	2	3	4	5	6	7	8	9	10	11	12	13	14	15	16	17	18
Plate thickness (mm)	9	9,5	9,5	9,5	10	10	10	10	10	10	10	10	10	10	10	10	10	10
Rib thickness each sector (mm)	9	9	9,5	10	3	3,5	4	4,5	5	5,5	6	6,5	7	7,5	8	9	9,5	10
Rib thickness (mm)	18	18	19	20	6	7	8	9	10	11	12	13	14	15	16	18	19	20
Equivalent (Von-Mises) Stress (MPa)	197,68	176,18	173,31	174,05	190,57	186,78	181,38	176,71	175,03	173,87	172,92	173,69	173,09	170,51	163,15	162,21	157,95	160,29
BEW Membrane Stress (MPa)	19,55	17,82	17,55	17,36	18,20	17,77	17,39	17,14	16,83	16,45	16,89	16,74	16,55	16,35	16,20	15,83	15,66	15,66
Plate bending Stress (MPa)	84,35	72,15	71,52	70,83	67,23	66,91	66,59	66,29	65,90	65,49	65,05	64,59	64,16	63,65	63,10	62,01	61,46	61,46

Figure 2.39: Global results with 36 target sectors with Gap in the BEW (r_{BEW}=58 mm) and rib sharing

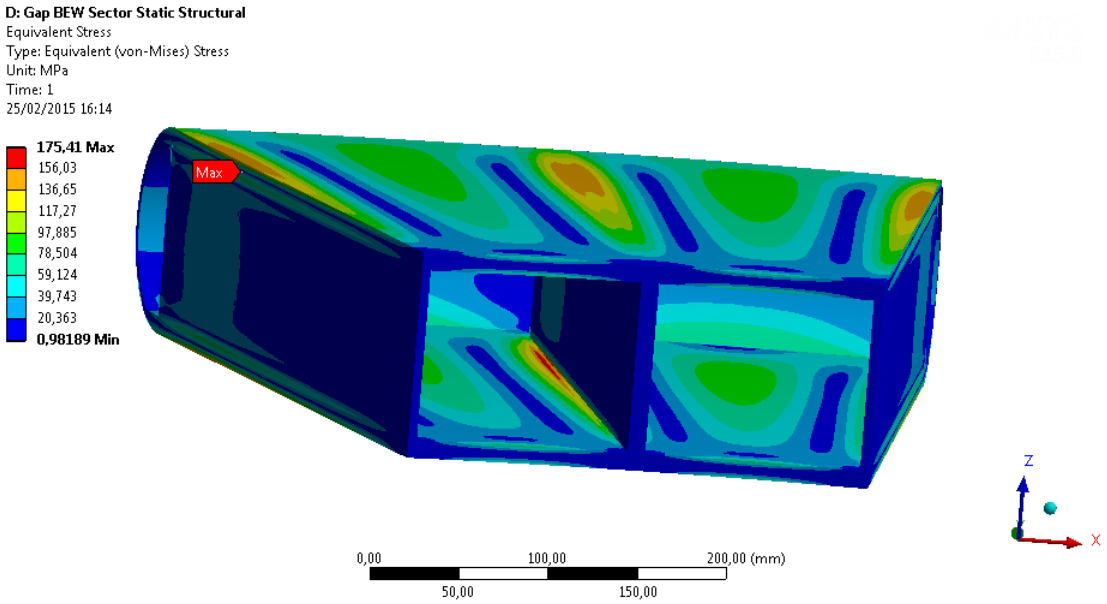

Figure 2.40: Equivalent stress in the shroud with 36 target sectors with gap in the BEW (r_{BEW}=58 mm)

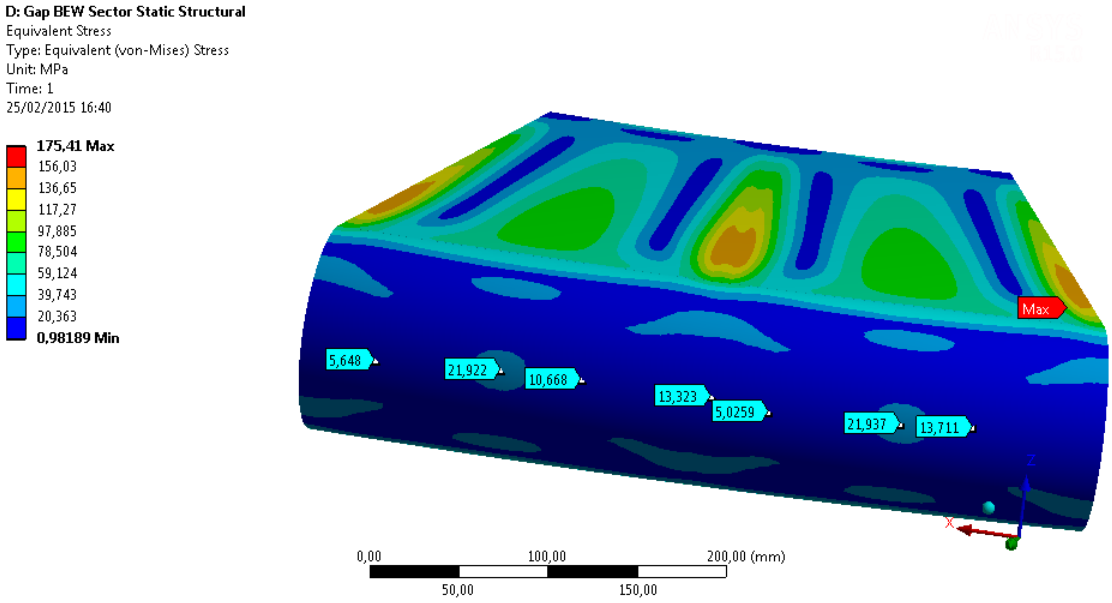

Figure 2.41: Equivalent stress in the shroud with 36 target sectors with gap in the BEW (r_{BEW}=58 mm)

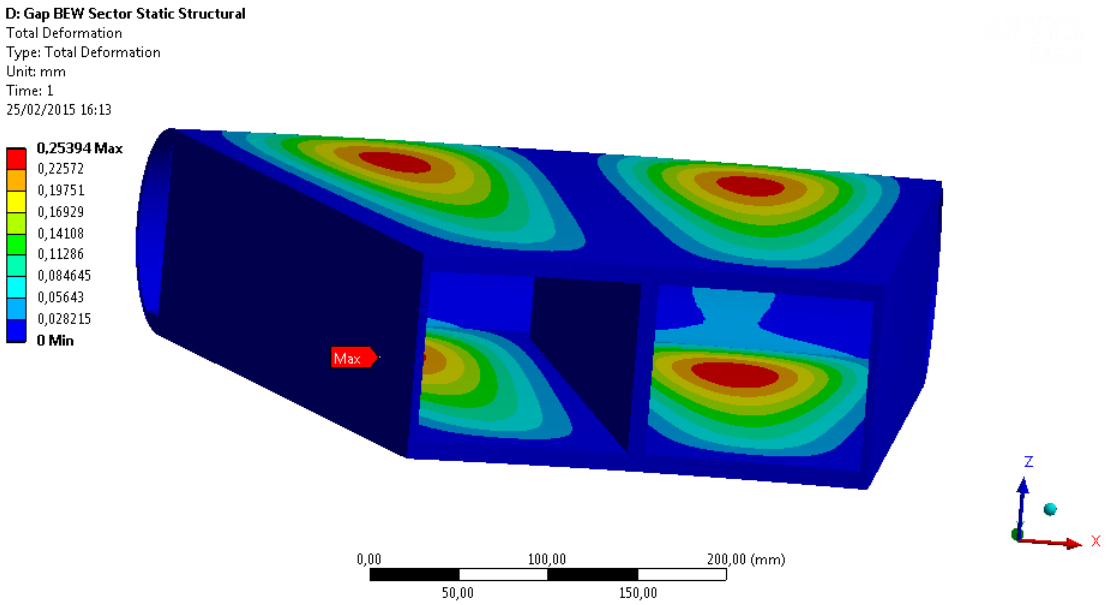

Figure 2.42: Equivalent stress in the shroud with 36 target sectors with gap in the BEW (r_{BEW}=58 mm)

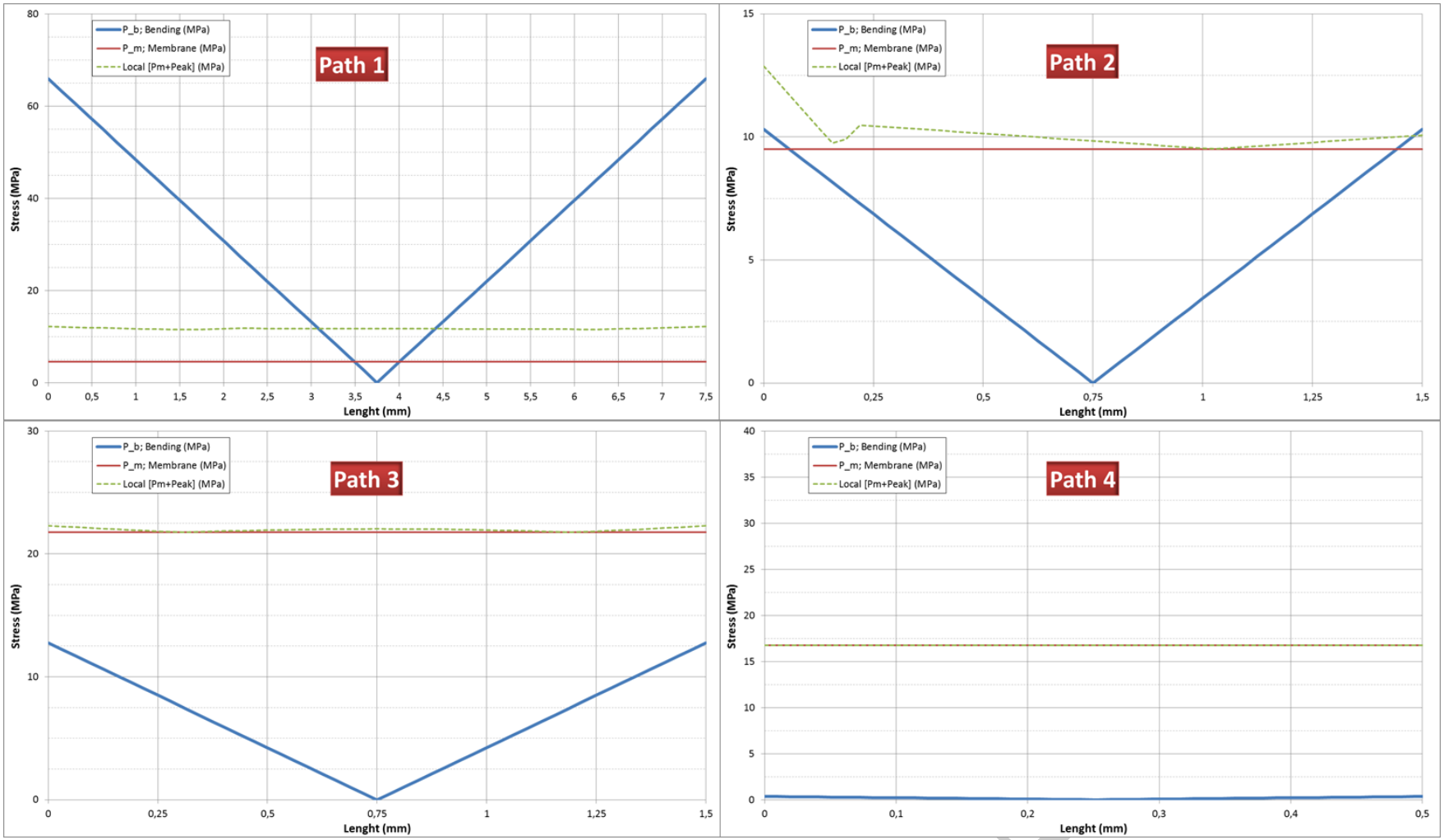

Figure 2.43: Results of the path analysis with 36 target sectors with gap in the BEW (r_{BEW}=58 mm) and rib sharing. Case 9

2.1.6 Shroud with 32 target sectors

This section is divided in:

- Complete sector
- Sector with gap in the BEW, r_{BEW}=72 mm
- Sector with gap in the BEW, r_{BEW}=58 mm and rib sharing

Complete sector

For this study, is has modified the angle of the sector up to 11.25°and the radius value of the BEW is 72 mm, Figures 2.3 and 2.4. The hexa mesh density in this case can be taken from Figure 2.44. The structure consists of total 131,959 elements and 586,666 nodes. Global results of the parametric analysis (12 cases) are shown in the Figure 2.45. Only two cases are below the maximum value (184.5 MPa).

The optimized case for this study is the **case 12** (plate and rib thickness = 10 mm) with an Equivalent Von-Mises Stress value close to 184 MPa, see Figure 2.46 and a total deformation in the top of the plate is less than 0.60 mm, see Figure 2.47.

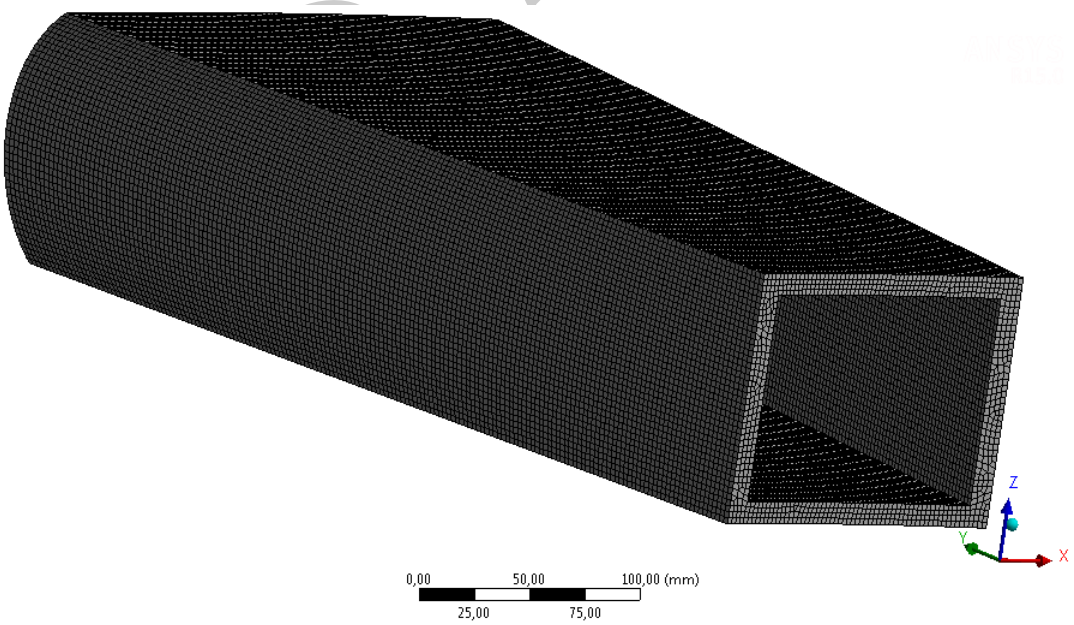

Figure 2.44: Mesh of the shroud with 32 (r_{BEW}=72 mm). Complete sector

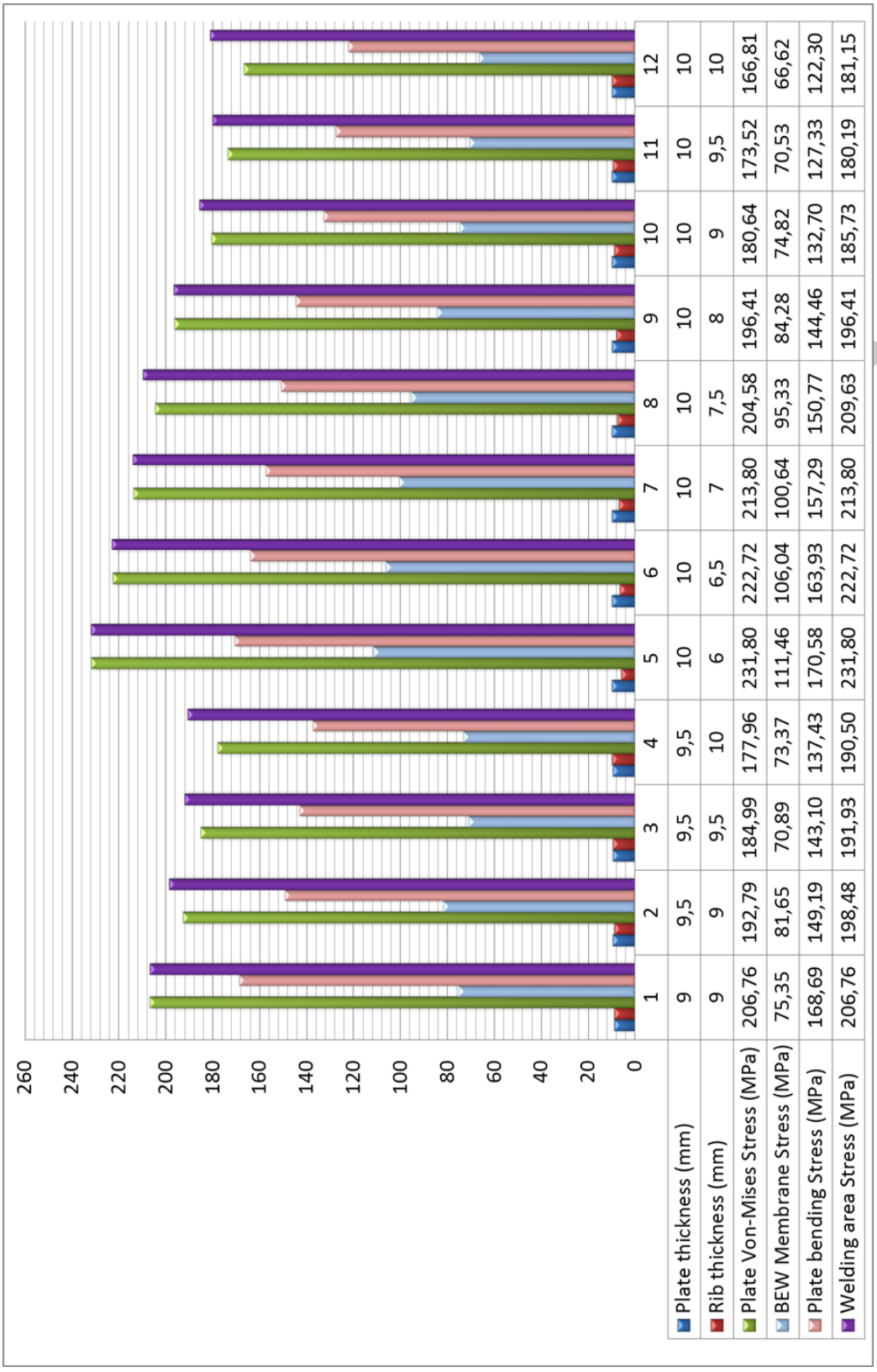

	1	2	3	4	5	6	7	8	9	10	11	12
Plate thickness (mm)	9	9,5	9,5	9,5	10	10	10	10	10	10	10	10
Rib thickness (mm)	9	9	9,5	10	6	6,5	7	7,5	8	9	9,5	10
Plate Von-Mises Stress (MPa)	206,76	192,79	184,99	177,96	231,80	222,72	213,80	204,58	196,41	180,64	173,52	166,81
BEW Membrane Stress (MPa)	75,35	81,65	70,89	73,37	111,46	106,04	100,64	95,33	84,28	74,82	70,53	66,62
Plate bending Stress (MPa)	168,69	149,19	143,10	137,43	170,58	163,93	157,29	150,77	144,46	132,70	127,33	122,30
Welding area Stress (MPa)	206,76	198,48	191,93	190,50	231,80	222,72	213,80	209,63	196,41	185,73	180,19	181,15

Figure 2.45: Global results with 32 target sectors (r_{BEW}=72 mm)

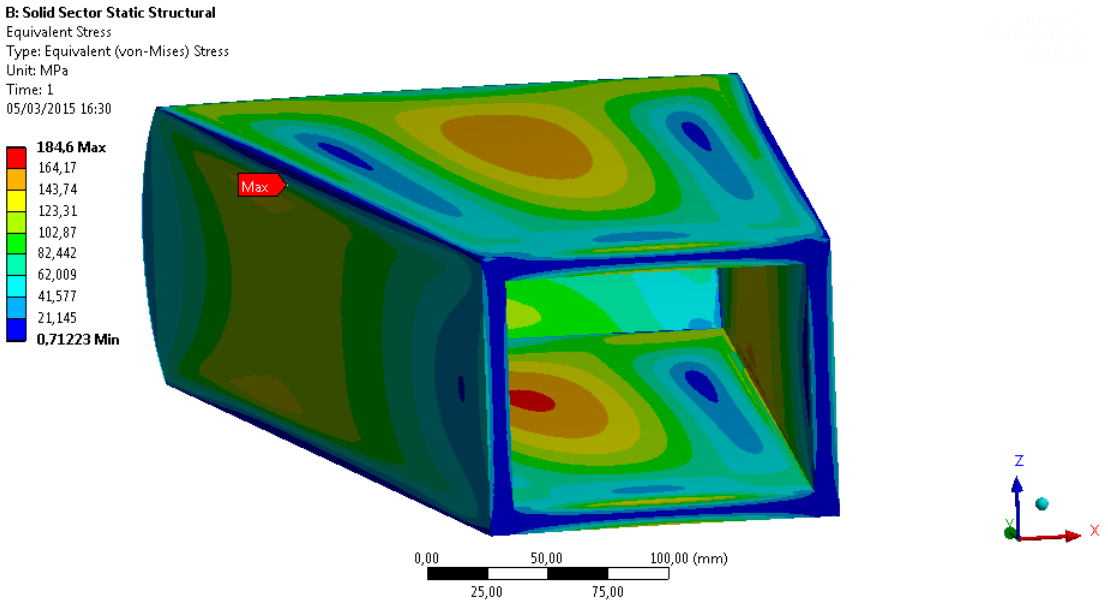

Figure 2.46: Equivalent stress in the shroud with 32 target sectors (r_{BEW}=72 mm)

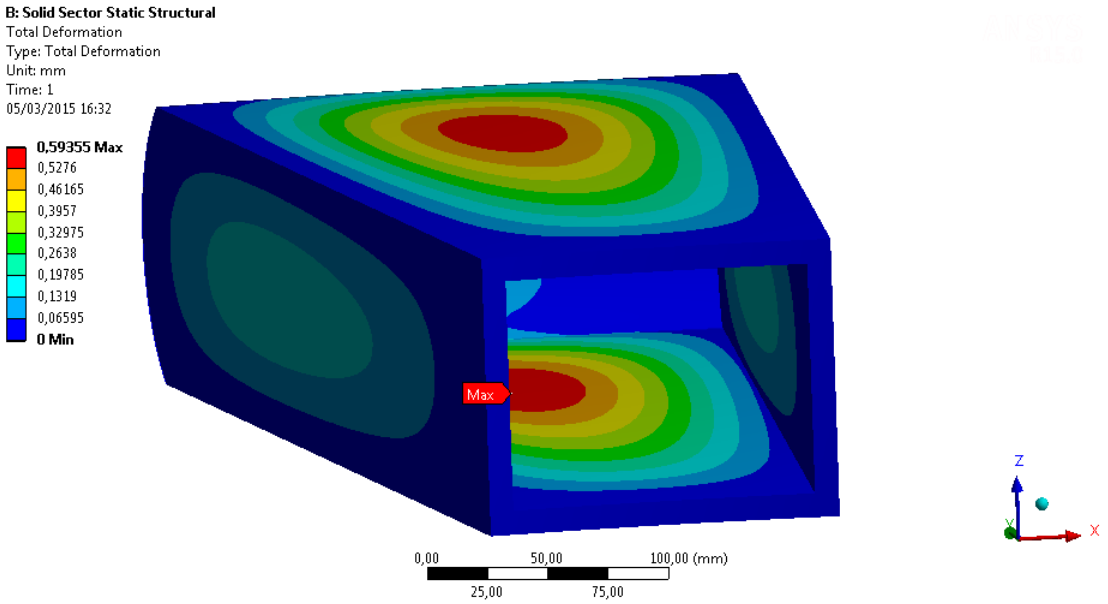

Figure 2.47: Total deformation in the shroud with 32 target sectors (r_{BEW}=72 mm)

Sector with gap in the BEW, r_{BEW}=72 mm

This configuration is the same as section 2.1.6, but including the gap in the BEW, see Figures 2.5 and 2.6. Mesh density in this case can be seen in Figure 2.48. It consists of a total of 130,471 elements and 608,744 nodes. results are shown in the Figure 2.49. There are not any case that have the acceptable Von-Mises stress value. The better case (but exceeding the RCC-MRxMx boundary) for this study is the **case 12** (plate and rib thickness = 10 mm) with an Equivalent Von-Mises Stress value of 206.87 MPa in the welding area, see Figure 2.50 and a total deformation in the top of the plate is less than 0.31 mm, see Figure 2.51.

This case is unfeasible due to exceeds RCC-MRxMx criteria.

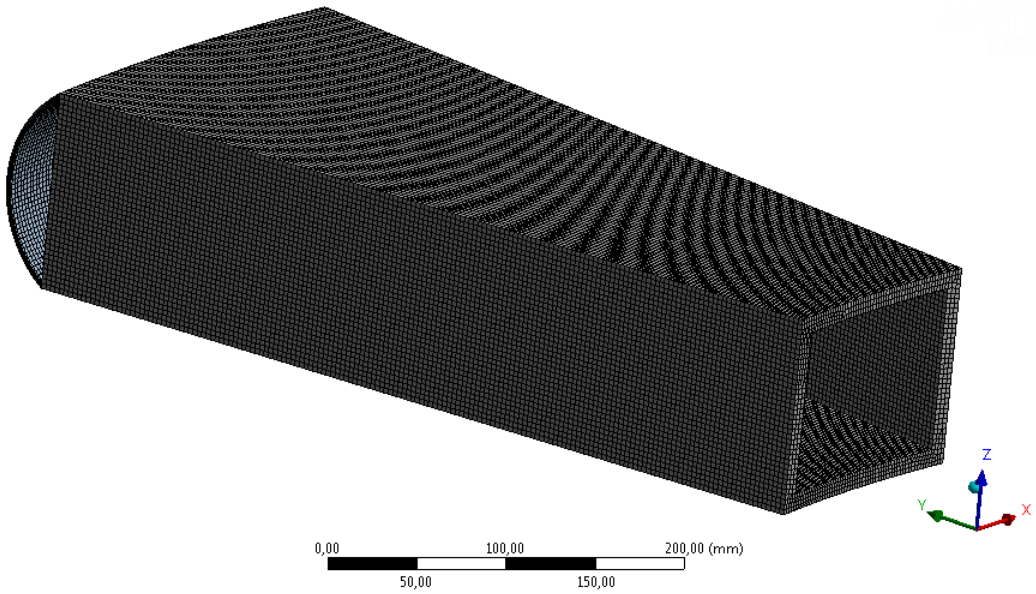

Figure 2.48: Mesh of the shroud with 32 sectors and gap in the BEW (r_{BEW}=72 mm)

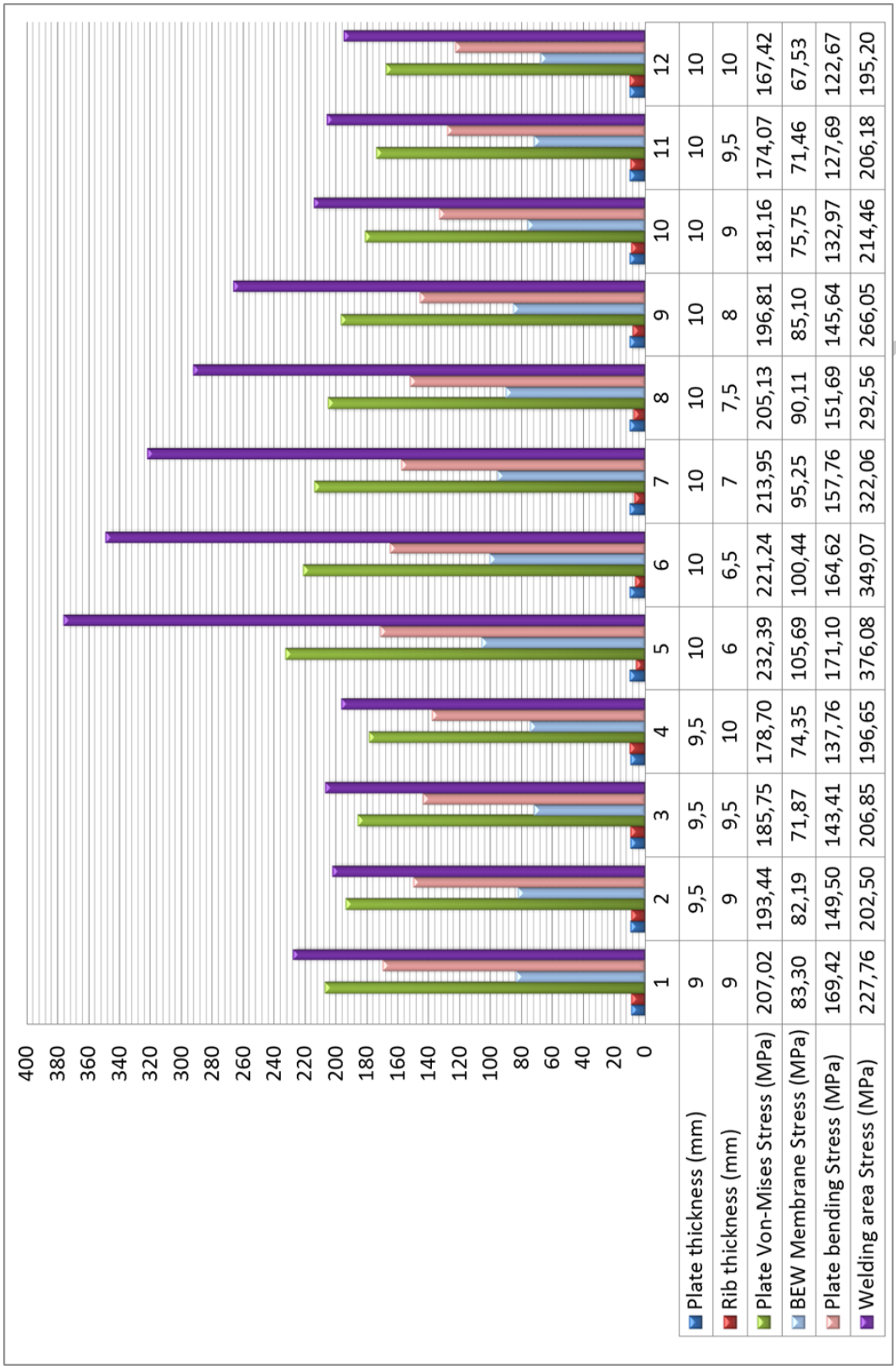

	1	2	3	4	5	6	7	8	9	10	11	12
Plate thickness (mm)	9	9,5	9,5	9,5	10	10	10	10	10	10	10	10
Rib thickness (mm)	9	9	9,5	10	6	6,5	7	7,5	8	9	9,5	10
Plate Von-Mises Stress (MPa)	207,02	193,44	185,75	178,70	232,39	221,24	213,95	205,13	196,81	181,16	174,07	167,42
BEW Membrane Stress (MPa)	83,30	82,19	71,87	74,35	105,69	100,44	95,25	90,11	85,10	75,75	71,46	67,53
Plate bending Stress (MPa)	169,42	149,50	143,41	137,76	171,10	164,62	157,76	151,69	145,64	132,97	127,69	122,67
Welding area Stress (MPa)	227,76	202,50	206,85	196,65	376,08	349,07	322,06	292,56	266,05	214,46	206,18	195,20

Figure 2.49: Global results with 32 target sectors with Gap in the BEW (r_{BEW}=72 mm)

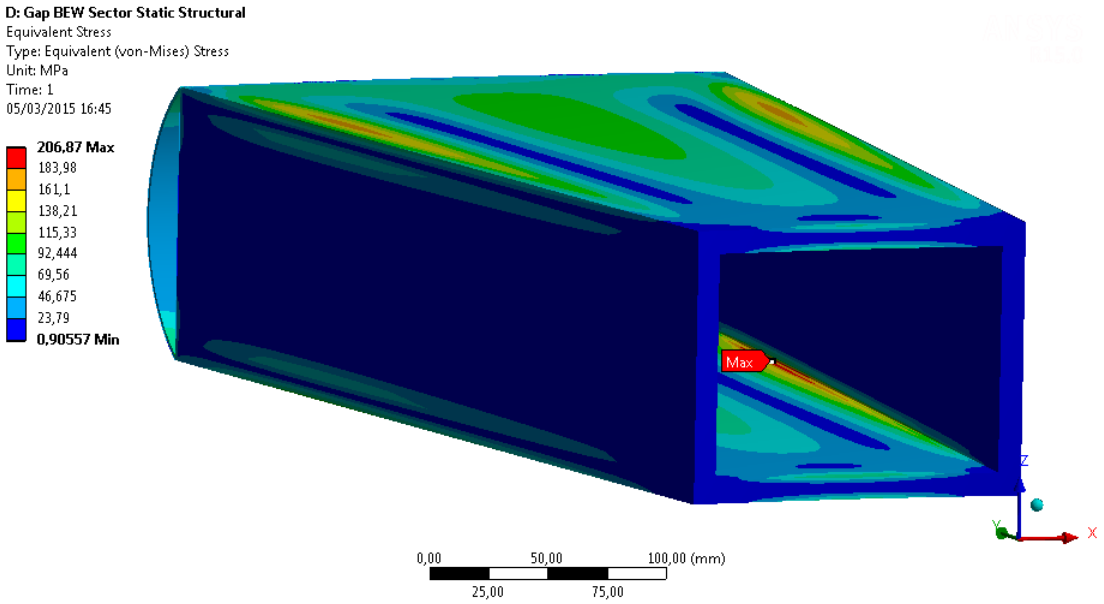

Figure 2.50: Equivalent stress in the shroud with 32 target sectors with gap in the BEW (r_{BEW}=72 mm)

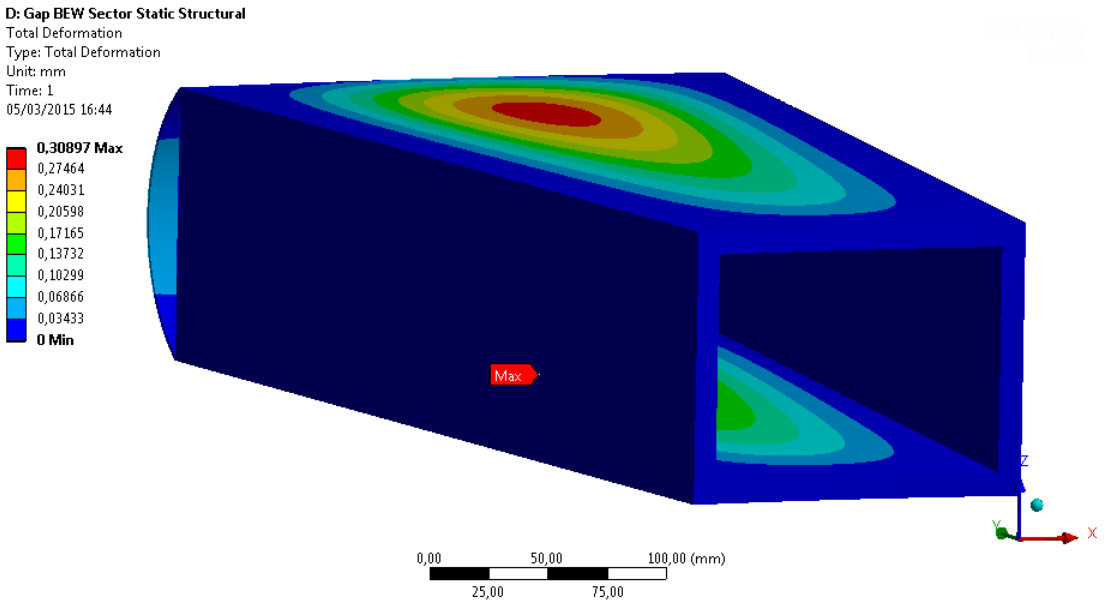

Figure 2.51: Total deformation in the shroud with 32 target sectors with gap in the BEW (r_{BEW}=72 mm)

Sector with gap in the BEW, r_{BEW}=58 mm and rib sharing

This case is the same as 2.1.6 but modifying the radius up to 58 mm, and the rib is shared between two sectors, see Figures 2.9 and 2.10. Mesh density is 119,670 elements and 574,012 nodes (see Figure 2.52). Global results (11 cases) are shown in the Figure 2.53. In the same way as 2.1.6 there are not any case that satisfy the RCC-MRxMx criteria. The better case for this study (but exceeding the RCC-MRxM boundary, Table 2.1.2) is the **case 11** (plate thickness = 10 and rib thickness [each sector] = 10 mm) with an Equivalent Von-Mises Stress value close to 200 MPa in the welding area, see Figure 2.50 and a total deformation in the top of the plate less than 0.35 mm, see Figure 2.51.

This case, same as section 2.1.6 is unfeasible due to exceeds RCC-MRxMx criteria.

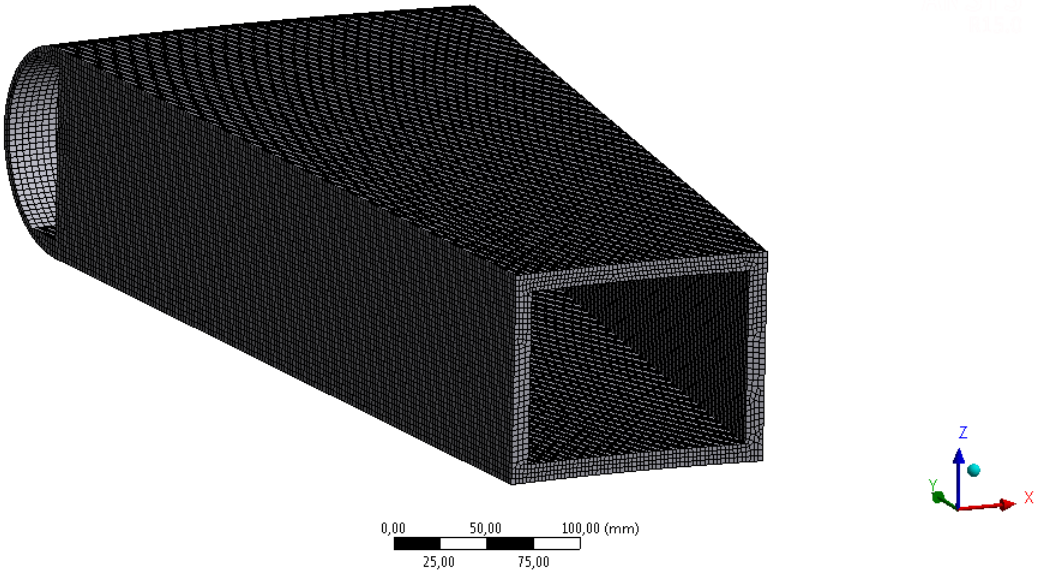

Figure 2.52: Mesh of the shroud with 32 sectors and gap in the BEW (r_{BEW}=58 mm) and rib sharing

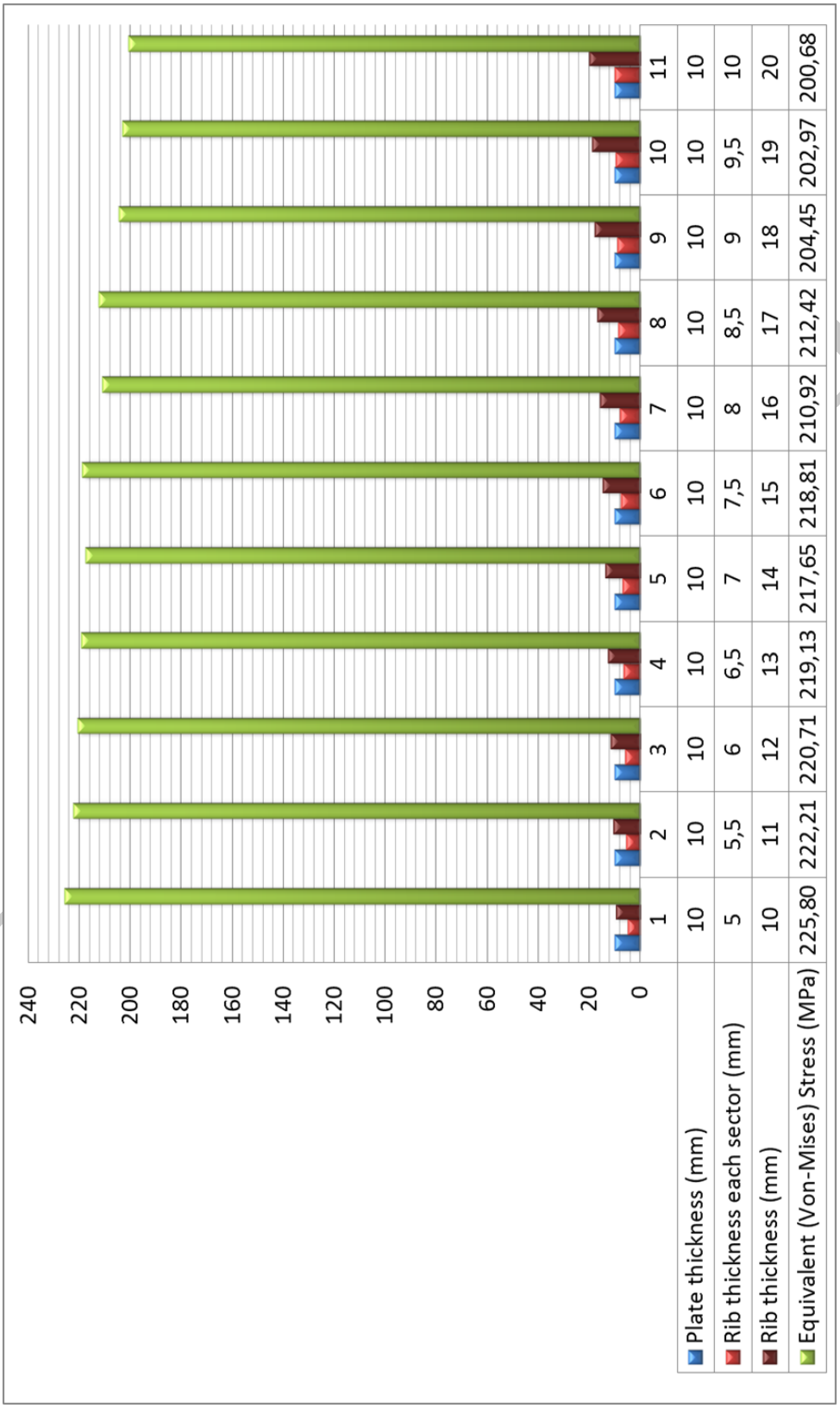

Figure 2.53: Global results with 32 target sectors with Gap in the BEW (r_{BEW}=58 mm) and rib sharing

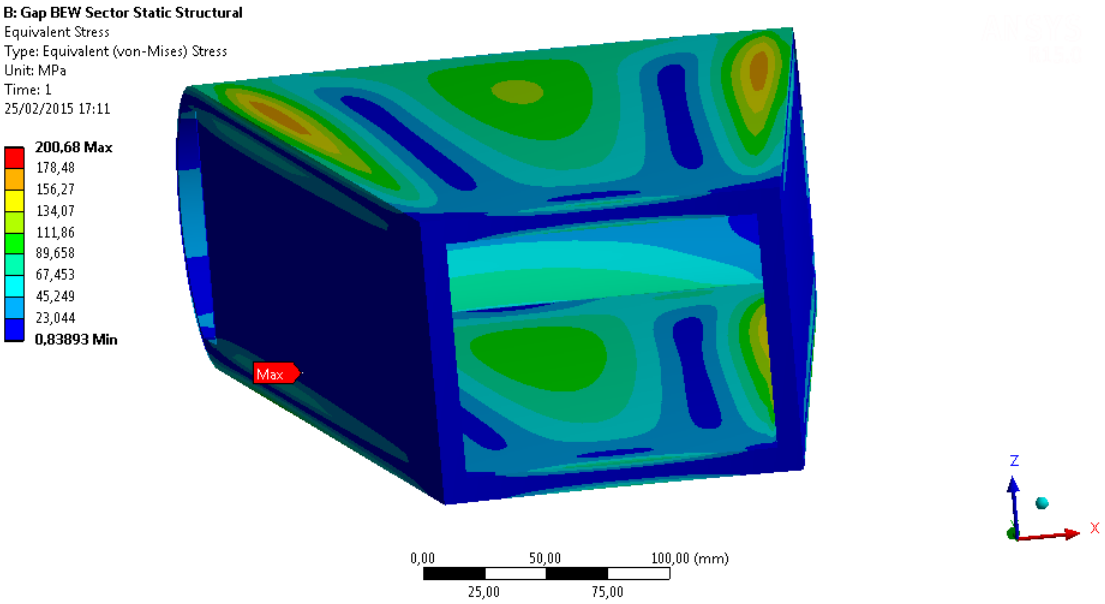

Figure 2.54: Equivalent Von-Mises stress with 32 target sectors with Gap in the BEW (r_{BEW}=58 mm) and rib sharing

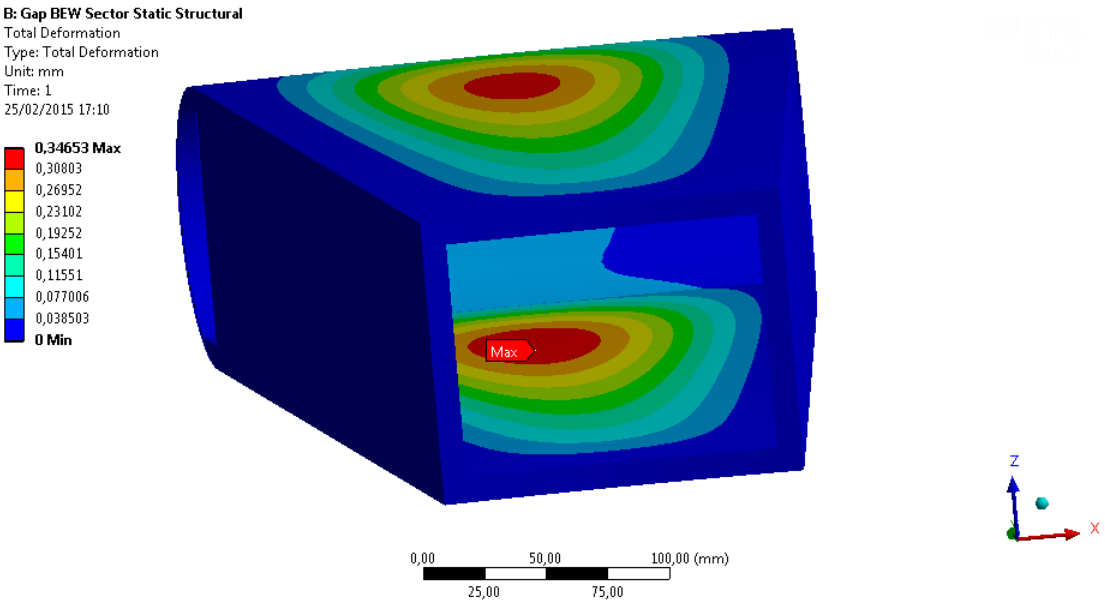

Figure 2.55: Total deformation with 32 target sectors with Gap in the BEW (r_{BEW}=58 mm) and rib sharing

2.1.7 Shroud without stiffeners

As it can be seen in Figures 2.58 and 2.59, this configuration is not feasible due to the high deformation (24,75 mm) and the Von-Misses stresses (2532,4 MPa) reached in the shroud. For this reason, ribs are essential in the structure, to provide stiffness. It has been assessed several types of meshes. The mesh density can be taken from Figure 2.56, and with more detail in figure 2.57. It consists of a total of 72,057 elements and 366,708 nodes and solved considering cyclic symmetry.

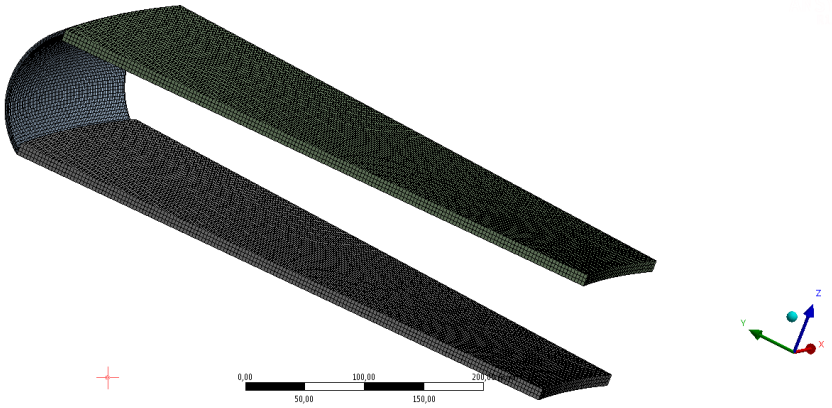

Figure 2.56: Mesh of the shroud without stiffeners (r_{BEW}=72 mm)

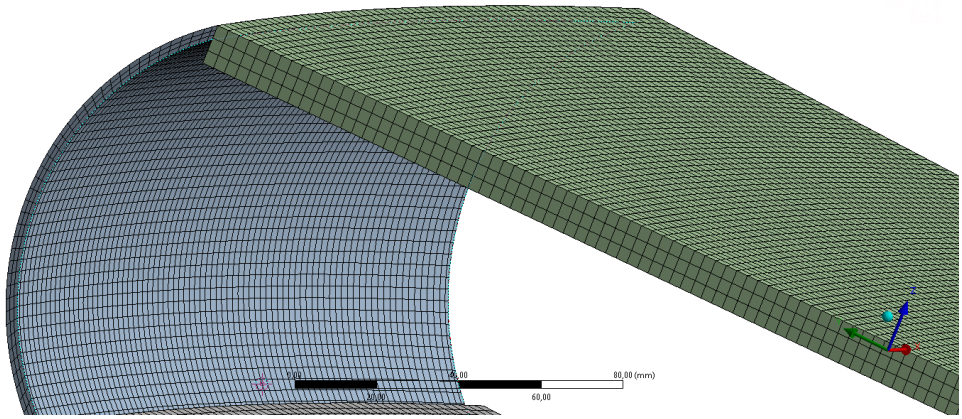

Figure 2.57: Detail mesh of the shroud without stiffeners (r_{BEW}=72 mm)

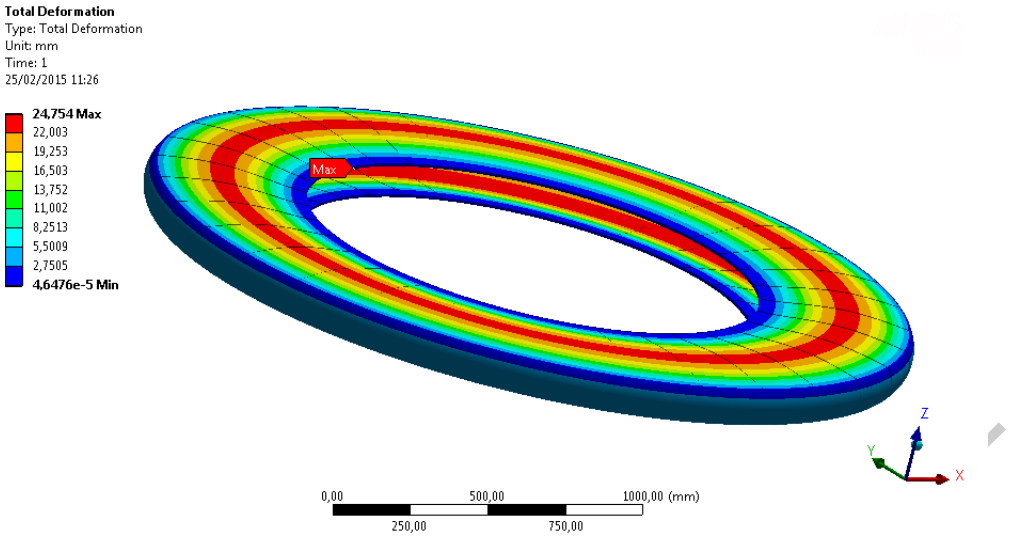

Figure 2.58: Total deformation in the shroud without stiffeners (r_{BEW}=72 mm)

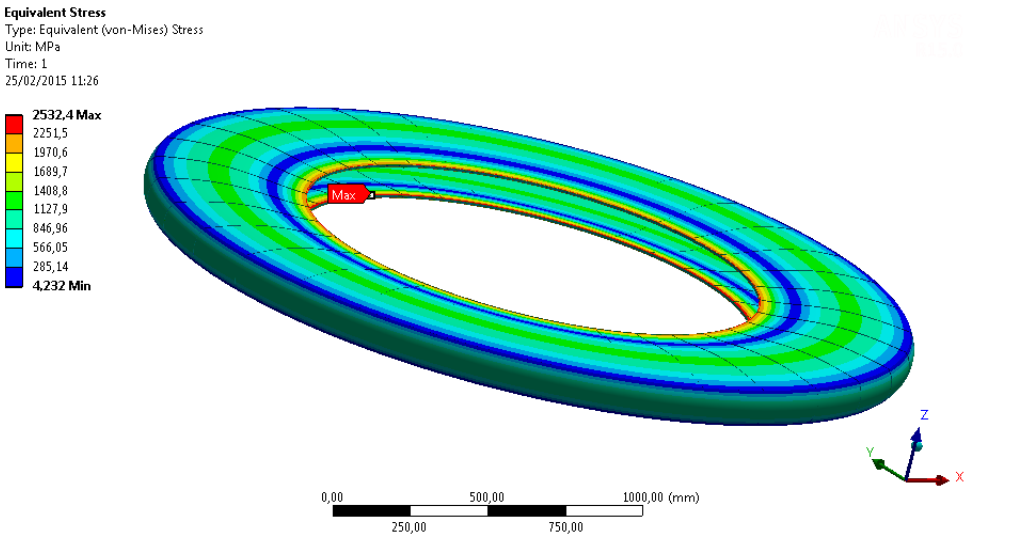

Figure 2.59: Equivalent stress in the shroud without stiffeners (r_{BEW}=72 mm)

2.1.8 Conclusions

- **33 target sectors:** the target vessel has a good mechanical behavior with this configuration, but it is complicated to manufacturing because of the periodic angle.
- **32 target sectors:** holds high Von-Mises stresses. Structural geometrical conditions are demanding, rib thickness is around 20 mm.
- **36 target sectors:** good structural and manufacturing option. Stresses are reduced because the efforts are more distributed on more ribs.
- The radius change (from 78 mm to 58 mm) in the BEW produces an improvement in the He distribution.
- The incorporation of the gap is considered a safety measure in case of a block in the inlets of one sector.
- BEW stiffeners improves the stress conditions in the structure.
- Ribs are essential component in the vessel. Without ribs the structure is absolutely unfeasible.

2.2 Target Vessel

2.2.1 Introduction

Due to simplify the preliminary mechanical design the Target Wheel has been divided in two different parts, one part is the Shroud which contains the blocks of tungsten and leads the helium to refrigerate the spallation material, studied in the previous section. The other part is the Target Vessel which physically supports the Shroud and delivers the helium from the axis of the Target wheel.

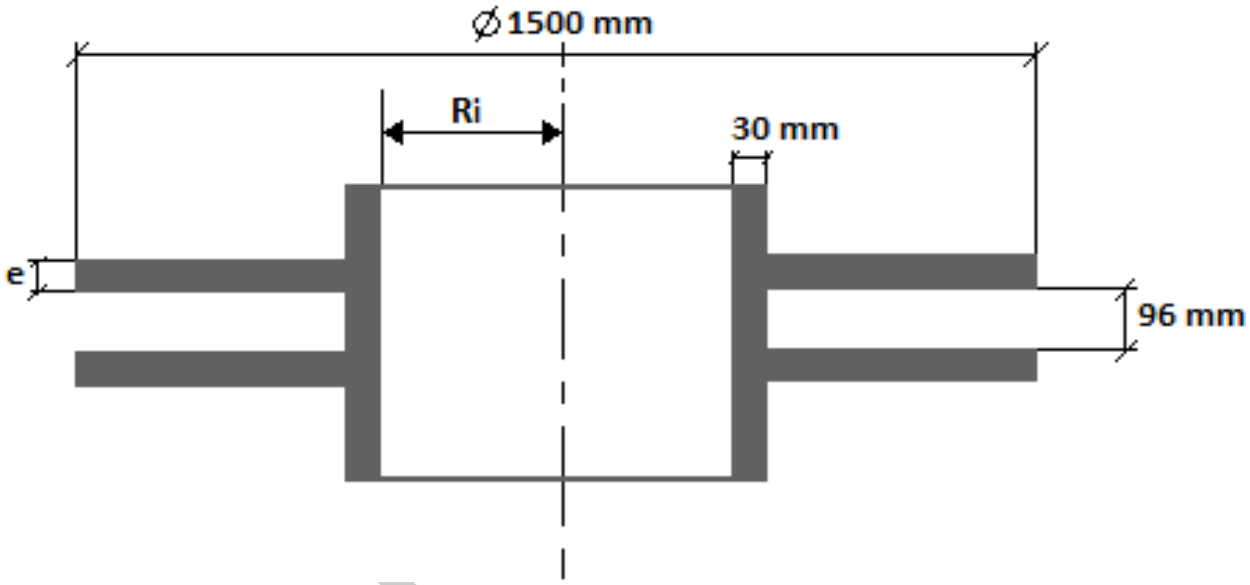

Figure 2.60: Target Vessel sketch

The mechanical design begins from a Target Wheel concept that has been parametrized in CAD, required loads and boundary conditions have been applied in a FE Model and different results have been obtained adjusting geometrical parameters. The design concept (Figure2.60) consists of two parallel circular ring plates with a thickness **e** (parameter), separated a distance **s**=96 mm and an outer radius $\mathbf{R}_e$=750 mm (both required by the Shroud geometry). The rings are welded to a vertical cylinder with a thickness **t**=30 mm and inner radius $\mathbf{R}_i$ (parameter). The axis of the cylinder is coincident with the rotation axis of the whole system.

The Target Vessel is fully made of steel SS316, the mechanical properties used for the FEM are listed below:

- Density= 7800 kg/m^3
- Young's Modulus= 216 GPa

- Poisson's ratio= 0.265

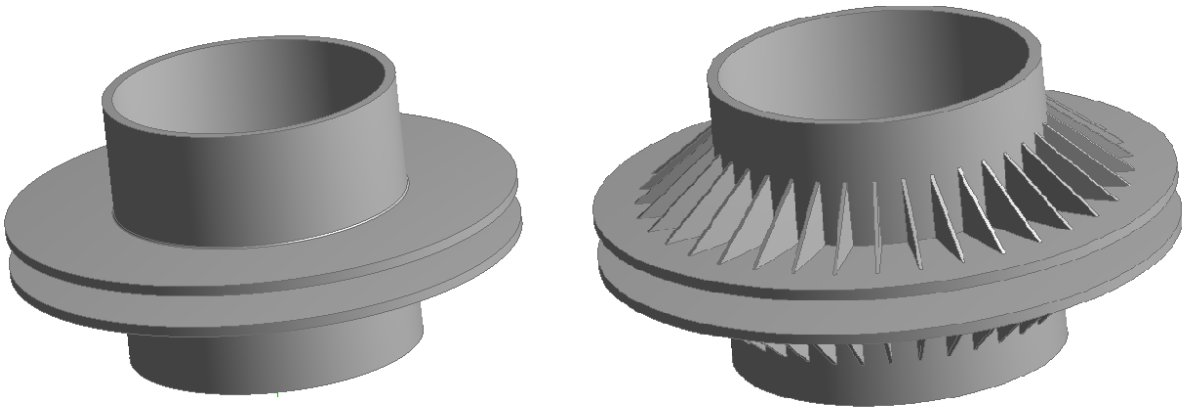

Figure 2.61: Target Vessel with and without ribs

In some FEM simulations a geometry with stiffening ribs (Figure2.61 right) has been studied in order to analyze and compare the mechanical response of the Target Vessel with and without the ribs. Based on previous studies and FEM simulations the geometry has been set as follows:

- Rib thickness = 10 mm
- Angle between the rib ant the horizontal plane = 40^{o}
- Rib lenght = $2/3 \cdot (\mathbf{R}_e\text{-}\mathbf{R}_i\text{-}\mathbf{t})$

2.2.2 Load and boundary conditions

For an accurate mechanical response FEM simulation, the applied loads and boundary conditions to the Target Vessel are the following:

- Gravity
- Tungsten and Shroud weight, which is simulated with a remote force applied on the perimeter of the ring plates
- Design helium pressure (12 bar)
- Fixed support on top of the cylinder
- 0,1 mm of displacement in the rotation axis direction, which is applied on the perimeter of the ring plates

In the following sections the results of the analysis are shown.

2.2.3 Stiffening ribs

In order to study the influence of the stiffening ribs on the mechanical behavior of the Pressure Vessel various FEM simulations were performed (for both settings with and without ribs) by varying the inner cylinder radius ($\mathbf{R}_i$) and the ring plates thickness ($\mathbf{e}$). Except in the simulations performed in the section 2.2.3, where the number of the stiffening ribs is studied, a Target Vessel configuration of 36 equally spaced stiffening ribs in each plate has been employed. To simplify the mechanical analysis, the cylinder holes through which the helium flows have been suppressed in the simulations discussed in this section, the influence of drilling the Target Vessel cylinder axis will be studied in the section 2.2.4 .

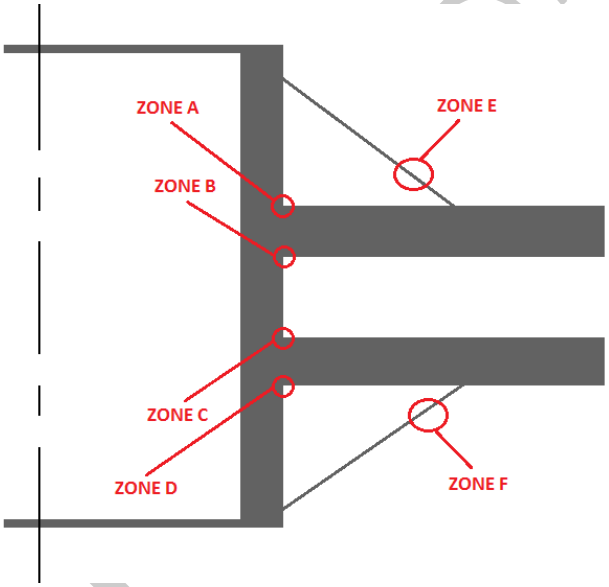

Figure 2.62: Target Vessel with and without ribs

Tables 2.2 (configuration without ribs) and 2.3 (configuration with ribs) show for each pair of parameters $\mathbf{R}_i$ and $\mathbf{e}$ some of the mechanical response results, as the maximum total deformation and the equivalent stress in areas where it is relatively high. These zones are identified in figure2.62 and correspond to the edges of the ribs and to the corners formed between the cylinder and the ring plates. Specifically for the configuration without ribs the highest equivalent stress is found around the upper corner formed by the cylinder and the top ring plate (zone A). On the other hand for the configuration with strips the lower ribs are subjected to the highest stress.

All the stress values which exceed the steel SS316 yield strength (σ_e=290 MPa) are not physically realistic but they have been included in the table 2.2 and figure 2.63 for a better study of the parameters influence.

R_i (mm)	e (mm)	Max.Def. (mm)	Max. equivalent stress (Mpa)			
			Zone A	Zone B	Zone C	Zone D
200	20	3.713	1064	1014	1028	1051
300	20	1.621	597	576	576	591
400	20	0.594	320	303	298	304
400	25	0.355	220	201	197	207
400	30	0.243	162	147	138	151
450	30	0.156	121	108	96	106
450	25	0.211	158	143	136	143
450	20	0.333	224	211	204	212

Table 2.2: Target Vessel without stiffening ribs mechanical response

R_i (mm)	e (mm)	Max.Def.(mm)	Max. equivalent stress (Mpa)			
			Zone B	Zone C	Zone E	Zone F
200	20	0.369	141	141	77	69
300	20	0.27	110	101	97	97
400	20	0.184	92	75	98	121
400	25	0.152	84	70	82	102
400	30	0.131	79	65	74	85
450	30	0.11	73	54	73	82
450	25	0.123	77	59	79	91
450	20	0.145	84	65	87	112

Table 2.3: Target Vessel with stiffening ribs mechanical response

Inner cylinder radius (R_i)

In the figure 2.63 the maximum equivalent stress has been represented for different inner cylinder radius of the Target Vessel and for both configurations, with and without ribs. The thickness of the ring plates considered is 20 mm, the rest of the Target Vessel dimensions are the already mentioned.

As the graph in the figure 2.63 displays increasing the inner cylinder radius helps reduce stress, this effect is more significant in the Target Vessel without ribs. In fact if the inner radius is increased, enough stress values closed to which ones obtained in the Target Vessel with stiffener ribs can be reached.

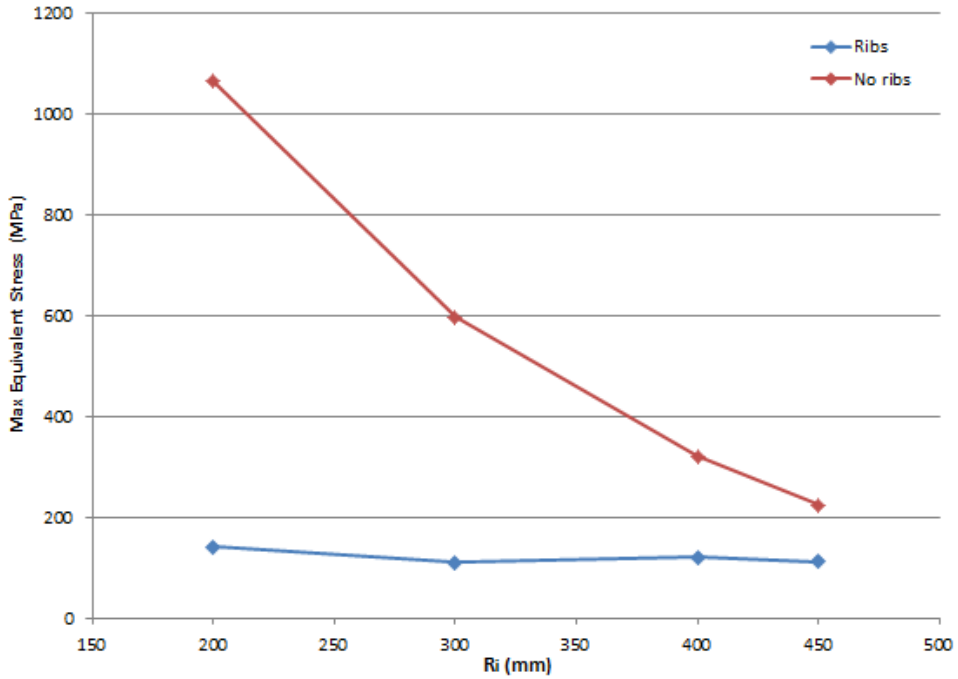

Figure 2.63: Maximum equivalent stress for different $\mathbf{R}_i$ values

Ring plates thickness (e)

In the figure 2.64 the maximum equivalent stress has been represented for different ring plates thickness. The four lines plotted in the graph correspond to four different configurations of the Target Vessel, with and without ribs for an inner cylinder radius of 400 and 450 mm.

As the graph in the figure 2.64 displays increasing the ring plates thickness decreases the mechanical stress in similar way as it was discussed with an increase of the inner cylinder radius. Additionally, as happened with the inner radius, this effect is more significant in the Target Vessel without ribs. In fact if the inner radius is increased, enough stress values closed to which ones obtained in the Target Vessel with stiffener ribs can be reached.

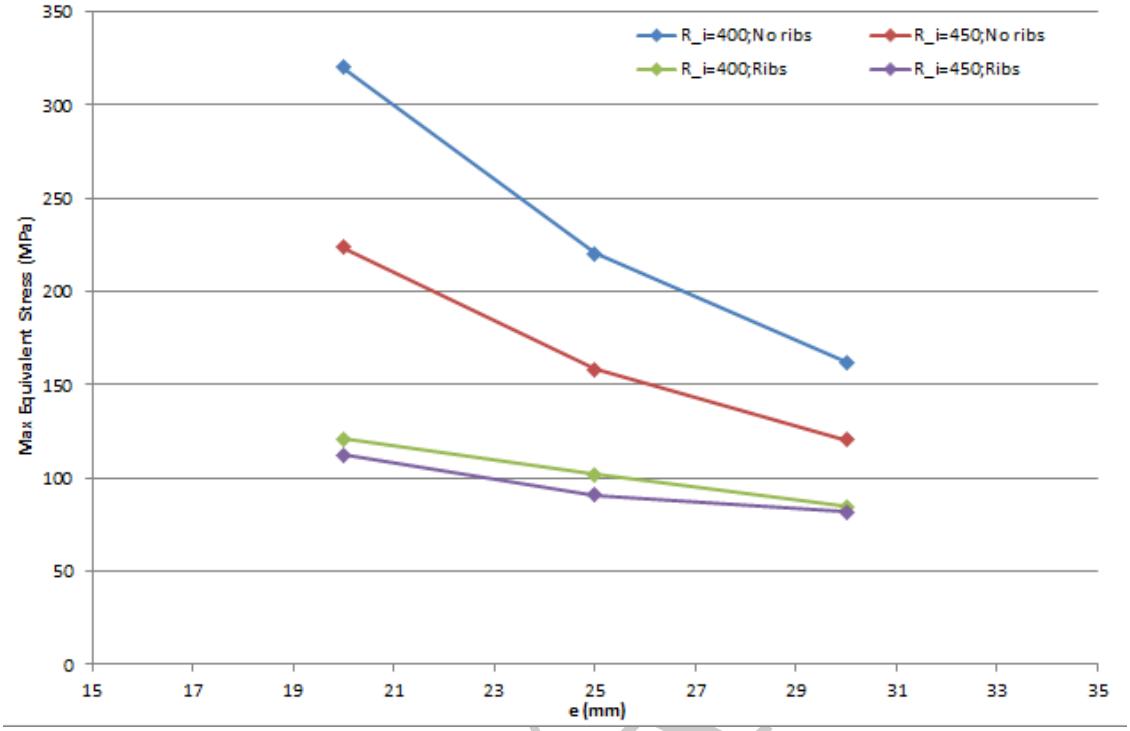

Figure 2.64: Maximum equivalent stress for different **e** values

Ribs number

Table 2.4 shows the mechanical response of the Target Vessel depending on the number of equally spaced stiffening ribs per ring plate. The dimensions of the ribs were described in section 2.2.1. The inner cylinder radius is 200 mm and the ring plates thickness is 20 mm.

The influence of the ribs number (between 32 and 36) is negligible, and the mechanical behavior is practically identical. The maximum equivalent stress and maximum total deformation values are almost the same for all Target Vessel configurations.

Ribs number	Mass (kg)	Max. equivalent Stress (MPa)	Max. def. (mm)
36	1028.1	141	0.369
35	1020.2	141	0.371
34	1012.4	143	0.375
33	1004.5	141	0.378
32	996.6	139	0.382

Table 2.4: Max. stress and deformation for different stiffening ribs number

2.2.4 Cylinder helium holes

The geometry of the holes in the cylinder through which the coolant flows is detailed in figure 2.65, dimensional settings chosen correspond to speed limitations of the helium flux. The hole in the middle correspond to the outlet of the hot helium which has flowed through the Shroud between the tungsten blocks, the other two holes are the inlets of the cold helium which conducts the coolant from the Target Wheel axis to the entrance channels of the Shroud. The oval geometry is because drilling the easiest way to manufacture the helium holes, this geometry also helps decreasing the stress by suppressing the corners.

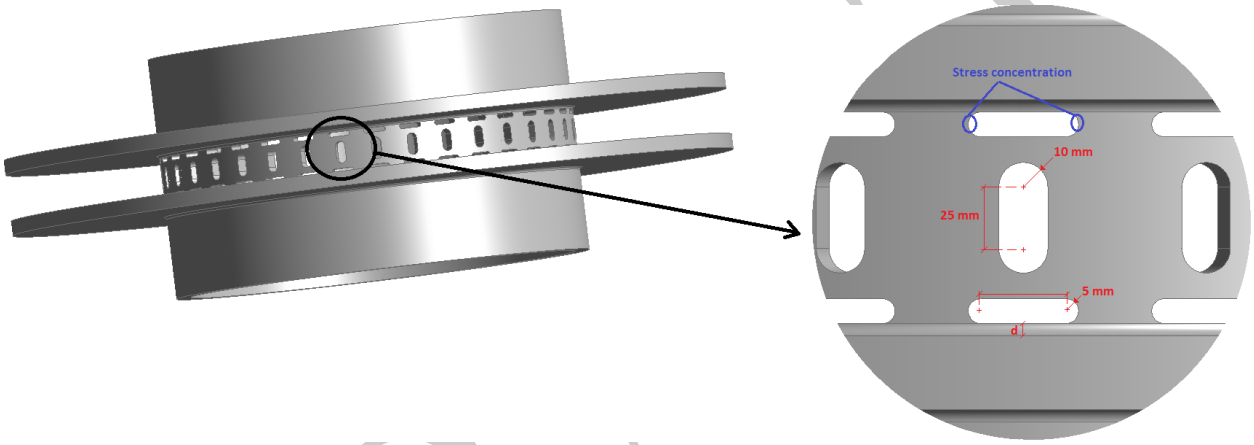

Figure 2.65: Helium holes inlets/outlets geometry

As the FEM simulations show the presence of a discontinuity of material closed to the ring plates such as helium inlet holes causes a stress concentration in this area (see image 2.65) and in this Target Vessel configuration maximum stress zones match this concentration zones. In table 2.5 maximum equivalent stress and total maximum deformation can be found for different separation of the helium holes **d**.

Table 2.5 shows maximum equivalent stress and maximum deformation for different hole separation. The thickness of the ring plates considered is 30 mm, the inner cylinder radius is 400 mm and the rest of the Target Vessel dimensions are the already mentioned

d (mm)	Max. Equivalent stress (MPa)	Max. Def. (mm)
0.1	289	0.258
2	243	0.258
3	222	0.258
4	206	0.258
5	195	0.258
6	192	0.258
7	193	0.258
8	193	0.258
9	192	0.258
10	185	0.258

Table 2.5: Max. stress and deformation for different helium inlet holes distances

The graph plotted in figure 2.66 shows that increasing the hole distance the maximum stress is reduced. From 5 mm of separation the stress decreasing is very low.

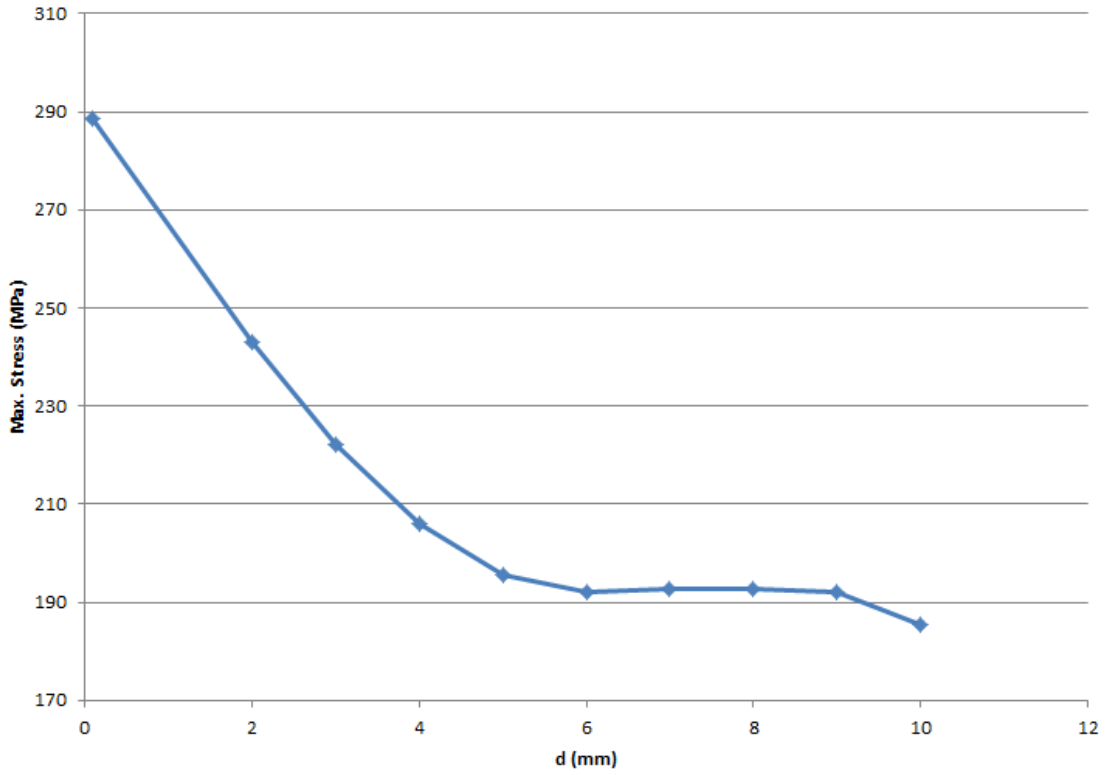

Figure 2.66: Maximum equivalent stress vs helium inlet holes distance to the ring plates

The figure 2.67 shows the mechanical strain and stress maps of the Target Vessel configuration described in the figure 2.65.

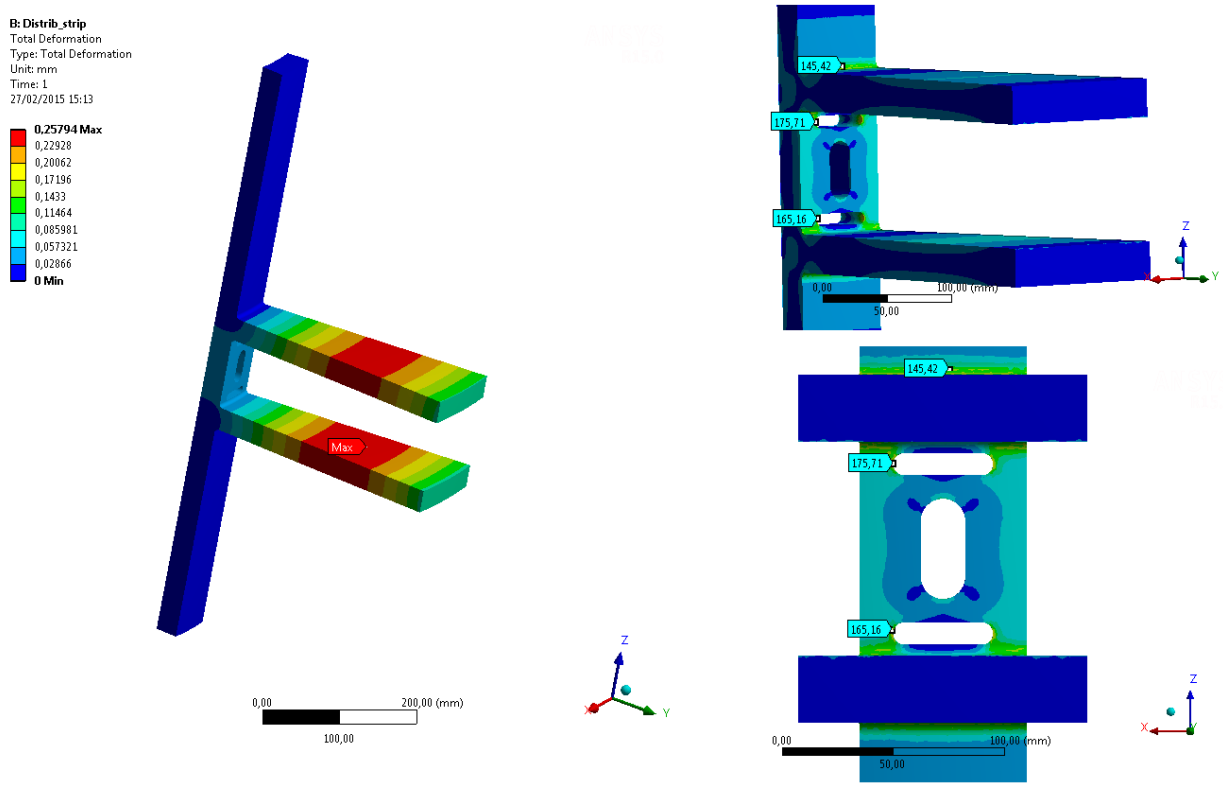

Figure 2.67: Mechanical strain and stress maps

2.2.5 Conclusions

- The value of the inner cylinder radius ($\mathbf{R}_i$) should be as large as possible. Increasing this radius the Vessel becomes more robust and the maximum equivalent stress and deformation decrease. According to the performed FEM simulations a value of $\mathbf{R}_i$ between 400 and 450 mm achieves acceptable conditions from the mechanical point of view.

- The value of the ring plates thickness ($\mathbf{e}$) should be as large as possible, increasing this thickness the Target Vessel becomes more robust and the maximum equivalent stress and deformation decrease. According to the performed FEM simulations a value of $\mathbf{e}$ between 25 and 30 mm achieves acceptable conditions from the mechanical point of view without increasing too much the total weight.

- The presence of stiffener ribs decreases the stress and the deformation of the Target Vessel, however for large enough values of $\mathbf{R}_i$ and $\mathbf{e}$ (detailed in previous paragraphs) it is possible to obtain acceptable conditions from the mechanical point of view using a Target Vessel without ribs. In a Target Vessel configuration with ribs the mechanical behavior is almost identical for a number of ribs between 32 and 36 per ring plate.

- The oval geometry of helium holes contributes to reduce the stress concentration, although it is necessary separate the helium inlet holes not to exceed the stress requirements. With a separation of **d**=5 mm we could achieve acceptable mechanical conditions.
- The proposed configuration reduces significantly the amount of shielding material in the center of the wheel. Its impact in the proton and neutron streaming have to be evaluated.

Chapter 3

Shaft Shielding

3.1 Introduction

The helium inner and outer channels in the shaft provides streaming paths for neutrons along the shielding of the monolith. This streaming paths can produce a very high dose rate in the top of the target monolith if adequate shielding elements are not introduce in the cooling channels. Due to this effect, the internal shielding of the shaft is critical to reduce the dose rates in the top of the monolith vessel. The figure 3.1 shows the target station configuration for the shielding calculations.

The proton beam comes from the accelerator to the target and generates the neutrons. The target station has a monolith for the shielding but some neutron radiation can scape through the shaft. There are three critical parts of the shaft from the radiation point of view.

- The central pipe for the helium return flow, including a helical inset.
- The space between the outer and inner pipe as the helium inlet for target cooling.
- The gap between the shaft and the monolith for mechanical rotation.

The figure 3.2 represents the shaft more detailed. The cooling pipe is placed at 30 cm of radius since the shaft center and the gap between the shaft and the monolith is placed at 35.5 cm. The neutrons go through these zones from the target to outside and produce out range radiation values.

The mentioned streaming paths for neutrones in the shaft increase the neutron dose rate on top of the target vessel. This radiation field will damage bearings, drive unit and positioning unit so it is critical to minimize this value in order to allow the use of non nuclear credited components.

The analysis of the shaft is a complicated shielding problem for montecarlo analysis so, in order to reduce the stadistical errors several the variance reduction techniques, such as the weight windows generation (WW), are used. The MCNPX weight window generator (WWG)

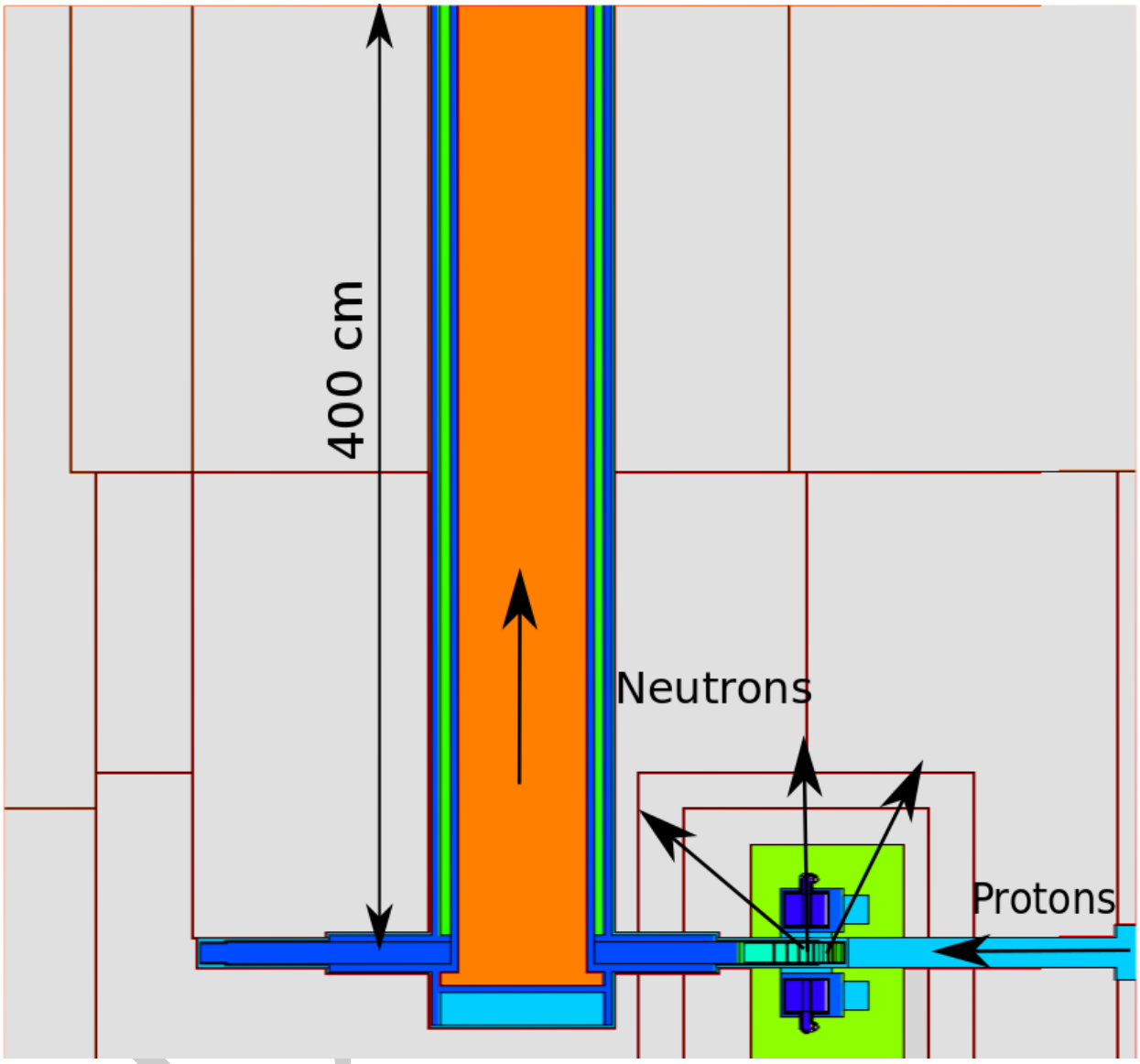

Figure 3.1: Target station configuration for the shielding calculations

has some limitations and, for that reason, a weight window generation tool has been created. The Weight Window Generation Tool has been used for these shielding calculations. It has reduced the computational time considerably and it has provided good statistical error.

3.2 Initial situation and first modifications

The shielding calculations have been done with the MCNPX model considering a beam averaged current set at 2.5 mA. This model has the central pipe of the shaft filled with helium.

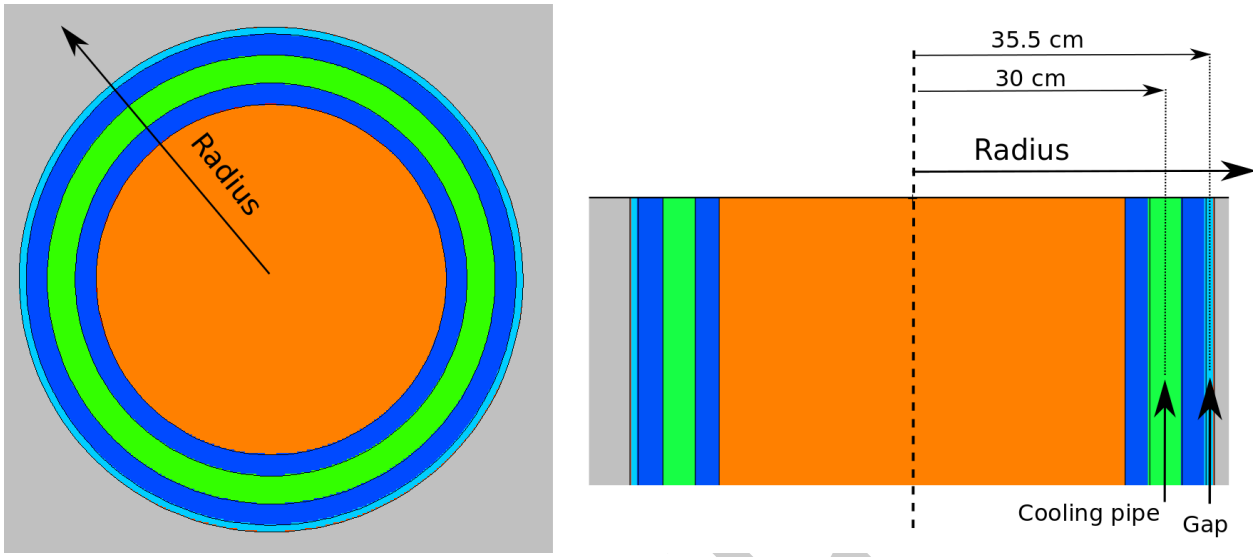

Figure 3.2: Shaft end geometry

In order to simulate the helical inset of the shaft, this material has been changed for Stainless Steel (SS316L) with 60% of density.

The initial neutron dose distribution at the end of the shaft is represented in the figure 3.3. The initial configuration shows two peaks. The first one, at 30 cm of radius, is produced by the coolant pipe as the helium inlet. This peak has 350 Sv/h and is the maximum value with that configuration. The second one, at 35.5 cm of radius, is produced by the gap between the shaft and the monolith. Its value is 50 Sv/h. The dose in the others points are considerably less than these two peaks and they are around 5 Sv/h.

The first peak at the cooling pipe can be avoided by adding some shielding in the pipe. This is the first modification to try to reduce the neutron dose at the area of interest. The figure 3.4 shows the results of filling the cooling pipe with Stainless Steel (SS316L) with 60% of density. The first peak at 30 cm has been eliminated with the new shielding. Its value was 350 Sv/h and now it has been reduced to 200 mSv/h. Nevertheless, the second peak has not been eliminated and it persists at 50 Sv/h.

The figure 3.5 represents the comparison between the initial configuration and the first modification. Not only the maximum radiation peak has been removed, the general dose has been reduced $1-1.5$ orders of magnitude too. Much neutron radiation escaped through the cooling pipe and it affected the surrounding areas. The general neutron dose was around 5 Sv/h and now it's around 100 mSv/h.

However, the peak produced by the gap still gives too much dose. The methodology used in the first modification can not be utilized in the gap. The mechanical rotation of the shaft

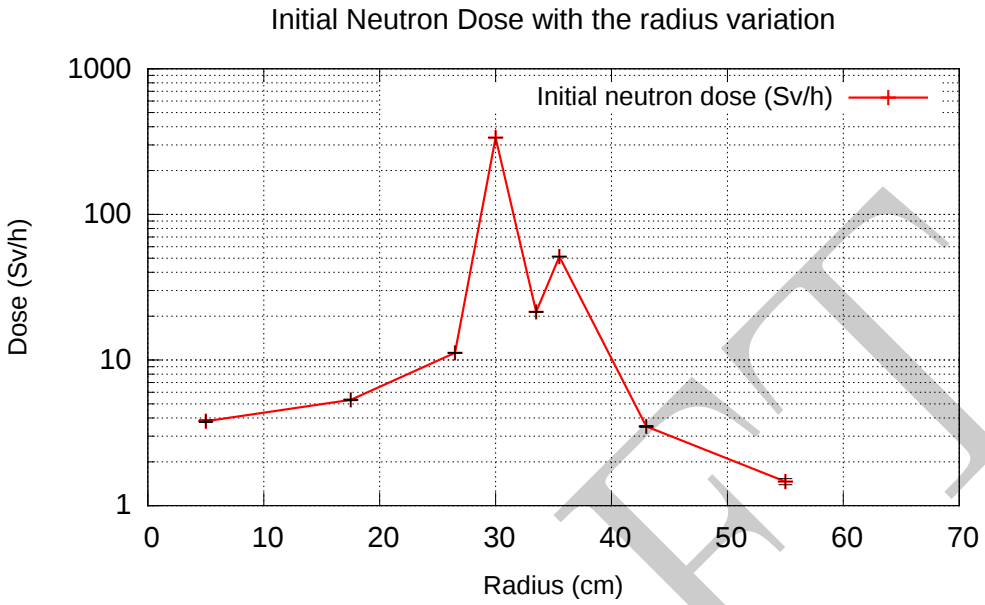

Figure 3.3: Initial neutron dose distribution with a 60% of density SS316L on the shaft center.

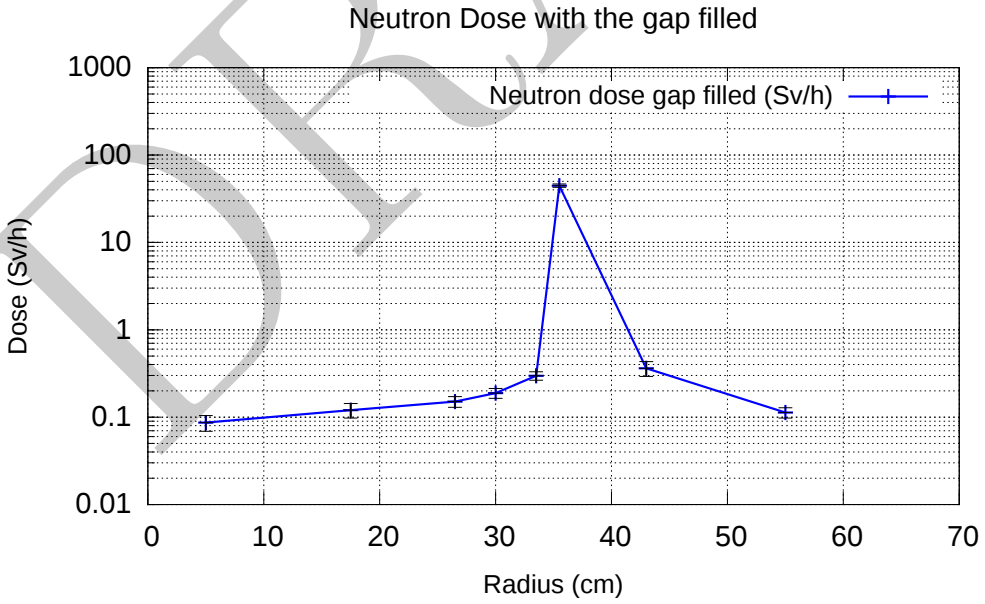

Figure 3.4: Neutron dose with the cooling pipe filled with a 60% of density SS316L.

needs this gap, so it can not be filled with a shielding material.

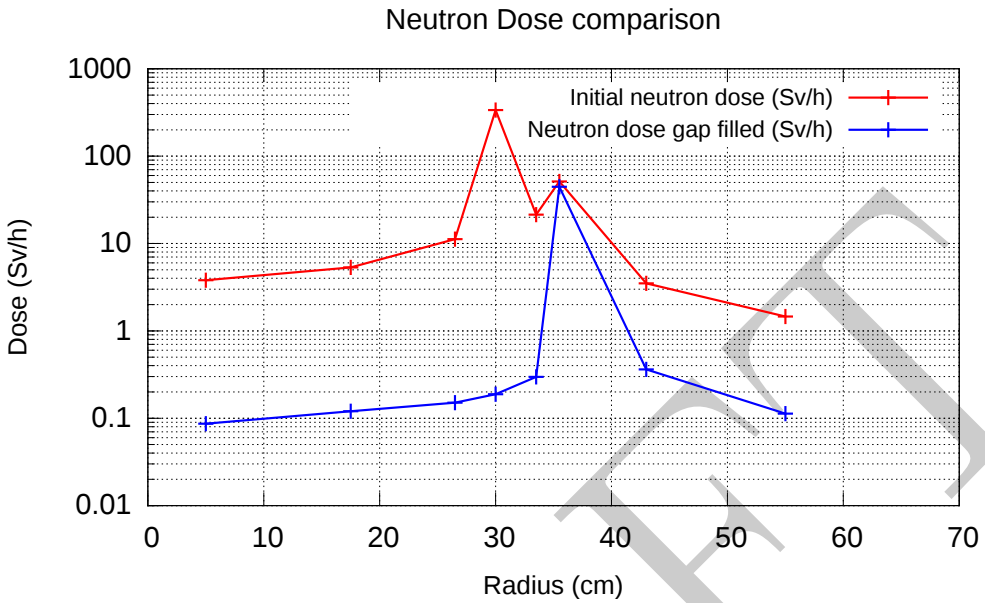

Figure 3.5: Neutron dose comparison between the initial configuration and the coolant pipe 60% shielding.

With the purpose to reduce this radiation, the Shaft Shielding Ring has been proposed.

3.3 Shaft Shielding Ring

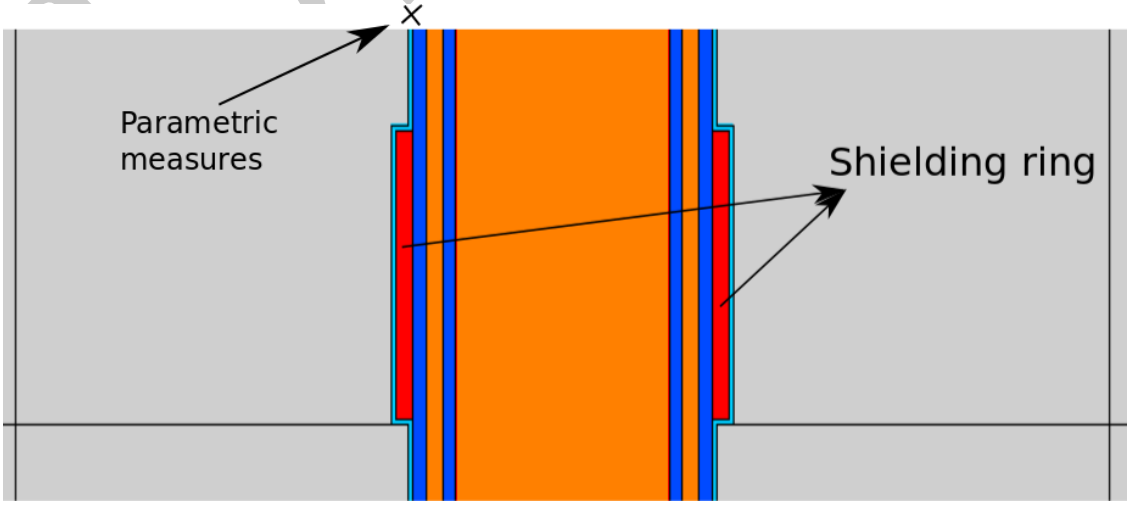

Figure 3.6: Shaft geometry with the shielding ring.

The Shaft Shielding Ring is a ring over the outer shaft radius, at 35 cm, that rotates with him. The purpose of this configuration is to make a labyrinth for neutrons leaving the facility through the gap. Without the ring, these neutrons have a direct exit with no opposition. The ring force them to pass through a shielding zone.

The configuration of the ring is represented in the figure 3.6. Two parametric calculations have been done in order to define the ring parameters: position and length. The width of the ring has been set at 4 cm. This dose measures have been taken at the end of the gap, at 35.5 cm of radius. The ring is made of SS316L for the parametric study.

The first parametric analysis tries to determinate the best positioning for the ring along the shaft. The figure 3.7 shows this analysis. For these calculations, the width and length have been set at 4 cm and 20 cm respectively. The position 0 cm corresponds to the target, at the bottom of the shaft, and the position 400 cm corresponds to the end of the shaft.

In the first place, the positioning at the beginning of the shaft doesn't reduce the dose so much. According as the position grows, the neutron dose decreases. From the positioning at 200 cm, at the middle of the shaft, the neutron dose doesn't decrease with the next values of position. This result allows to set the positioning of the ring at 200 cm since the beginning of the shaft.

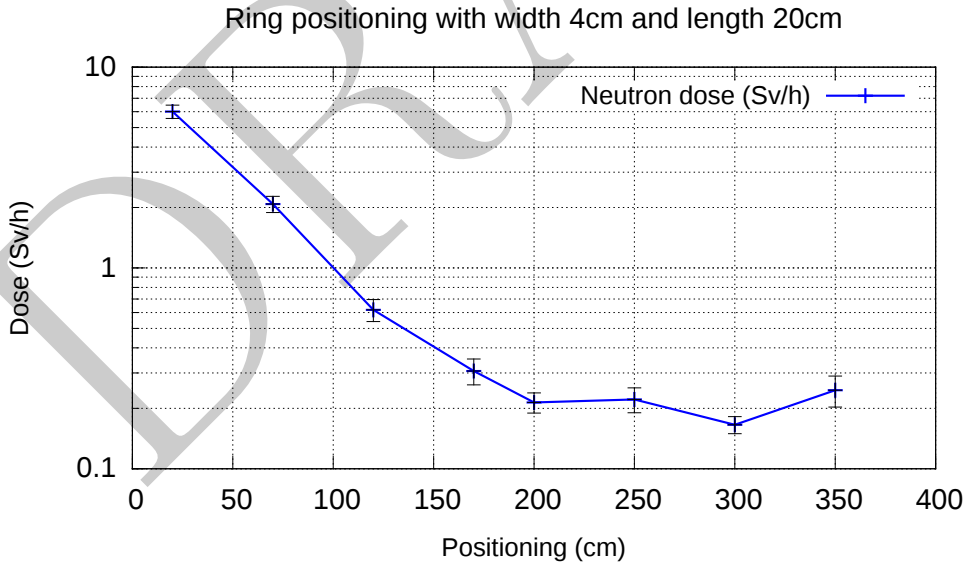

Figure 3.7: Parametric analysis for the ring positioning with the parameters of width= 4 cm, length= 20 cm and made of SS316L.

The second parametric analysis tries to determinate the best length for the ring, once the position has been set. The figure 3.8 shows this analysis. The width and position have been set at 4 cm and 200 cm respectively.

The results show that increasing the shaft length the neutron dose decreases. This behaviour continues until the length reaches 80 cm. From this point the dose doesn't decreases with the increment of the shaft length. The dose reduction reached with the length augmentation is around one order of magnitude from 20 cm to 80 cm. The optimal length is in the range of $80 - 100$ cm, and it has been set at 80 cm for the next analysis.

These two parametric calculations allow to conclude the final sizing of the shaft ring:

- Width of 4 cm
- Positioning at the middle of the shaft, at 200 cm from the bottom
- Length of 80 cm

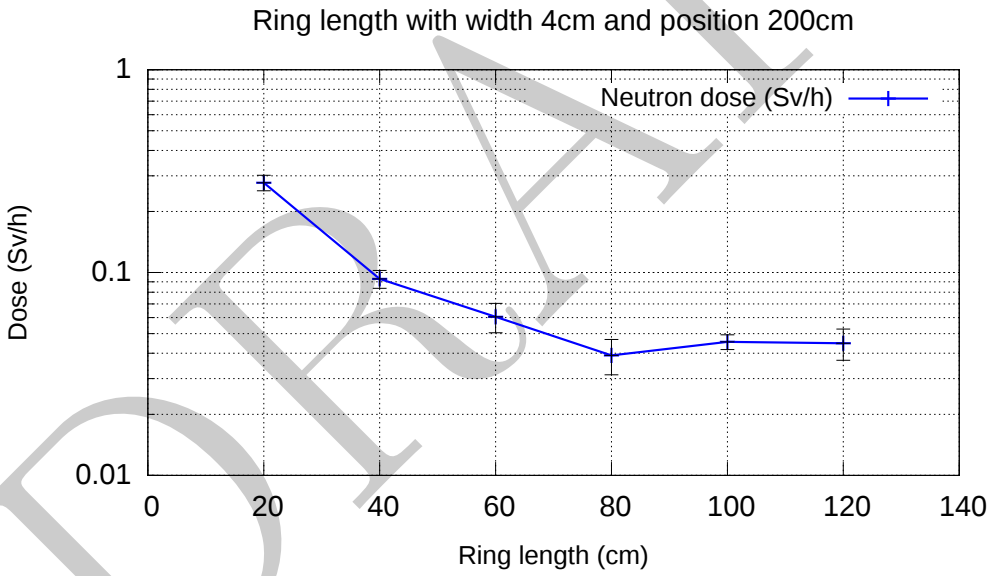

Figure 3.8: Parametric analysis for the ring length with the parameters of width= 4 cm, position= 200 cm and made of SS316L.

Once the ring sizing has been done, the neutron dose distribution has been calculated and it's represented in the figure 3.9. The neutron dose shows an homogeneous distribution in radius, so the radiation effect produced by the gap has been removed with this configuration.

To conclude the shaft ring analysis, the figure 3.10 shows the comparison between the previous neutron dose with the neutron dose provided by the shaft ring. The peak dose produced by the gap has been reduced from 50 Sv/h to 50 mSv/h. Moreover, the general dose has

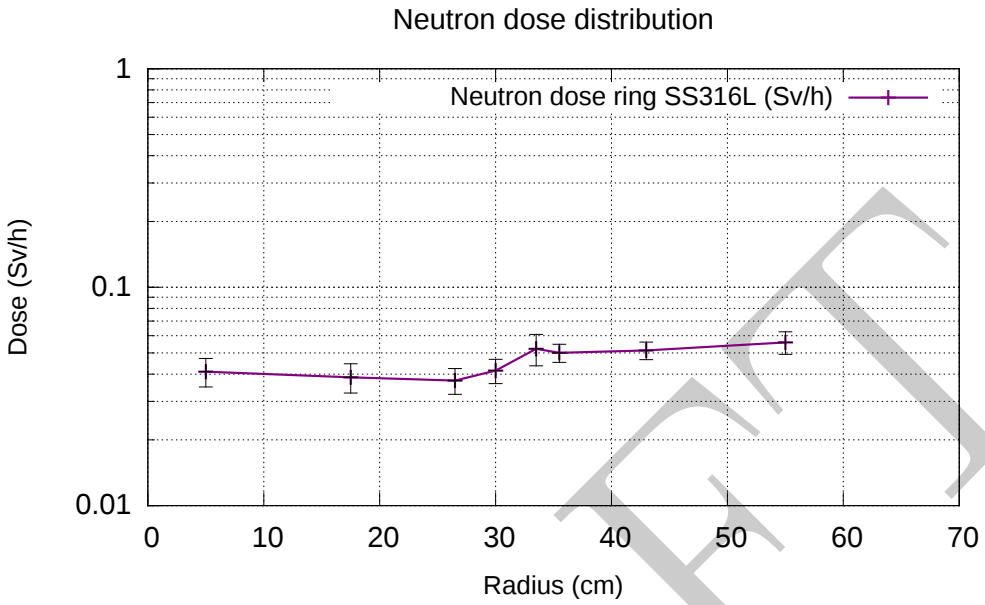

Figure 3.9: Neutron dose distribution in radius; width= 4 cm, length= 80 cm, position= 200 cm.

been reduced 0.5 orders of magnitude and its distribution is homogeneous in radius.

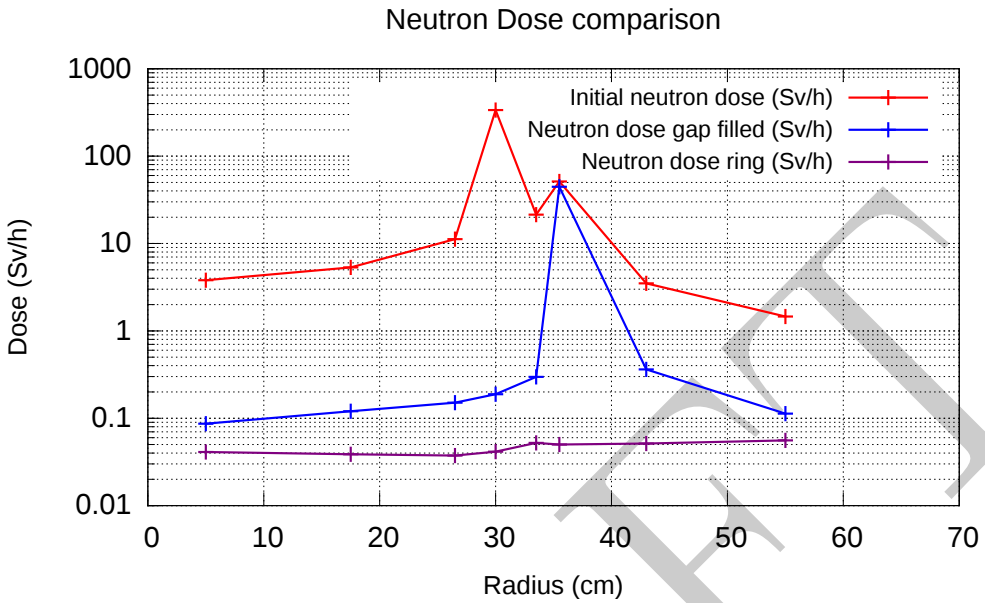

Figure 3.10: Neutron dose comparison between the previous situation and the ring contribution, with material SS316L.

3.4 Background dose

The previous calculation have been done with no material behind the end of the shaft. With this configuration, the effect of the components that could be placed at this area haven't been taken into account. The neutron scattering with these components could increase the neutron dose at the zones of interest. For that reason, the background dose has been calculated.

To do a conservative calculation of the background dose, a steel block has been placed behind the shaft. The steel block is a cylinder with equal radius than the monolith. Its width is 50 cm and it has been placed at 20 cm behind the shaft. In this case, the dose has been measured at 10 cm behind the shaft, at the middle of the space between the shaft and the steel block. These measures gives a dose distribution in the radius. The figure 3.11 represents the comparison between the background neutron dose and the neutron dose without the steel block.
The background dose has the same distribution in radius than the case without the steel block. However, the background dose is a factor of 3 greater. Its general dose is around 150 mSv/h while the previous general dose was 50 mSv/h.

To check that the background dose doesn't comes from the shaft, it has been done an analysis of which cells are the origin of the neutrons. This measure has been done at the end of the gap, at 35.5 cm of radius, and it's represented in the figure 3.12.

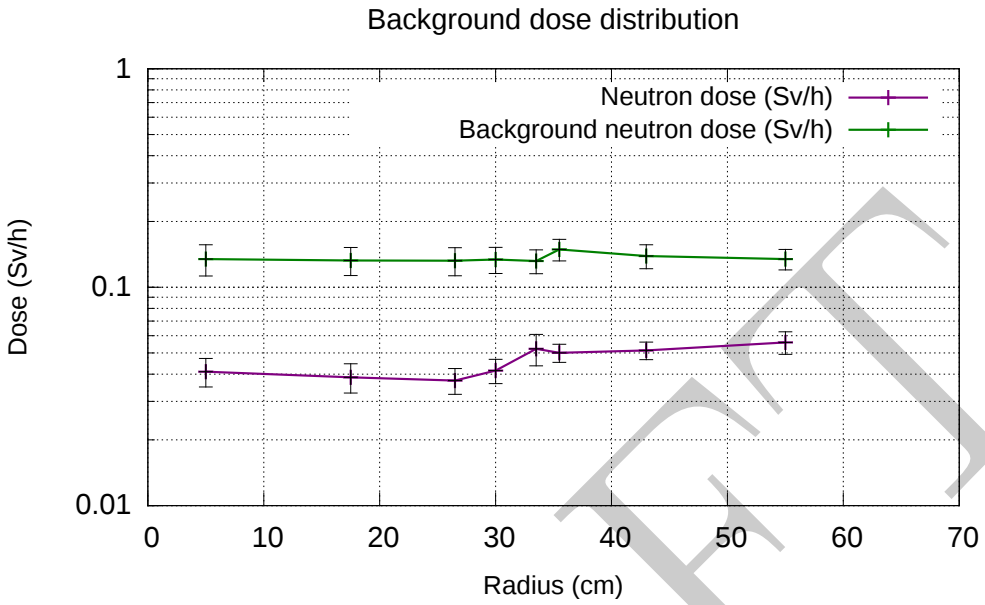

Figure 3.11: Background neutron dose with a steel block of 50 cm, positioning at 20 cm behind the end of the shaft.

The dose origin study shows that the major contribution comes from the steel block with a 37%. The next major contribution comes from the monolith. As the distance from the shaft increases, the dose contribution decreases. The values range are 21% to 1%. The rest of the dose, around 25%, comes from the different parts of the shaft, principally comes from the center of the shaft. These results show the correct shaft shielding.

3.5 Sensitivity analysis

The shaft dimensions are provided for the model used in the calculations (*"THE ESS TARGET STATION MONOLITH MCNP MASTERFILE (RB)", version rb55m0005*). These dimensions could change with the modifications in the design. This sensitivity analysis has been done in order to analyze how the variation of some parameters affects the radiation dose.

The first sensitivity analysis is the variation of the coolant pipe dimension. This element had been filled with SS316L 60% of density in the previous modifications. Its original thickness is 4 cm, according to the model. This dimension has been modified increasing 4 cm each new simulation. The results are shown in the figure 3.13.
The neutron dose distribution doesn't change its form with the variation of the coolant pipe dimension. However, the dose value increases as the radius increases. The maximum dose value reaches 300 mSv/h with an increment of 12 cm. That is reasonable because a 100% of shielding is been changed for a 60% of shielding.

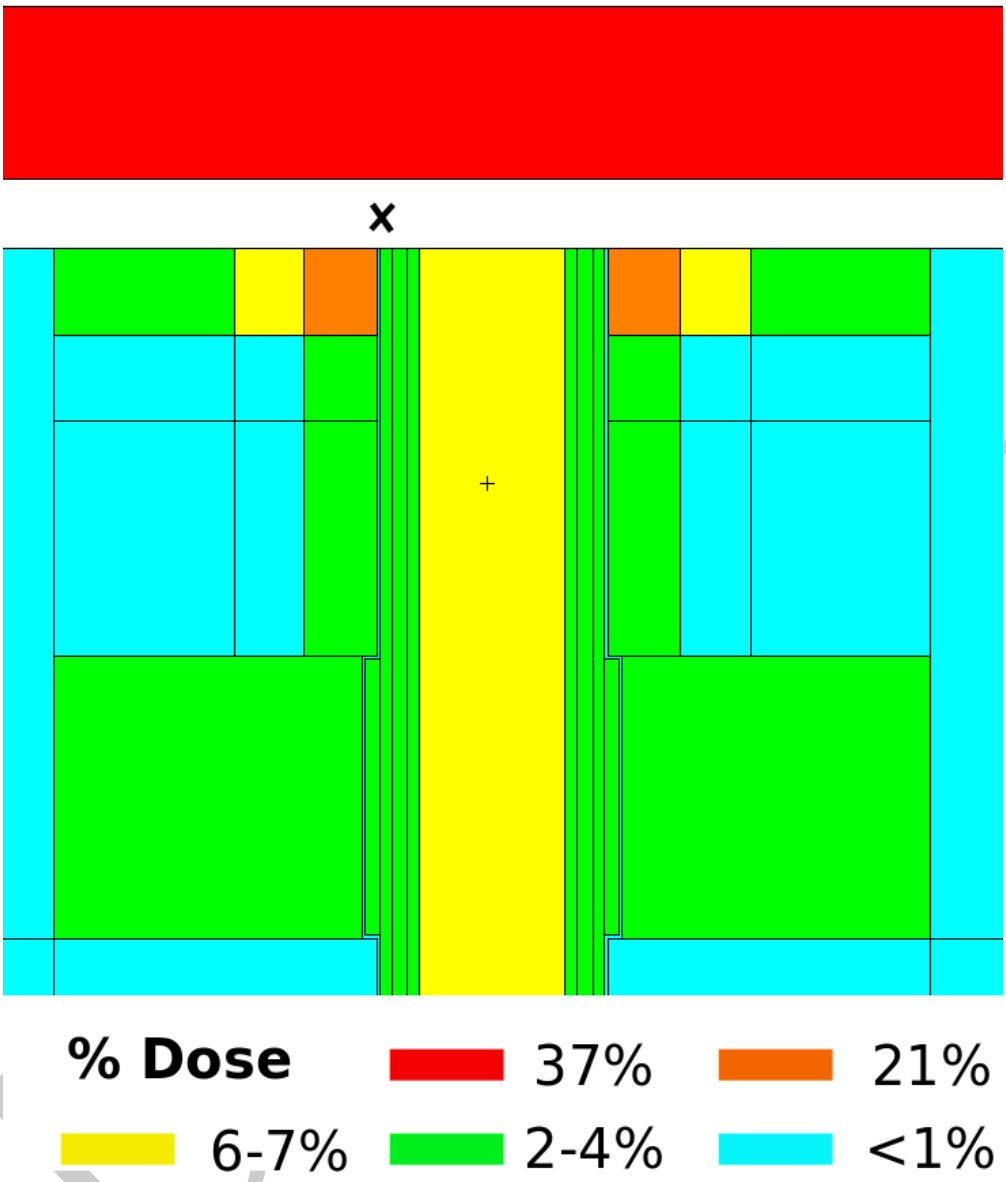

Figure 3.12: Analysis of the background dose origin with a steel block behind the shaft.

The second sensitivity analysis is the variation of the gap dimension. Its original thickness is 1 cm, according to the model. This dimension has been modified increasing 0.5 cm each simulation. The results are shown in the figure 3.14.

In the same way it happened with the previous analysis, the neutron dose distribution doesn't change its form. As the gap dimension increases the neutron dose increases. The maximum dose value reaches 250 mSv/h with a gap of 2 cm.

These two sensitivity analysis show that the neutron dose can increment its value a factor

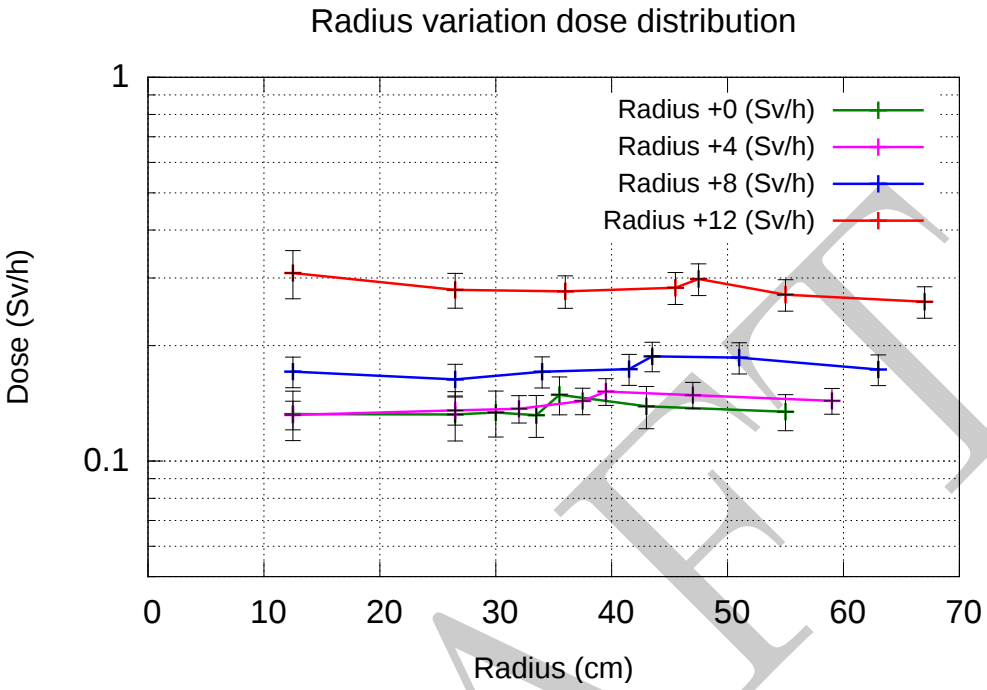

Figure 3.13: Analysis of the coolant pipe dimension. Radius variation referenced with the model from 0 cm to 12 cm.

of 2 with the dimension variation in the ranges considered. The maximum increment of the coolant pipe dimension considered is 12 cm and the maximum increment of the gap dimension is 1 cm.

A final study of the shaft shielding configuration has been done. It consists of removing the bottom part of the shaft shielding and study the effects produced on the dose at the top of the shaft. The shielding material has been changed for helium. The figure 3.15 represents this configuration in which are included the shaft ring and the steel block for the background dose.

The results of this analysis are in the figure 3.16 and show that removing this part of the shielding increases the neutron dose. Therefore, it isn't recommended of removing this part of the shielding.

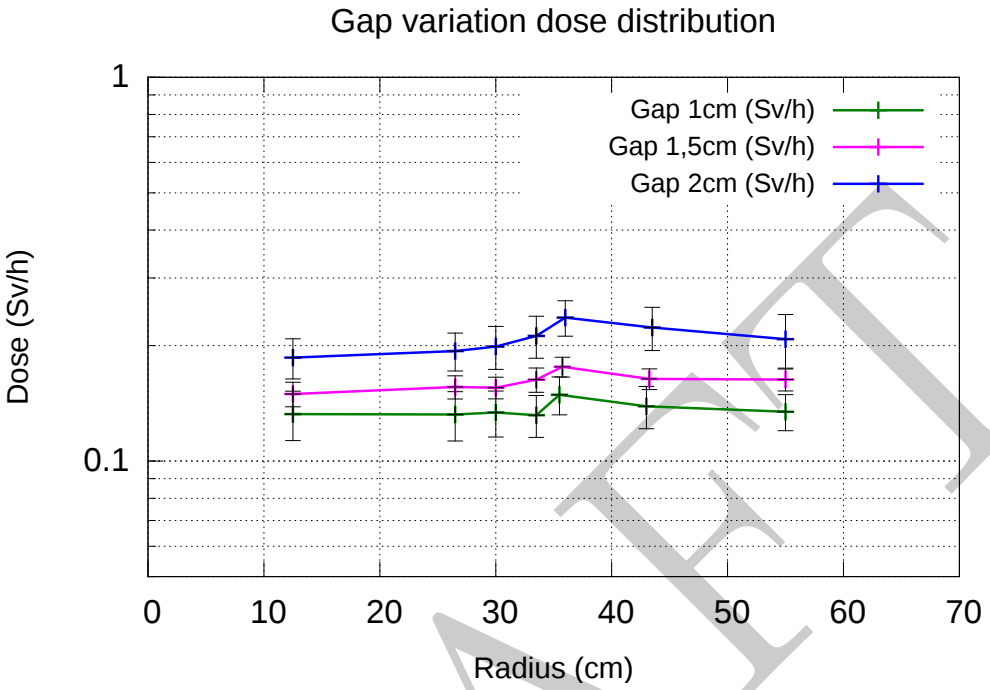

Figure 3.14: Analysis of the gap thickness. Gap measure from 1 cm to 2 cm.

3.6 Conclusions

The shaft needed a shielding to reduce the two peaks that the neutron dose distribution had. After some changes, the neutron dose has been reduced to optimal parameters.

- The peak produced by the coolant pipe has been eliminated by filling the coolant pipe with SS316 60% of density.
- The peak dose produced by the gap between the shaft and the monolith has been reduced to values of 50 mSv/h. This reduction has been done putting the shaft shielding ring.
  - Width of 4 cm
  - Positioning at 200 cm
  - Length of 80 cm
  - Made of SS316L
- This additional shielding should be design as a ring independent to the shaft which is introduced after the shielding blocks bellow the ring.
- The background dose is produced by the whole system, not by the shaft, and its value is 150 mSv/h.

Figure 3.15: Configuration of removing the bottom part of the shaft shielding.

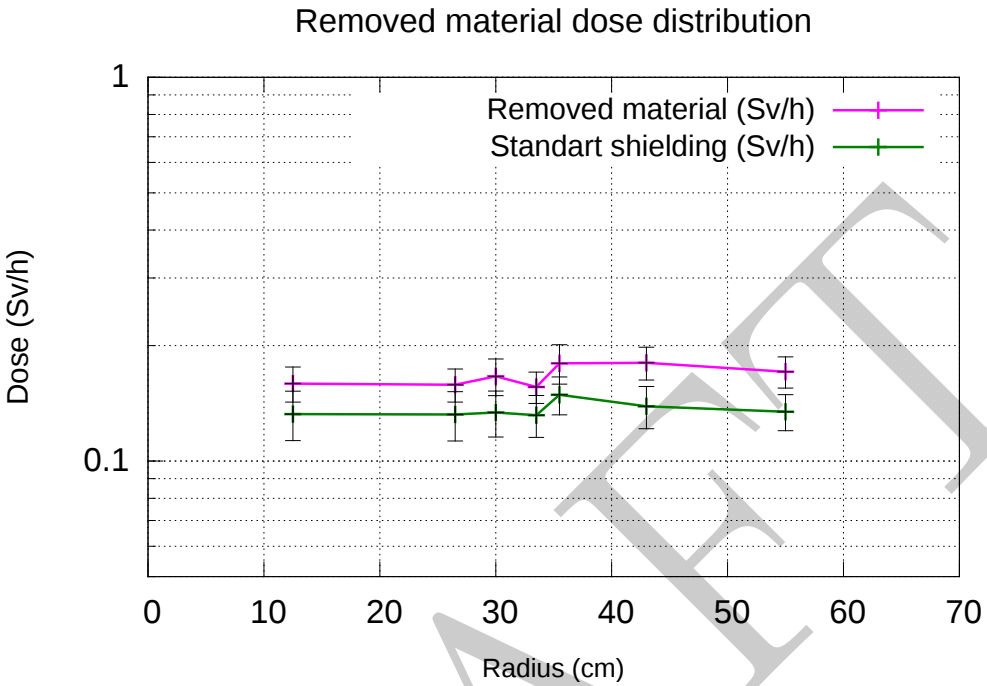

Figure 3.16: Analysis of removing the bottom part of the shaft shielding.

The table 3.1 and the figure 3.17 show the comparative results of the different situations in this shielding process.

Configuration	Gap at 30cm	Gap at 35.5cm	General dose
Initial situation	350 **Sv/h**	50 **Sv/h**	5 **Sv/h**
Cooling pipe shielding	200 mSv/h	50 **Sv/h**	100 mSv/h
Shaft Ring	50 mSv/h	50 mSv/h	50 mSv/h
Background	150 mSv/h	150 mSv/h	150 mSv/h

Table 3.1: Comparative neutron dose with the different configurations

A sensitivity analysis has been done to estimate the dose variation with the modification of some parameters. This analysis shows an increment in the neutron dose with the modification of the gap and cooling pipe dimensions. The table 3.2 represents the results of these two analysis.

Parameter	Initial dimension	Initial dose	Final dimension	Final dose
Cooling pipe	4 cm	150 mSv/h	16 cm	300 mSv/h
Gap	1 cm	150 mSv/h	2 cm	250 mSv/h

Table 3.2: Results of the sensitivity analysis.

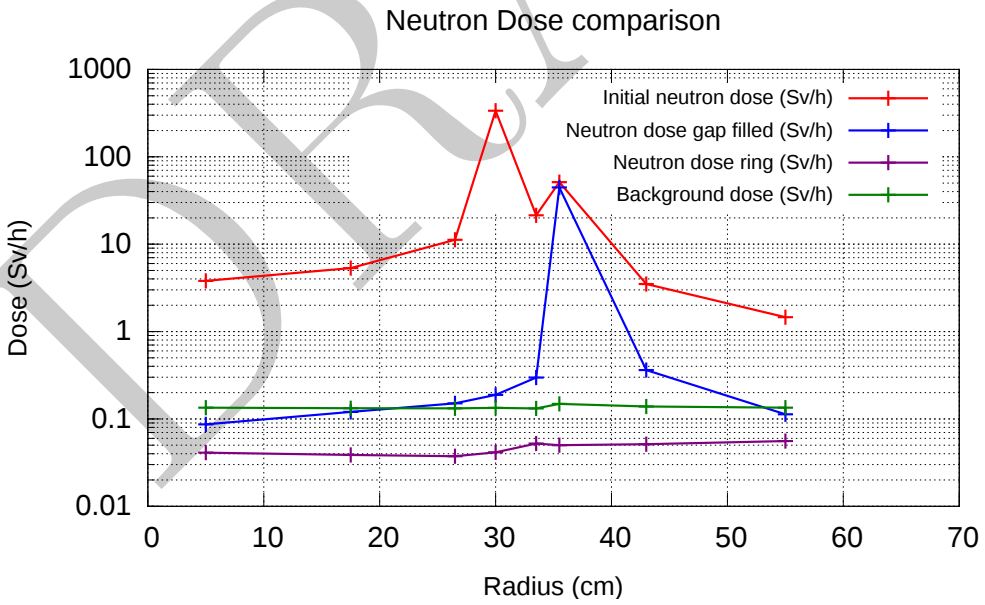

Figure 3.17: Final neutron dose comparison.

Bibliography

[1] ISIS neutron spallation source, UK: stfc.ac.uk. http://www.isis

[2] M. Mocko, G. Muhrer, Fourth-generation spallation neutron target-moderator-reflector-shield assembly at the Manuel Lujan Jr. neutron scattering center, Nuclear Instruments and Methods in Physics Research Section A: Accelerators, Spectrometers, Detectors and Associated Equipment, Volume 704, 11 March 2013, Pages 27-35, ISSN 0168-9002, http://dx.doi.org/10.1016/j.nima.2012.11.103. (http://www.sciencedirect.com/science/article/pii/S0168900212014507)

[3] http://www.afcen.com/en/publications/rcc-mrx

[4] A. Ghiglino, K. Thomsen, M. Magán, F. Martínez, F. Sordo, S. Terrón, R. Vivanco, J. de Vicente, M. Carrera, Jörg Wolters, Michael Butzek, WP13: Water cooled Cannelloni target as back-up solution for ESS, ESS-BILBAO Technical Report, June 2013

[5] D. B. Pelowitz, ed., MCNPX User's Manual, Version 2.7.0, Los Alamos National Laboratory report LA-CP-11-00438 (April 2011)

[6] ESS Technical Design Report, ISBN 978-91-980173-2-8

[7] Technical Report ESS-0019345

[8] ESS Lund private comunitation

[9] Y. Lee, Requirements for maximum stress and maximum temperature in proton-irradiated tungsten. Technical Report. March 19, 2014.

[10] Danish Atomic Energy Commission. Research Establishment RISÖ. The properties of helium: Density, Specific Heats, Viscosity and Thermal Conductivity at Pressures from 1 to 100 bar and from room temperature to about 1800 K.

[11] FLUENT Academic Research, Release 15.0, ANSYS, Inc.

[12] Nilsson, private comunication.